JAWAHARLAL NEHRU UNIVERSITY

A Study of Radio Relic and Radio Halo emission in Galaxy Clusters

by

Lijo Thomas George

A thesis submitted in partial fulfillment for the
degree of Doctor of Philosophy

RAMAN RESEARCH INSTITUTE
BANGALORE
INDIA

July 2017

Certificate

This is to certify that the thesis entitled **"A Study of Radio Relic and Radio Halo emission in Galaxy Clusters"** submitted by **Lijo Thomas George** for the award of the degree of Doctor of Philosophy of Jawaharlal Nehru University is his original work. This has not been published or submitted to any other University of any other Degree or Diploma.

Signed:

Prof. Ravi Subrahmanyan
Director

Signed:

Prof. K. S. Dwarakanath
Thesis Supervisor

Astronomy and Astrophysics Group,
Raman Research Institute,
Bangalore – 560 080
INDIA

Date:

Declaration of Authorship

I, **LIJO THOMAS GEORGE**, declare that this thesis titled, **'A STUDY OF RADIO RELIC AND RADIO HALO EMISSION IN GALAXY CLUSTERS'** and the work presented in it are my own. I confirm that:

- This work was done wholly while in candidature for a research degree at Jawaharlal Nehru University under the supervision of **Prof. K. S. DWARAKANATH**.
- No part of this thesis has previously been submitted for a degree or any other qualification at this University or any other institution.
- Where I have consulted the published work of others, this is always clearly attributed.
- Where I have quoted from the work of others, the source is always given. With the exception of such quotations, this thesis is entirely my own work.
- I have acknowledged all main sources of help.

Signed: _____

Prof. K. S. Dwarakanath
Thesis Supervisor

Signed: _____

Lijo Thomas George

Astronomy and Astrophysics Group,
Raman Research Institute,
Bangalore – 560 080
INDIA

Date: _____

"I owe my success to having listened respectfully to the very best advice, and then going away and doing the exact opposite."

G. K. Chesterton

Abstract

Diffuse radio emission from galaxy clusters is seen in the form of Mpc sized central halos and peripheral relics. These objects are rare but are predominantly found in merging clusters as compared to relaxed clusters. Most halos and relics have been detected at higher frequencies ($>$ 1 GHz). However, high frequency interferometric observations are not ideal for the detection of extended diffuse radio sources due to various selection effects. Low frequency measurements are better suited to detect halos and relics in galaxy clusters. As such we decided to observe a few merging galaxy clusters using the Murchison Widefield Array (MWA) which is located in a radio-quiet zone in Western Australia and operates in the frequency range 80-230 MHz. These clusters where chosen from literature based on their high frequency measurements and contained relics with or without radio halos. We imaged these clusters at all MWA frequencies and compared the images with those produced via a standard pipeline for the GaLactic and Extragalactic All-sky MWA (GLEAM) Survey. The MWA images were also compared with those from existing surveys like TGSS and NVSS as well as complimentary X-ray images from ROSAT, XMM-Newton and Chandra telescopes in order to understand the nature of the emission. The spectra of the halos and relics was estimated over 80-1400 MHz. This is the first time spectra of halos and/or relics have been estimated over such a large frequency range. Furthermore, the claimed relics in two clusters were reclassified as galaxies based on their spectra. In clusters where no halo was detected we placed stringent upper limits to a possible halo emission. These limits are the best that have been obtained so far. The implications of these results to models of halo formation will be discussed. We also report the detection of a new steep spectrum relic in a galaxy cluster using the GLEAM survey and its follow up observations with the GMRT.

Acknowledgements

They say it takes a village to raise a child and I feel the same can be said for a thesis as well. I would like to take this moment to thank all the people who have helped me through this journey.

First and foremost, I'd like to thank Prof. Dwarakanath for his mentorship these past few years. I have learnt a lot from him and not just about radio astronomy. I want to thank him for being patient with me even as I kept making mistakes and for helping me learn through those mistakes.

I would like to acknowledge all the people who taught me during coursework as well as the faculty on the Astro floor for random coffee time discussions (scientific and otherwise). A special thanks to members of my Advisory Committee (Prof. Ravi Subrahmanyan, Prof. Shiv Sethi and Prof. Sadiq Rangwala) for their comments and inputs.

This thesis makes use of data from the Murchison Widefield Array located at the Murchison Radio-astronomy Observatory in Western Australia and operated by the Commonwealth Scientific and Industrial Research Organisation (CSIRO). Thanks to the members of the MWA collaboration who have helped in shaping up this thesis, particularly, Prof. Melanie Johnston-Hollitt, Prof. Huib Intema and Prof. Natasha Hurley-Walker for their comments and inputs. Additional thanks to Viral and Ruta for discussions on radio astronomy and cluster physics.

This research has made use of the NASA/IPAC Extragalactic Database (NED) which is operated by the Jet Propulsion Laboratory, California Institute of Technology, under contract with the National Aeronautics and Space Administration. This research has made use of data obtained from the High Energy Astrophysics Science Archive Research Center (HEASARC), provided by NASAs Goddard Space Flight Center.

I would like to thank Vidya for... well... being Vidya. With a matronly presence, she has always ensured that all the background stuff is taken care of so that we students don't need to worry about them. Thanks to the admin members (Marissa, Radha etc.), the library staff and the computer department for all their help.

This journey has been extremely hard but it would have been unbearable were it not for my friends and colleagues in the institute. A huge thanks to Priyanka, Gayathri, Karam, Mayuri, Varun, Nomaan, Raju, Kshitij, Nipanjana and Chandreyee for the love, the laughter and the memories. I will be eternally grateful to Nazma for being my closest friend and confidante for the past 6 years.

And last, but certainly not the least, I'd like to thank my family for their love and support. My brother and my parents have been a never-ending source of love and encouragement ever since I decided to do this PhD. My thanks to them for being patient with me when I was complaining, pushing me when I needed pushing and most importantly believing in me even when I didn't.

From the bottom of my heart, thank you all!

CONTENTS

LIST OF FIGURES

LIST OF TABLES

Dedicated to
My family

CHAPTER

ONE

INTRODUCTION

1.1 Galaxy Clusters

Galaxy clusters are the largest ($\sim$ Mpc) gravitationally bound objects in the Universe with the most massive clusters having masses $\sim 10^{15} M_{\odot}$. They are composed primarily of dark matter ($\sim 80\%$) with the bulk of the remaining mass ($15 - 17\%$) accounted for by the gas in the Intra-Cluster Medium (ICM). Luminous matter in the form of stars and galaxies only contribute $3 - 5\%$ of the total mass of a galaxy cluster.

According to the hierarchical model of structure formation, perturbations in the primordial density distribution causes dark matter to become overdense in certain regions. Figure 1.1 shows a slice of the Millennium Simulation (Springel et al., 2005) where dark matter is shown clumping together at these "nodes" which are connected to each other by the filamentary "Cosmic Web". These nodes act as potential wells resulting in an infall of baryonic matter and consequentially the formation of galaxies and galaxy clusters. Subsequent gravitational attraction causes mergers between the galaxies and galaxy clusters. These cluster mergers are some of the most energetic events in the Universe. The most massive clusters can dissipate energies $\sim 10^{63} - 10^{64}$ ergs into the ICM during a merger event (Hoeft et al., 2008).

A typical galaxy cluster can contain hundreds to thousands of galaxies bound together gravitationally within a radius of $\sim$ Mpc.. The ICM gas that pervades the cluster is hot ($T \sim 10^{8} K$) and has a density $\sim 10^{-3} - 10^{-4}$ cm^{-3} (Sarazin, 1988). Figure 1.2 shows the galaxy cluster MACS J0416.1-2403 as seen by the Hubble Space Telescope (HST).

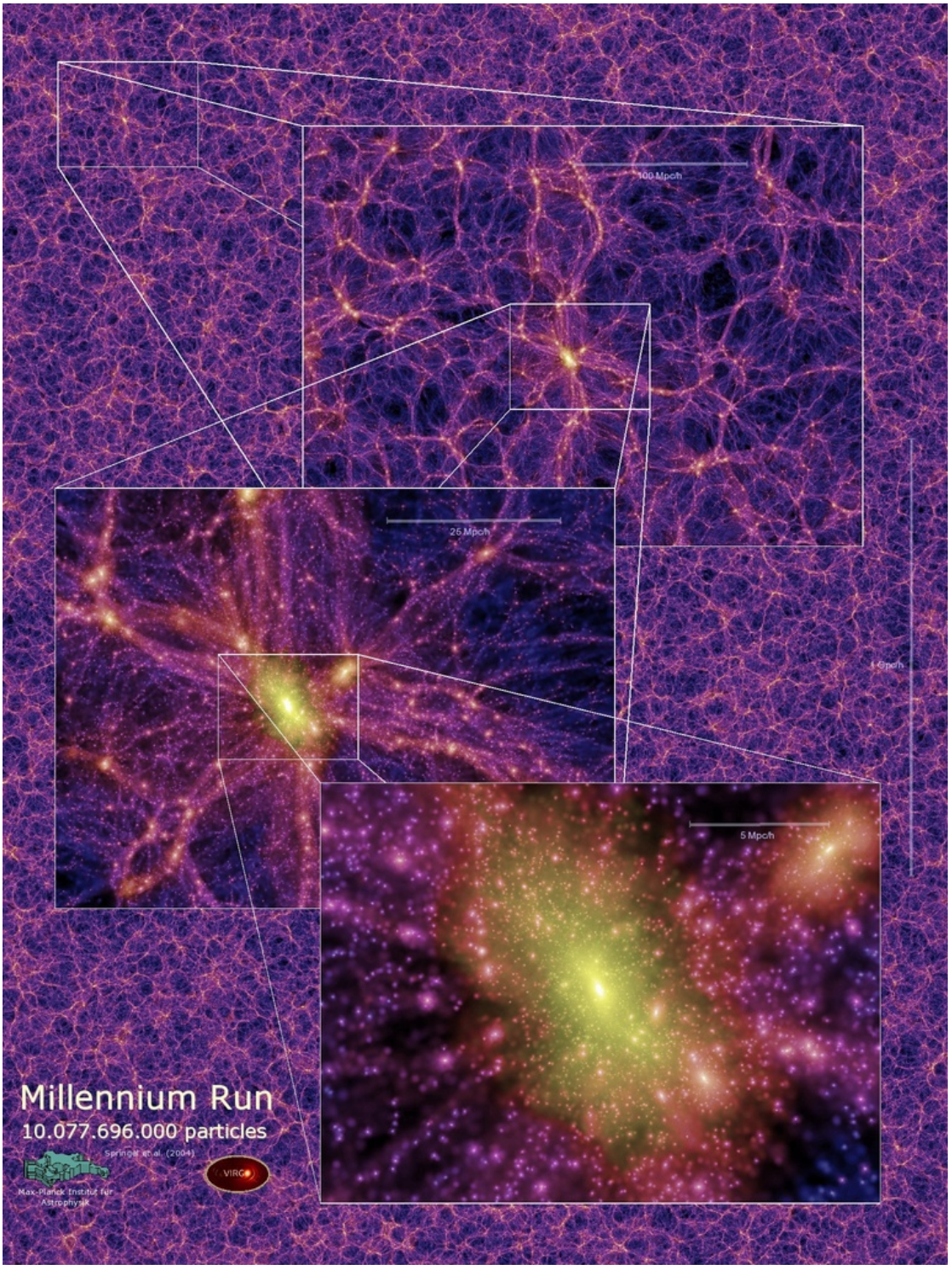

FIGURE 1.1: Slice of the Millennium Simulation. The background image is the projected density field for a 15 Mpc/h thick slice at $z = 0$. The overlaid square panels enlarge the region by a factor of 4 each time.

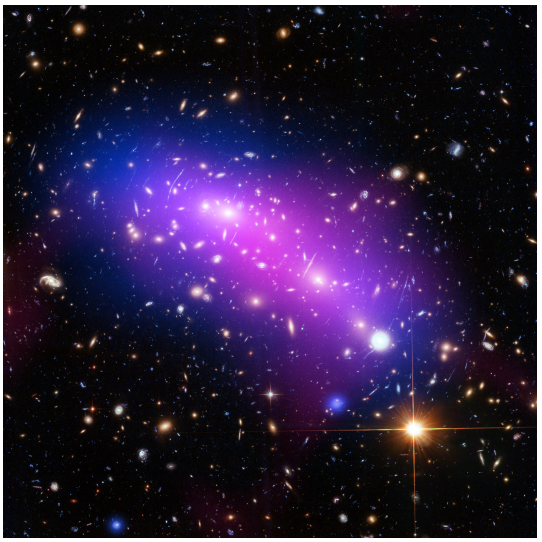

FIGURE 1.2: Cluster MACS J0416.1-2403 in the optical, radio and X-ray regimes. The optical data is from the Hubble Space Telescope, X-ray is from the *Chandra* telescope, while the radio image is obtained from the Jansky Very Large Array (JVLA) (Ogrean et al., 2015)

Also shown in this image are the observations of the cluster in X-ray (blue) using the *Chandra* telescope and in radio (red) using the NRAO Jansky Very Large Array (JVLA).

1.2 Emission from ICM in galaxy clusters

Emission from the ICM in galaxy clusters occurs mainly in the regime of X-rays and radio waves.

X-ray emission from the ICM occurs primarily in the form of *thermal bremsstrahlung* radiation wherein thermal electrons in the hot ICM plasma ($T \sim 10^7 - 10^8$ K) deaccelerate in the Coulombic field of ions and produce X-ray radiation. This emission depends on the temperature of the gas ($\propto T^{-1/2}$) and falls of exponentially ($\propto e^{-h\nu/kT}$). The contribution to X-ray emission from relativistic electrons (due to Inverse-Compton scattering) is relatively small and ignorable. The total X-ray luminosity in galaxy clusters ($L_{\rm X}$) is usually $\sim 10^{44} - 10^{45}$ erg s^{-1} .

All sky X-ray surveys like the *Uhuru* sky survey (Giacconi et al., 1972), the Extended Medium Sensitivity Survey (EMSS) with the *Einstein Observatory* (Gioia et al., 1990), the *ROSAT* All-Sky Survey (RASS, Voges 1992, Ebeling et al. 1996), and it's follow up the ROSAT-ESO Flux LimitEd X-ray (REFLEX) Survey (Böhringer et al., 2001, 2004) and most recently, the MAssive Cluster Survey (MACS, Ebeling et al. 2001) were instrumental in discovering and identifying galaxy clusters and studying their X-ray

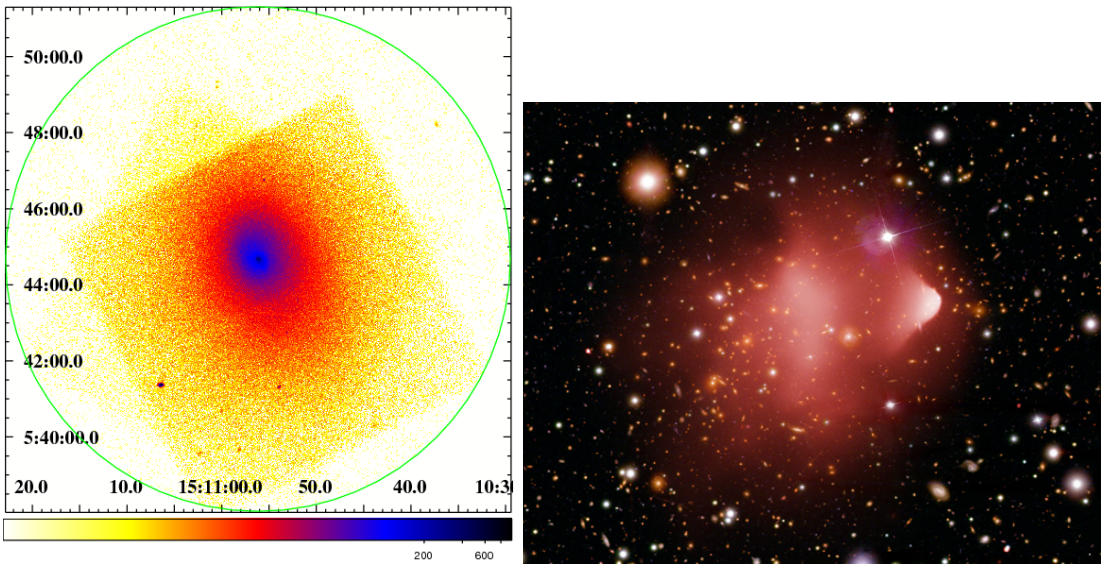

FIGURE 1.3: Relaxed and Disturbed Clusters. *Left:* A2029 (Million and Allen, 2009) is a low redshift cluster ($z = 0.0779$) with a relaxed X-ray morphology. The figure shows the surface brightness (counts) in the cluster in the 0.8 to 7.0 keV band of the *Chandra* telescope. *Right:* The Bullet Cluster (1E 0657-558) (Markevitch et al., 2002) is an intermediate redshift ($z = 0.3$) cluster with a disturbed X-ray morphology. The figure shows the *Chandra* X-ray image of the cluster on top of the optical image. The image is $6.7'$ across in size.

properties. Figure 1.3 shows the X-ray images of two clusters – one relaxed and one disturbed.

In addition to X-rays, the ICM in galaxy clusters is also known to emit in the radio band. This emission is unlike the emission detected from sources like supernovae, the Active Galactic Nuclei (AGN) at the centre of galaxies or the jets and lobes produced in galaxies as it has no optical counterpart. It is diffuse in nature (~ 1 mJy arcmin^{-2} at 1.4 GHz) and extends over the entire $\sim$ Mpc region of the cluster. It's origin is non-thermal as it is the synchrotron radiation produced due to the motion of relativistic electrons in the magnetic field ($\sim \mu$G) of the cluster.

This diffuse radio emission from galaxy clusters is seen in 2 main forms – the cluster-wide *radio halos* or *radio relics*, found mainly near the peripheries of the cluster (Feretti and Giovannini, 1996). Figure 1.4 shows the radio contours at 1.4 GHz of the prototypical radio halo in the Coma Cluster (left panel) as well as the spectrum of the radio emission (right panel). Although the radio emission spectrum does follow a power-law, it steepens at higher frequencies. This is a consequence of the nature of the emission itself. A few important properties of synchrotron radiation will be discussed below before discussing radio halos and radio relics in detail afterwards.

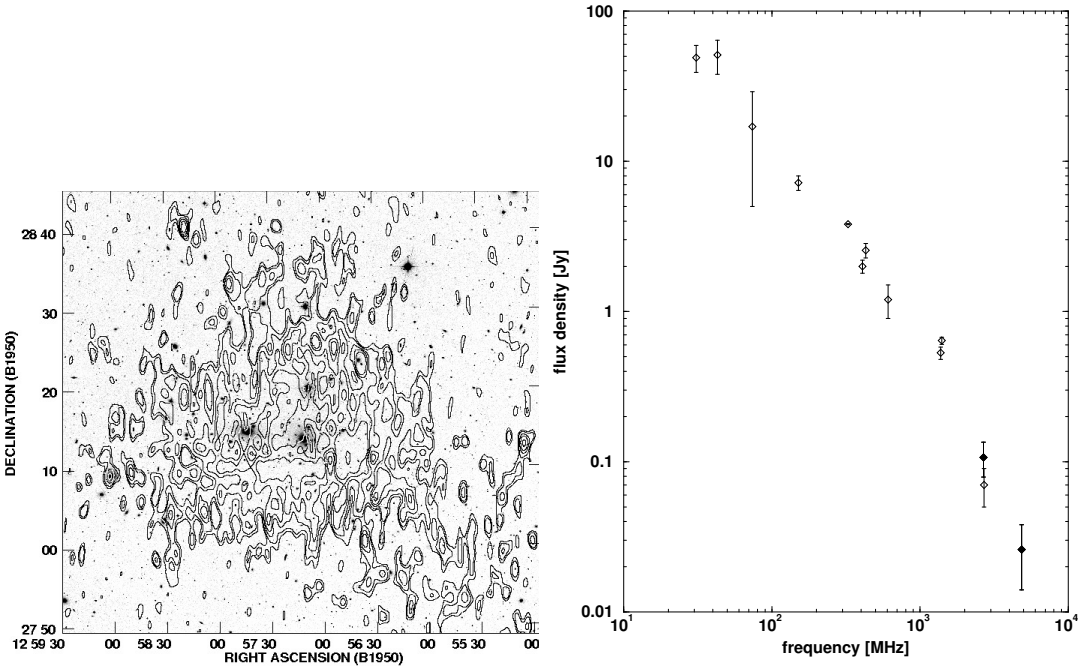

FIGURE 1.4: *Left:* The 90 cm contours of the radio halo in the Coma cluster overlaid on the DSS optical image after removing all the point sources (Feretti, 2002). *Right:* Spectrum for the radio halo in the Coma cluster over the frequency range 30-5000 MHz (Thierbach et al., 2003).

1.2.1 Synchrotron Radiation

Synchrotron radiation is produced due to the motion of high-energy electrons ($\gamma \gtrsim 10^4$, where γ = Lorentz factor) in the presence of a magnetic field, B.

In astrophysical scenarios, electrons are usually found to have an energy distribution of the form, $N(E)dE \propto E^{-p}dE$. In such a scenario, the total power of the synchrotron radiation (S), as a function of frequency (ν), will follow a power law where the spectral index of the spectrum will be, $\alpha = (p-1)/2$, where $S \propto \nu^{-\alpha}$. The ultra-relativistic electrons generating this radiation suffer from energy losses due to various reasons such as Inverse-Compton (IC) scattering (e.g. from the Cosmic Microwave Background (CMB) photons pervading the Universe) as well as losses due to adiabatic expansion. Furthermore, the electrons also suffer losses due to synchrotron radiation. The rate of energy loss due to IC scattering and synchrotron radiation (in the relativistic limit, i.e. $v \to c$) are given below.

$$-\left(\frac{dE}{dt}\right)_{IC} = \frac{4}{3}\sigma_{\rm T} c \gamma^2 U_{\rm rad}, \tag{1.1}$$

$$-\left(\frac{dE}{dt}\right)_{\rm synch} = \frac{4}{3}\sigma_{\rm T} c \gamma^2 U_{\rm mag} = 6.6 \times 10^4 \gamma^2 B^2 \ \ {\rm eV\,s^{-1}}, \tag{1.2}$$

where, $\sigma_{\rm T}$ is the Thomson Scattering cross-section, c is the speed of light, γ is the Lorentz factor for the electrons with energy $E = \gamma m_e c^2$, $U_{\rm mag}$ is the magnetic field energy, B is the magnetic field in the cluster (in Tesla, where 1T $= 10^4$ Gauss) and $U_{\rm rad}$ is the energy density of the radiation field. In the case of CMB radiation, $U_{\rm rad}$ depends on the redshift through an equivalent magnetic field ($B_{\rm IC}$) which is given by $B_{\rm IC} = 3.25(1+z)^2$, where $B_{\rm IC}$ is in units of μG (microGauss). Note that the energy loss rates due to both IC and synchrotron radiation are proportional to E^2. This means that higher energy electrons lose energy faster than lower energy electrons.

It can be shown that when IC and synchrotron losses dominate, the energy distribution of the electrons steepens (Longair, 1994). The spectrum of the electron distribution gets changed to $N(E) \propto E^{-(p+1)}$. As a result, the spectral index of the radio emission also steepens by 0.5. The frequency at which this steepening takes place provides information about the spectral age of the emitting source. The lifetime of the electrons can be estimated using the relation

$$t_{\rm age} = 1060 \frac{B^{0.5}}{B^2 + B_{\rm IC}^2} \left[(1+z)\nu\right]^{-0.5}, \tag{1.3}$$

where, z is the redshift and ν is the break frequency (Slee et al., 2001).

1.3 Radio Halos

Radio halos are sources of synchrotron emission from the ICM and are found in the central regions of the cluster. The radio halo in Coma (Figure 1.4) was the first such object to be discovered (Thierbach et al., 2003, Willson, 1970, Schlickeiser et al., 1987, Giovannini et al., 1993, Bonafede et al., 2010). Since then many more radio halos have been discovered. Figure 1.5 shows another example of a galaxy cluster (A520) that hosts such a halo. Also shown in the image is the spectral index map of the cluster between 325 MHz and 1.4 GHz. The morphology of radio halos is usually very smooth and the emission extremely diffuse. The magnetic field in galaxy clusters is $\sim \mu$G (Carilli and Taylor, 2002) but the radio emission in halos has very little polarisation ($\sim$5%) (Feretti and Giovannini, 1998, Bacchi et al., 2003).

Statistically, radio halos are not very common in the Universe. Only $\sim$5% of galaxy clusters below a redshift of 0.2 have been found to host a radio halo (Giovannini et al., 1999). However, if one considers massive galaxy clusters i.e. clusters with X-ray luminosity $L_{\rm X} \gtrsim 10^{45}$ erg s^{-1} , this fraction increases to almost one-third (Venturi et al., 2008, Kale et al., 2013). One caveat that should be considered when discussing these

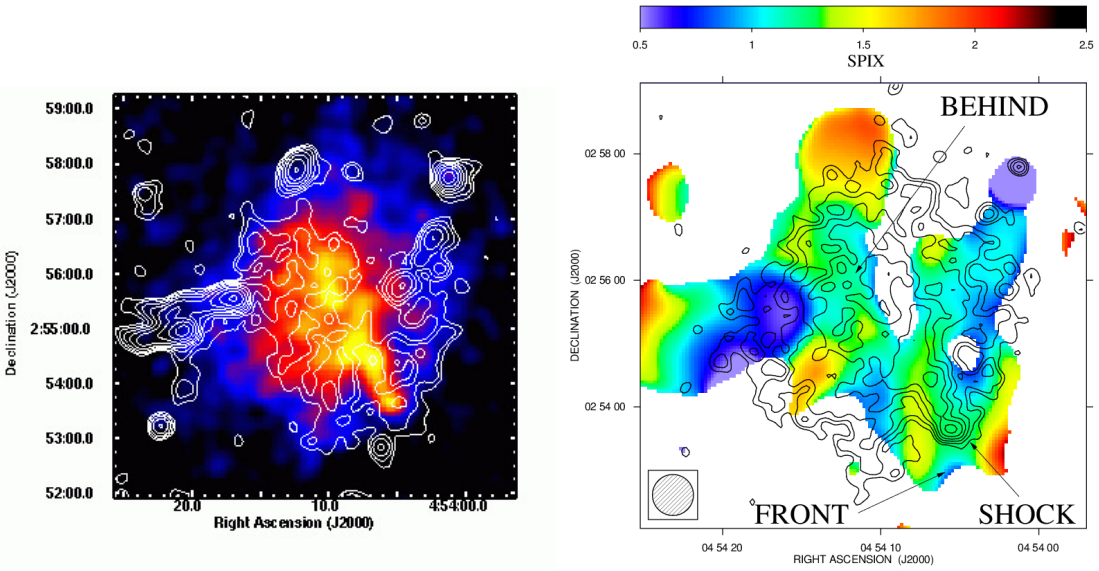

FIGURE 1.5: *Left:* The 1.4 GHz contours ($15'' \times 15''$) of the radio halo in Abell 520 overlaid on the *Chandra* X-ray image (Govoni et al., 2004). The contour levels are at 0.06, 0.12, 0.24, 0.48, 0.96, 1.92, 3.84, 7.68 mJy beam^{-1} . *Right:* Spectral index map of A520 in colour (between 325 MHz and 1.4 GHz) overlaid with the X-ray contours of the cluster (Vacca et al., 2014)

.

results is that these surveys are biased towards the highly X-ray luminous clusters. This is because halos in high X-ray luminosity clusters have higher radio luminosities as well (Brunetti et al., 2009, Bacchi et al., 2003, Liang et al., 2000, Cassano et al., 2006, Brunetti et al., 2007, Rudnick and Lemmerman, 2009). As a result it is possible that halos with lower radio power were not detected by the current generation of radio telescopes.

Comparison of the radio power of halos in clusters and the X-ray luminosity of the cluster show an empirical correlation between the two (Kale et al., 2015). Figure 1.6 shows the $L_X - P_{1.4}$ relation between cluster radio halo power at 1.4 GHz and the cluster X-ray luminosity from the recent GMRT Radio Halo Survey (GRHS, Venturi et al. 2008, 2007) and Extended GMRT Radio Halo Survey (EGRHS, Kale et al. 2015, 2013). It should be noted here that most of the halos are ∼Mpc in size even though halos have been discovered with sizes ∼500 kpc.

The sizes of the radio halos are an important factor when discussing their origin. Diffusion of relativistic electrons from the jets of radio galaxies cannot explain the ∼ Mpc scale emission seen from most radio halos. The diffusion velocities of relativistic electrons in a cluster are limited by the Alfvén wave velocity of electrons, i.e. $v_e \lesssim 100$ km s^{-1} , where, v_e is the group drift velocity of electrons. The time required for relativistic electrons ($\gamma \gtrsim 10^4$) to diffuse to ∼Mpc distance is ∼ Hubble time and thus

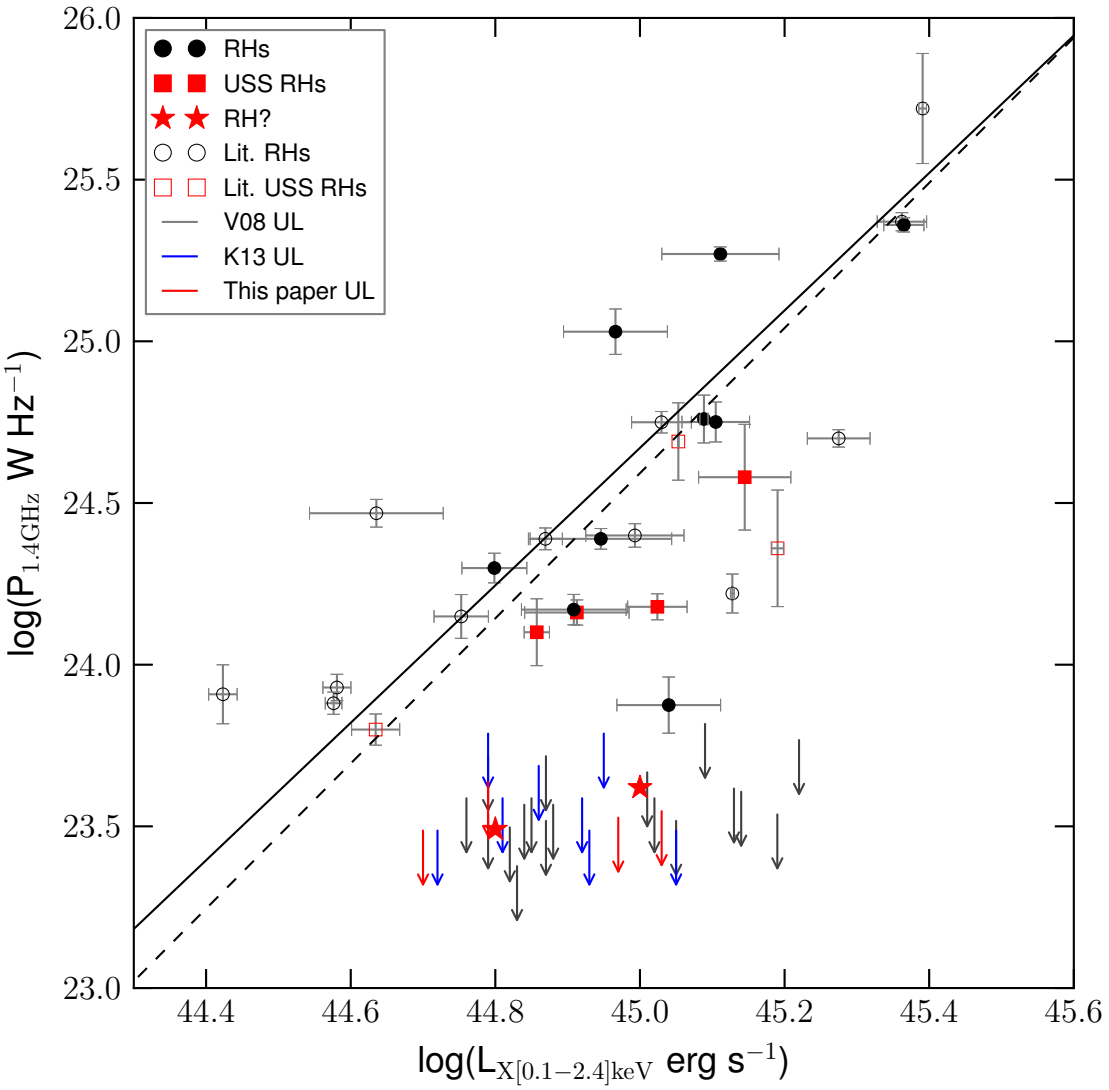

FIGURE 1.6: $L_X - P_{1.4}$ relation for radio halos and upper limits in the GRHS and EGRHS (Kale et al., 2015). The solid line represents the best fit to the relation after excluding the Ultra Steep Spectrum radio halos (USSRH). Dashed line includes the USSRHs.

much larger than the lifetime of the relativistic electrons themselves ($\sim 10^8 - 10^9$ years). This is known as the *diffusion problem* (Jaffe, 1977). Figure 1.7 shows the timescale of losses for high energy electrons (blue) and protons (red) at 1μG (solid line) and 3μG as compared to the diffusion timescale (magenta) (Blasi et al., 2007) .

In order to explain the presence of relativistic electrons across the ~Mpc scale cluster, the electrons in the ICM need to be accelerated *in-situ* (Jaffe, 1977). Any model to explain the mechanism of halo generation needs to account for the acceleration of electrons to relativistic levels as well has how this acceleration is maintained through the various energy losses that relativistic electrons are subjected to.

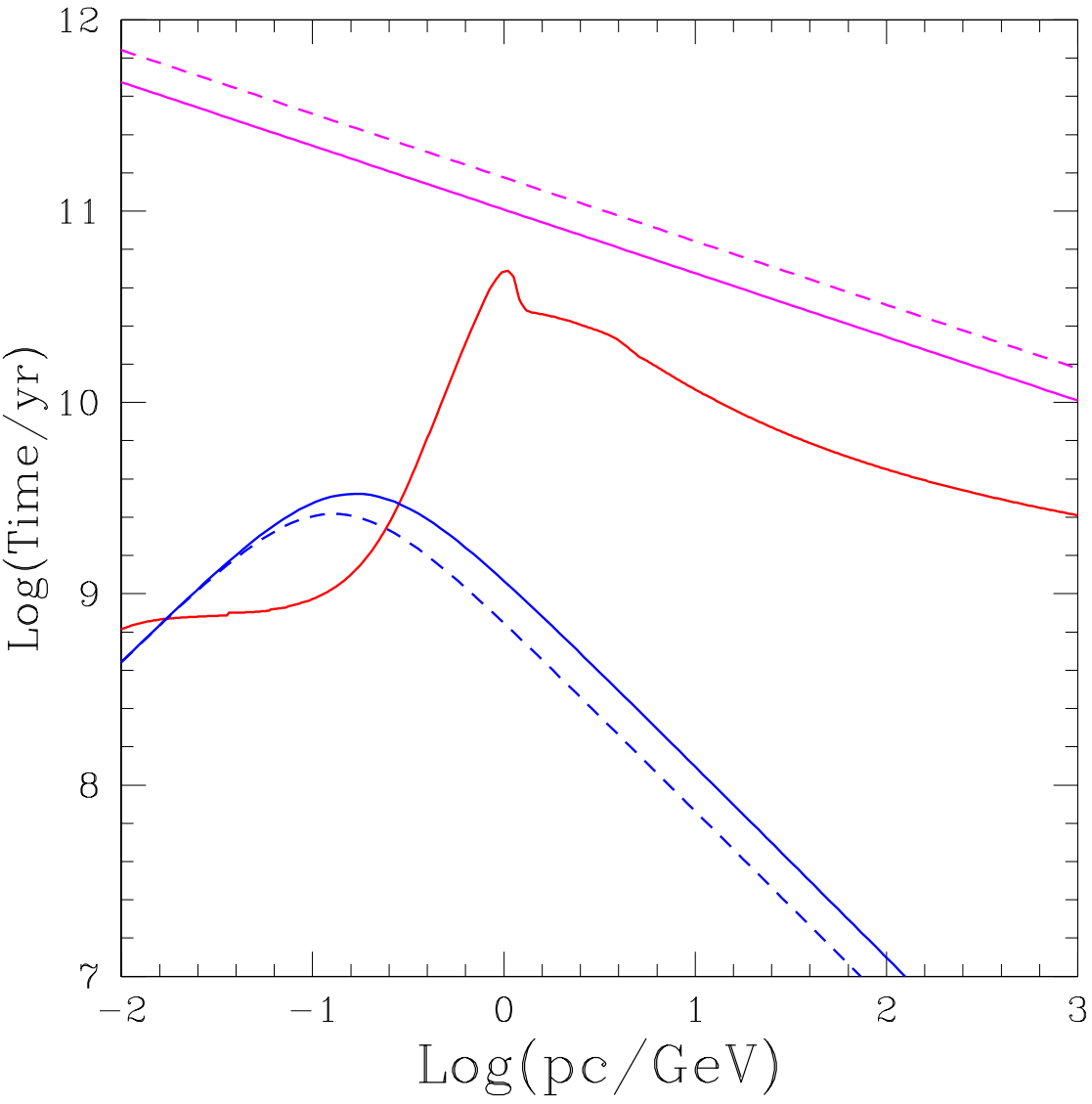

FIGURE 1.7: Timescale for energy losses in a galaxy cluster for protons(red) and electrons (blue). Diffusion time scales for protons are also plotted (pink). Magnetic field is assumed to be 1μG (solid) and 3μG (dashed).

1.3.1 Primary Model

The most well accepted model that satisfies these conditions is the *primary model* that posits that the turbulence generated at the time of cluster merger provides sufficient energy to accelerate electrons to relativistic levels (Harris et al., 1980, Tribble, 1993, Brunetti et al., 2001a, Petrosian, 2001, Fujita et al., 2003, Brunetti et al., 2004, Brunetti and Lazarian, 2007). One of the reasons there is a lot of support for this theory is the observation that most of the radio halos observed so far have been detected in merging galaxy clusters. Merging galaxy clusters have extremely disturbed X-ray distributions as well. The non-uniformity of X-ray distribution in galaxy clusters is quantifiable.

The most common parameters used to measure the disturbed nature of galaxy clusters are - power ratios, the emission centroid shift (w) and the surface brightness concentration parameter (c). Power ratios compare the multipole expansions of the X-ray surface brightness in a cluster (Buote and Tsai, 1995, Böhringer et al., 2010). They are usually defined as,

$$P_0 = [\, a_0 \ln(R_{\rm ap}) \,], \tag{1.4}$$

where $a_0 = S(< R_{\rm ap})$ is the total intensity inside the aperture radius $R_{\rm ap}$, and

$$P_{\rm m} = \frac{1}{2m^2 R_{\rm ap}^{2m}} \left(a_m^2 + b_m^2\right), \tag{1.5}$$

where the moments a_m and b_m are given by

$$a_m(R) = \int_{R' \leq R_{\rm ap}} S(x')(R') \cos(m\phi') d^2x'$$

$$b_m(R) = \int_{R' \leq R_{\rm ap}} S(x')(R') \sin(m\phi') d^2x'$$

where $S(x)$ is the X-ray surface brightness. Usually P_3/P_0 is the power ratio used as it is the lowest moment that provides a measure for substructure in clusters. The centroid shift (Poole et al., 2006, Maughan et al., 2008) estimates the projected separation between the X-ray peak and the centroid inside circular apertures around the X-ray peak of the cluster. The concentration parameter (Santos et al., 2008) measures the fraction of the surface brightness in a cluster measured, say, 100 kpc from the cluster centre compared to the total surface brightness from 500 kpc around the cluster. An analysis of galaxy clusters (Cassano, 2010, Buote, 2001) (Figure 1.8) showed that clusters that were morphologically disturbed i.e. clusters that showed signs of recent or ongoing mergers were much more likely to host radio halos than those that did not.

The mechanism by which the energy generated during cluster mergers is transferred to electrons and accelerates them to relativistic levels is briefly discussed below.

A merger between clusters with typical relative velocities $\sim 10^3$ km s^{-1} can release gravitational energy $\sim 10^{64}$ erg s^{-1} . Even a few % of this energy is sufficient to accelerate electrons in the ICM to energies ~GeV (Brunetti and Lazarian, 2007, Cassano and Brunetti, 2005, Brunetti and Lazarian, 2011). The ICM in galaxy clusters contains

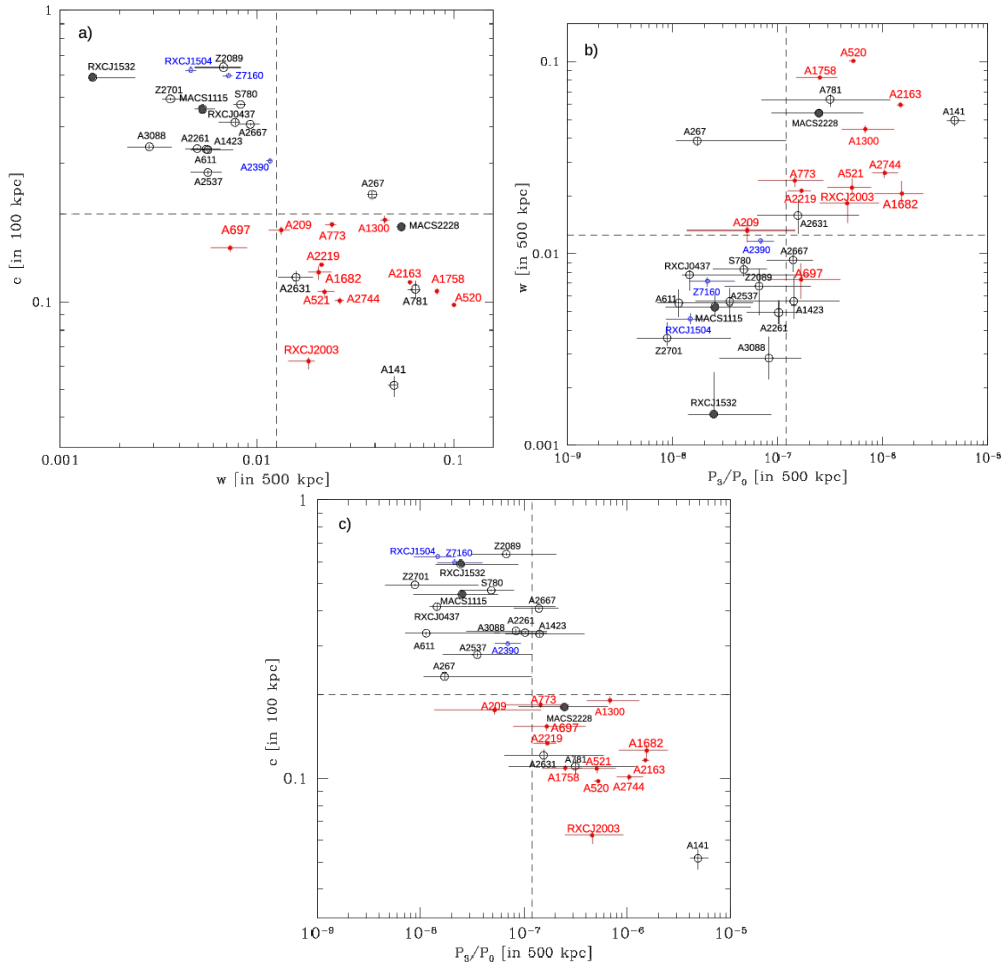

FIGURE 1.8: Cluster morphology parameters (Cassano, 2010). Clusters in red contain halos while clusters in black do not. *Top Left:* Concentration parameter (c) vs. centroid shift (w). *Top Right:* w vs. power ratio (P_3/P_0). *Bottom:* c vs. P_3/P_0. The vertical and horizontal dashed lines correspond to $c = 0.2, w = 0.012$ and $P_3/P_0 = 1.2 \times 10^{-7}$.

thermal electrons (responsible for thermal bremsstrahlung radiation) as well as non-thermal electrons (emissions from galaxy AGNs etc.) However, reacceleration of thermal electrons is an extremely energy inefficient process (Petrosian, 2001). Consequently, the generation of radio halos in galaxy clusters is a two-step process – first, an initial injection of relativistic *seed* electrons into the ICM followed by a reacceleration phase where these seed electrons are accelerated to relativistic levels (Brunetti et al., 2001a,b).

Numerical simulations confirm that turbulence is generated at the time of a cluster merger due to the displacement of gas from the cluster centres over length scales, $L \sim$100s of kpc (Brunetti et al., 2004, Brunetti and Lazarian, 2011, Ricker and Sarazin, 2001). A few % of the thermal energy of the cluster can be injected into the turbulence during such a merger (Cassano and Brunetti, 2005). This large-scale fluid turbulence then cascades to smaller scales where the energy from the fluid turbulence is transferred to

MHD (Magneto-HydroDynamic) waves which are responsible for accelerating the electrons in the medium. The mechanism by which MHD waves interact with particles can be through Alfveń waves (Fujita et al., 2003, Brunetti et al., 2004), fast or slow magnetosonic (MS) waves (Brunetti and Lazarian, 2007, 2011) or even turbulent reconnection (Brunetti and Lazarian, 2016). In all these cases, the efficiency of electron acceleration and the damping process by which they lose energy are important factors that are not completely understood and are still a matter of debate.

1.3.2 Secondary Model

An alternative to the primary model is the *secondary* or *hadronic model* that uses the presence of long-living high energy protons to explain the generation of relativistic electrons in galaxy clusters (Dennison, 1980, Blasi and Colafrancesco, 1999, Dolag and Enßlin, 2000).

Relativistic particles are injected into the medium constantly through supernova explosions and emissions from the AGNs at the centre of galaxies. In the case of protons, the energy losses are dominated by the inelastic *p-p* collisions at relativistic energies ($E > GeV$) and ionization and Coulomb scattering at mildly relativistic energies. The radiative lifetime of such high energy protons is estimated to be $\sim 10^{10}$ years. This is sufficient time for the protons to diffuse through the Mpc-sized cluster.

The *p-p* collisions produce secondary particles through the following interaction (Blasi and Colafrancesco, 1999):

$$p + p \rightarrow \pi^0 + \pi^+ + \pi^- + \text{anything}$$
$$\pi^0 \rightarrow \gamma\gamma$$
$$\pi^\pm \rightarrow \mu^\pm + \nu_\mu(\bar{\nu}_\mu), \quad \mu^\pm \rightarrow e^\pm + \bar{\nu}_\mu(\nu_\mu) + \nu_e(\bar{\nu}_e)$$

This interaction only requires a proton threshold energy of 300 MeV. The resulting spectrum of the electrons is expected to be a power-law without any breaks which is at odds with the spectral steepening seen in the prototypical radio halo in the Coma cluster (Thierbach et al., 2003). The production of gamma rays as another secondary consequence of this reaction is also an important prediction of this theory. However, gamma ray observations of galaxy clusters have not been able to detect any such emissions (Reimer et al., 2003, Ackermann et al., 2010, Jeltema and Profumo, 2011). Only upper limits have been placed on the expected gamma ray emission. Another issue is

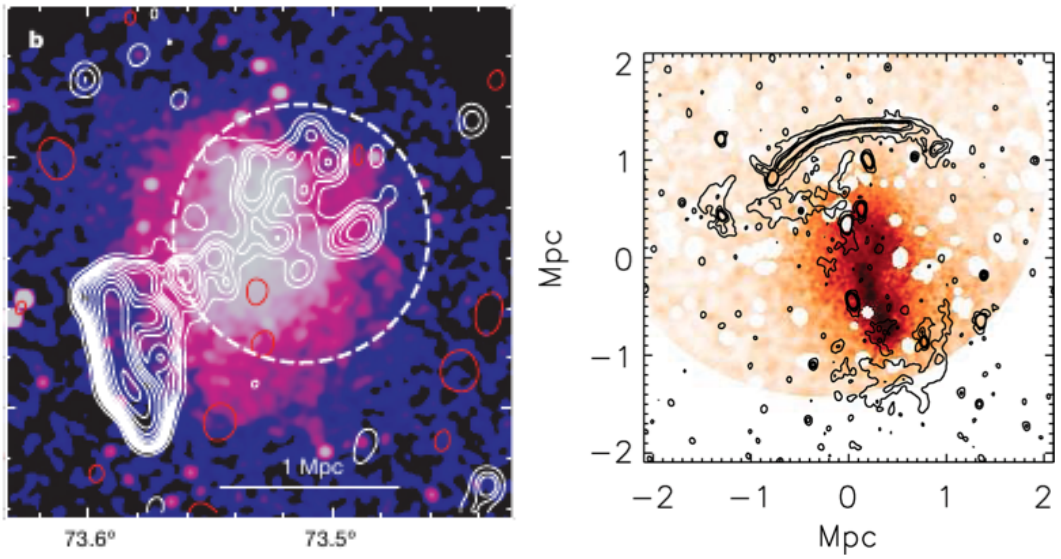

FIGURE 1.9: *Left:* GMRT 610 MHz contours of the cluster A521 at $35'' \times 35''$ resolution overlaid on the *Chandra* X-ray image. RMS in the region is 58 μJy/beam. Right: WSRT 1.4 GHz contours of the cluster CIZA J2242.8+5301 overlaid on the *XMM-Newton* X-ray image. The resolution of the radio image is $16.5'' \times 12.9''$ and an RMS of 19μJy/beam.

that since relativistic protons can be expected to be found in all clusters one would expect synchrotron emission from secondary electrons to be found in all clusters as well. However, as mentioned before, a very small fraction of galaxy clusters are known to host radio halos. It should be noted that the strength of the secondary model is predicted to be weaker than the primary model (Brunetti and Lazarian, 2011) and as such more sensitive radio observations of galaxy clusters are required to detect emission from these secondary electrons.

1.4 Radio Relics

In addition to radio halos, diffuse emission from the ICM in galaxy clusters is also seen in the form of radio relics. These objects are usually elongated and arc-like in nature with significant polarization $(10 - 40\%)$ and are found towards the peripheries of galaxy clusters. They can vary in size with 100s of kpc to ∼Mpc sized relics having been detected in some clusters. Relics in clusters are found with or without an accompanying halo. Additionally, in some clusters double relics are found on opposite ends of the X-ray distribution. Figure 1.9 shows two examples of clusters with relics.

In each figure the colour image in the background shows the X-ray emission of the cluster with the radio contours overlaid on top. The relic emission can be seen towards the edge of the X-ray emission.

The origin of radio relics is attributed mainly to the shocks that travel outwards in the aftermath of a cluster merger. The relics are believed to trace these outgoing shocks. This idea is supported by the observation that in clusters with double relics the two relics lie on the cluster merger axis. The theory that explains the acceleration process of electrons in shocks is discussed below.

The Diffusive Shock Acceleration (DSA) theory is a first order Fermi process wherein the acceleration of electrons takes place across the shock. As the electrons diffuse through the shock and bounce off the two shock fronts they gain energy with each reflection and can reach energies ∼GeV (Blandford and Eichler, 1987, Jones and Ellison, 1991). While the DSA is the most prominent theory considered to explain the origin of radio relics there are still some unanswered questions. The Mach number of the shocks generated during cluster mergers (Markevitch and Vikhlinin, 2007) (as estimated through simulations and X-ray observations) is small ($M \lesssim 3$). The efficiency of electron acceleration with such shocks is expected to be poor (Kang et al., 2002). While it should be mentioned that this issue can be resolved by assuming a pre-existing seed population of relativistic electrons (Kang and Ryu, 2011) it is still unclear if DSA is truly responsible for the origin of radio relics (Vazza and Brüggen, 2014, Vazza et al., 2015, 2016).

1.5 Studies on Radio Halos and Relics

Since the discovery of the first radio halo (Coma; Willson (1970)) there has been a lot of effort by the scientific community to discover more clusters which host radio halos and relics. Traditionally, most radio halos and relics have been discovered through follow-up radio observations of X-ray detections of galaxy clusters.

The first large scale search for radio halos and relics in galaxy clusters was by Giovannini et al. (1999) where the cluster sample used was from the X-ray brightest Abell-type clusters (XBACs) by Ebeling et al. (1996). They used images of these clusters at 1.4 GHz from the NRAO-VLA Sky Survey (NVSS) to detect possible halo and relic emission. The survey was carried out in the D-configuration of the VLA and covered the entire sky above a declination of $-40°$. The D-configuration of the VLA includes the shortest baselines and was thus fairly sensitive to extended emission. The angular resolution achieved by the survey was $45''$ and a sensitivity level of 0.45 mJy beam^{-1} . Of the 283 brightest X-ray clusters ($f_X > 5 \times 10^{-12}$ erg cm^{-2}s^{-1}) in the sample below a redshift of $z \leq 0.2$, radio halos and relics were detected in 29 clusters. The trend of highly X-ray luminous clusters being more likely hosts to halos and relics was first seen here with only $\sim 10\%$ of clusters with $L_X \leq 10^{45}$ erg s^{-1} showing the presence of any diffuse sources.

On the other hand nearly a third of the clusters with $L_X > 10^{45}$ erg s^{-1} had halos or relics in them.

One of the biggest shortcomings of this study was the lack of short-spacings in the VLA (even in the D-configuration) because of which the NVSS was not sensitive to emission larger than $15'$. This is important at low redshifts where the angular size for Mpc sized objects is quite large ($\theta_b \sim 10'$ at $z = 0.1$). The radio halo in the Coma cluster ($z = 0.0232$) was resolved out in the NVSS images. Additionally, the primary model of halo formation predicts a steepening of the electron spectrum at higher frequencies. As a result it is likely that the survey missed detection of steep spectrum halos ($\alpha < -1.3$, see for e.g. Dallacasa et al. (2009)). Low frequency observations are thus better suited for the detection of diffuse, extended emission of radio halos and relics.

The GMRT [1] Radio Halos Survey (GRHS) (and its follow up, the Extended GMRT Radio Halos Survey) which was carried out at 235 and 610 MHz was a step in this direction (Kale et al., 2015, Venturi et al., 2008, Kale et al., 2013, Venturi et al., 2007). The cluster sample used for this survey was the ROSAT-ESO Flux Limited X-ray (REFLEX) catalogue (Böhringer et al., 2004) and the extended ROSAT Brightest Cluster Sample (BCS) catalogue (Ebeling et al., 1998, 2000). Only clusters in the redshift range $0.2 < z < 0.4$ with X-ray luminosity $L_{X[0.1-2.4keV]} > 5 \times 10^{44}$ erg s^{-1} were studied. This luminosity cut-off was put so as to maximize the possibility of detecting giant radio halos ($R_H \gtrsim 700$ kpc) in the given redshift range (Cassano et al., 2006, 2004). The resolution of the survey was $\sim 10''$ with a noise level ~ 0.1 mJy beam^{-1} . Of the 64 clusters observed, diffuse emission was detected in 30 clusters and upper limits to halo emission were placed in 30 clusters (Figure 1.6). Additionally, the survey also demonstrated the *bi-modal* nature of halo emission in galaxy clusters. In clusters where no halos were detected, upper limits to possible halo emission were placed (arrows in Figure 1.6) which were a factor of 10 below the best-fit in the empirical $L_X - P_{1.4}$ relation. Whether these clusters genuinely don't contain halos or are merely below the GMRT detection limits is still unclear.

A possible reason why GMRT could have missed out on detecting halos and relics in these clusters is that GMRT observations suffer from two major issues: lack of good short-spacing data and RFI (Radio Frequency Interference), especially at the lowest frequencies. Future observations with telescopes like the Murchison Widefield Array (MWA), the LOw Frequency Array (LOFAR) and the Square Kilometer Array (SKA), which do not suffer from RFI and will provide better *uv*-coverage and thus better sensitivity to diffuse extended emission from radio halos and relics, will be needed to confirm the presence or absence of diffuse emission, particularly in low X-ray luminosity clusters.

[1] Giant Metrewave Radio Telescope

1.6 This thesis

Diffuse radio emission in galaxy clusters is still poorly studied in literature. There are only ~ 100 halos and relics that have been detected. Most of these detections were made using radio observations at 1.4 GHz or above. There exist very few observations of halos and relics at lower frequencies (< 1 GHz). It is important to observe galaxy clusters at low frequencies because:

- The spectra of halos and relics at lower frequencies is not known very well. Multi-frequency observations of these sources exist for very few sources (Feretti et al., 2012). If spectral steepening of the radiating electrons at high frequencies is taking place (as predicted by the primary model) then low frequency observations are crucial to check the spectral behaviour of radio halos and relics over a large range of frequencies.
- Since most radio halos and relics are known to have steep spectra ($\alpha < -1, S \propto \nu^{\alpha}$) it is possible that due to sensitivity limitations, the current generation of telescopes would have missed them. Thus low frequency observations are important to detect these missing halos and relics where possible or at least place upper limits to a possible halo emission.
- Furthermore, at lower redshifts ($z < 0.1$) Mpc sized objects have very large angular scales ($\gtrsim 10'$). High frequency observations would resolve out such extended emissions. Low frequency observations with good uv-coverage will be needed to detect halos and relics at these redshifts.

RFI is a major hindrance for radio observations at low frequencies. It would be beneficial then to use telescopes which do not suffer from these issues to study the weak radio halos and relics.

In **Chapter 2**, we describe the Murchison Widefield Array (MWA), a low frequency telescope operating in the frequency range $80-230$ MHz. The telescope has been built in a radio-quiet region in Western Australia and is a collaborative effort between institutes across the world. The telescopes design and construction will be briefly discussed as well as the system parameters that make it well suited for our purposes. Finally, we will describe the GaLactic and Extragalactic All-Sky MWA (GLEAM) Survey that was carried out using this telescope. The details of the survey will be discussed including the pipeline that was set up to process the data from the telescope and produce images.

In **Chapter 3** we discuss multi-frequency observations of the galaxy cluster Abell 3376 (A3376) using the MWA. A3376 is a low redshift ($z = 0.0456$) cluster which contains

two relics on opposite ends of the cluster X-ray emission. However, the cluster contains no radio halo. The cluster was imaged at all 5 MWA observing frequencies (88, 118, 154, 188 and 215 MHz) and compared with the pipeline images. Spectra for the two relics was obtained over the frequency range $80 - 1400$ MHz and while no halo was detected in the central regions of the cluster, a stringent upper limit was placed. By estimating the spectral ages of the relics of the cluster and comparing those with the dynamical timescale of the cluster, we concluded that any possible halo emission that might have existed in the cluster has quite probably decayed by now.

In **Chapter 4** a sample of merging galaxy clusters identified from their high frequency observations were studied with the MWA. These clusters were claimed to contain relics with or without halos. The GLEAM pipeline images were used to study these clusters. We estimated the spectra of the radio halos and relics over the frequency range $80 - 1400$ MHz and in cases where no halos were detected we placed upper limits to a possible halo emission. The implications of these upper limits to models of halo formation in galaxy clusters is also discussed and in cases where no halos were detected we placed upper limits to a possible halo emission. The implications of these upper limits to models of halo formation in galaxy clusters is also discussed.

In **Chapter 5** we present the first detection of a previously unknown radio relic using the MWA.

Finally, in **Chapter 6** we summarise the results of this thesis and discuss possible future work.

CHAPTER

TWO

THE MURCHISON WIDEFIELD ARRAY (MWA)

2.1 Introduction

The MWA (Lonsdale et al., 2009, Tingay et al., 2013) is a precursor to the upcoming Square Kilometre Array (SKA; Dewdney et al. 2013) telescope. It is located at the Murchison Radio-astronomy Observatory (MRO) in the Murchison region of Western Australia. This remote location was chosen because of the spectacularly low levels of man-made radio interference in this region. Radio Frequency Interference (RFI) is known to be an especially hard to tackle problem at the low frequencies such as those in which the MWA operates. The MWA is a dipole-based aperture array synthesis telescope that operates in the frequency range $80 - 300$ MHz.

Lonsdale et al. (2009) first described the conceptual design of the MWA employing the so-called "large-N" architecture (Hall, 2004) wherein hundreds to thousands of small antenna elements are used to observe the radio sky. This has the benefit of providing an extremely large field-of-view (fov) while simultaneously covering the uv plane comprehensively thus providing sensitivity to large-scale radio emission. However, this does present other challenges such as ionospheric effects which will not be discussed here but have been addressed elsewhere.

While the initial design of the telescope called for 512 antenna elements, or tiles (discussed in the next section), spread over 3 km, the final configuration adopted for the telescope utilises 128 tiles spread over 3km with 50 of the tiles within a 100m diameter core. This is followed by a smooth distribution of 62 tiles out to 1.5km and the remaining 16 tiles in the outer 3km region. This was done to provide good snapshot uv-coverage

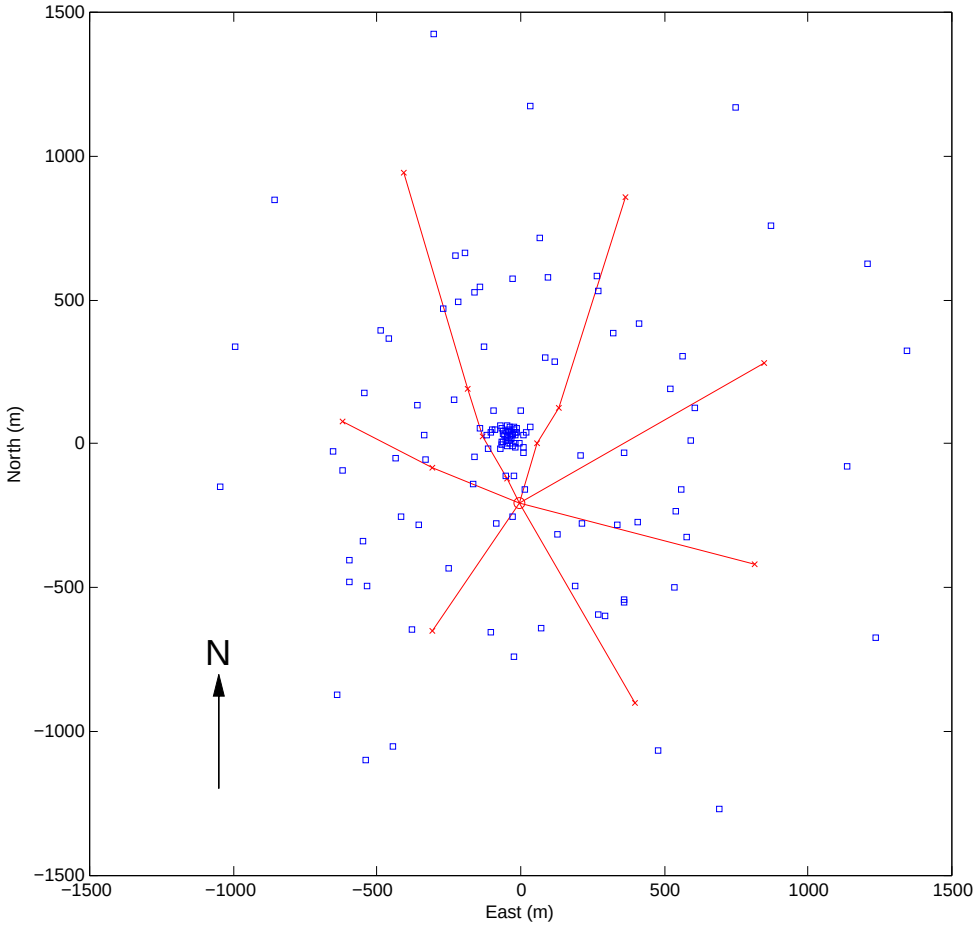

FIGURE 2.1: Distribution of MWA tiles (in blue) on location.

in the central core while still providing longer baselines for good resolutions. The final antenna configuration of the MWA is shown in Figure 2.1. Table 2.1 shows the system parameters for the telescope at 150 and 200 MHz.

Parameter	Symbol	150 MHz	200 MHz
Number of tiles	N	128	128
Area of one tile at zenith (m^2)	A_{eff}	21.5	19.8
Total collecting area (m^2)		2752	2534
Receiver temperature (K)	T_{rcv}	50	25
[a]Typical sky temperature (K)	T_{sky}	350	170
[b]Field of view (deg^2)	Ω_P	610	375
Instantaneous bandwidth (MHz)	B	30.72	30.72
Spectral resolution (MHz)		0.04	0.04
Temporal Resolution		0.5 s uncalibrated 8 s calibrated	0.5 s uncalibrated 8 s calibrated
Polarization		Full Stokes	Full Stokes
Minimum baseline (m)		7.7	7.7
Maximum baseline (m)		2864	2864
Angular resolution (3 km array)		$\sim 3'$	$\sim 2'$

[a] Nijboer et al. (2013).
[b] Based on FWHM of primary beam. Imageable area is significantly larger.

TABLE 2.1: System parameters for MWA

2.2 Bow-Tie Antenna and Tiles

A single antenna element (or, tile) of the MWA comprises of 16 dual-polarization dipoles arranged in a 5m×5m square grid with a 1.1m spacing between them. All 16 elements are placed on a galvanised steel wire mesh which acts as a reflecting screen at the MWA frequencies (Figure 2.2). The signals from the dipoles are combined in such a way so as to allow for pointing in any direction on the sky by changing the delays to each element. The beamformer for each tile produces output for 2 linear polarisations – X and Y. The analog output from 8 tiles are sent to a receiver which applies a bandpass filter in the frequency range $80 - 300$ MHz. The signal is then sampled with an 8-bit Analog to Digital Converter (ADC) which produces 24×1.28 MHz frequency channels. This results in the 30.72 MHz instantaneous bandwidth at every MWA observing frequency. The data from the 16 receivers are then sent to the correlator where every 1.28 MHz channel is then further divided into 128×10 kHz channels. For storage purposes the final data is stored with a temporal resolution of 0.5s and a frequency resolution of 40 kHz.

Figure 2.3 shows the single frequency *uv*-coverage for the MWA.

2.3 Comparison with current telescopes

The MWA is a precursor to the upcoming SKA telescope, part of which is planned to be built at the same location as MWA. With the large FOV that MWA provides surveys are

FIGURE 2.2: MWA tile with the 16 bow-tie dipoles in 4×4 configuration on a 5m×5m steel mesh.

a particularly important project that can be undertaken with the telescope. Figure 2.4 compares the MWA with current and upcoming telescopes in terms of sensitivities as well as FOV.

2.4 GLEAM

The GaLactic and Extragalactic All-sky MWA (GLEAM) Survey (Wayth et al., 2015). was carried out at 5 frequency bands between 72 and 230 MHz, centred on 88, 118, 154, 188 and 215 MHz with 30.72 MHz bandwidth each. Each full band was further divided into four sub-bands of 7.68 MHz bandwidth. The GLEAM Survey was carried out over two years. During the first year, the frequency resolution of the survey was 40 kHz while the time resolution was 0.5s. In the second year, the frequency and time resolutions were changed to 10 kHz and 2s, respectively.

The survey was carried out at seven declination settings
($\delta = +18.6°, +1.6°, -13.0°, -26.7°, -40.0°, -55.0°, -72°$), utilizing a drift-scan method. At the beginning of the observation the telescope was electronically set to one of the seven declinations and measurements were taken sequentially looping over the five frequencies

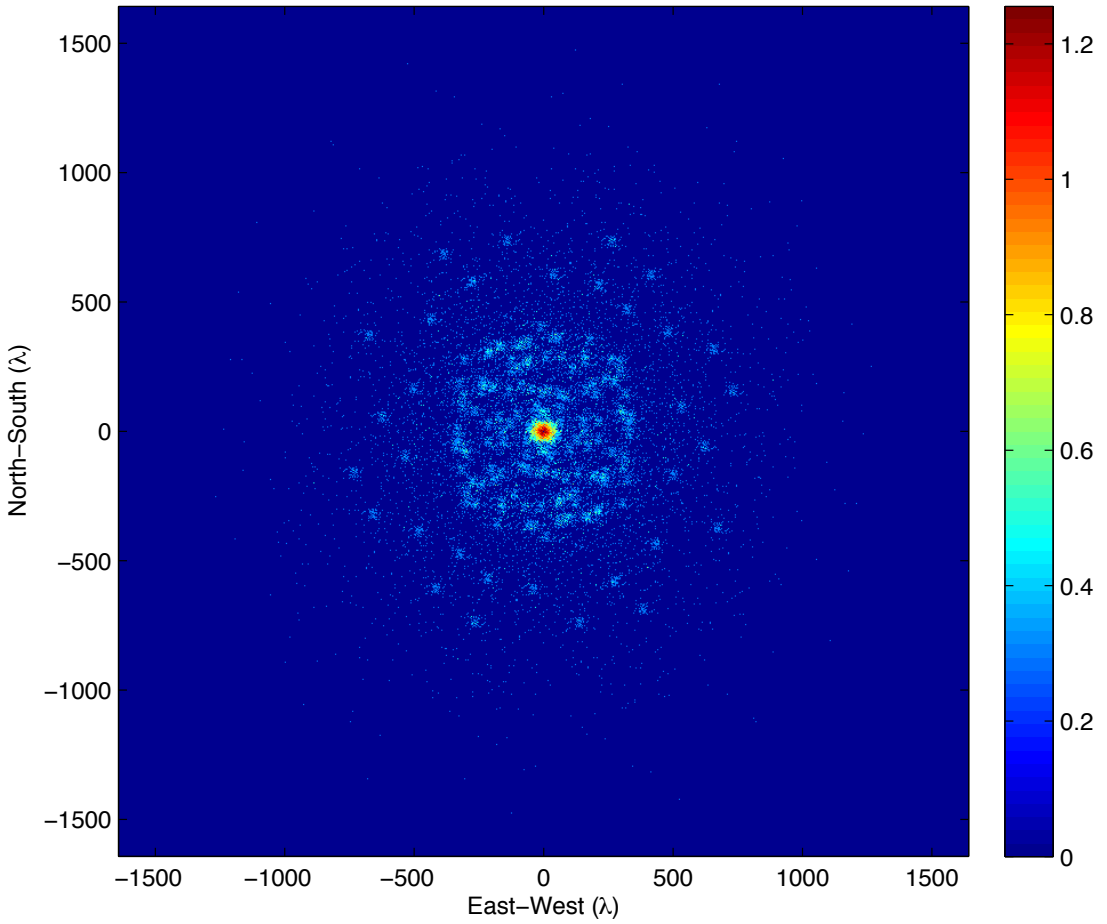

FIGURE 2.3: Snapshot uv-coverage of the MWA.

every two minutes (112 sec) as the sky drifted overhead. A set of calibrators were observed throughout each of the observing nights.

This raw data was then analysed and sent through a pipeline to produce the final images The basic steps of the analysis are as follows.

For each scan:

- A single bright source was used for a first-pass calibration on all the observations (Hurley-Walker et al., 2014);
- Cleaning of the images was performed using WSCLEAN (Offringa et al., 2014);
- The primary beam model for the MWA, as described by Sutinjo et al. (2015), was used to transform to astronomical Stokes;
- Assuming the sky to be unpolarized, Stokes Q, U and V were set to zero and, using the same beam model, converted back to instrumental Stokes;

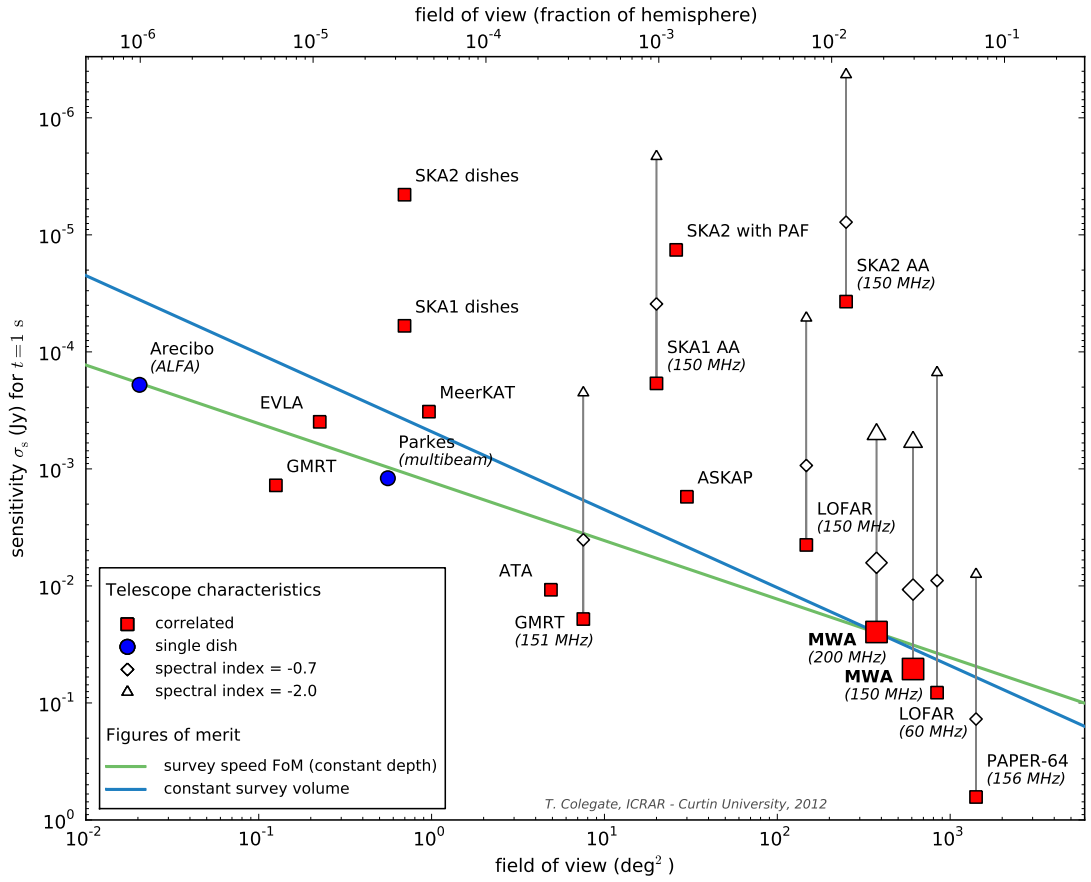

FIGURE 2.4: Comparison of MWA FOV and sensitivities with current and future telescopes.

- Self-calibration was now performed using this new sky model to produce the final multi-frequency synthesis images;

The GLEAM images were calibrated in 3 steps: first, at each frequency, the model of a bright source was used to transfer the complex antenna gains to the entire drift scan data of the night. Second, self-calibration was performed as described earlier. Finally, bright point sources ($> 8\sigma$) were chosen and cross-matched with the VLA Low frequency Sky Survey Redux (VLSSr) at 74 MHz, Molonglo Radio Catalog (MRC) at 408 MHz and NRAO VLA Sky Survey (NVSS) at 1400 MHz. A power law was fit to the spectra of the point sources and based on their expected to observed flux densities, a declination dependant average scaling factor was estimated at every MWA frequency and applied to the images. All the snapshots obtained during a night's observations were then combined in an inverse-noise-weighted fashion to produce mosaics at every frequency. Note that during this procedure, the absolute flux density scale of sources was set to the Baars scale (Baars et al., 1977). Details on all the above procedures can be found in Hurley-Walker et al. (2017).

In addition to the 30.72 MHz bandwidth images, a 60 MHz bandwidth wideband image centred at 200 MHz was created. These wideband images were made using observations in the frequency range $170 - 231$ MHz and provide a compromise between improved sensitivity and resolution and represent the best images to search for diffuse cluster emission. These wideband images have a resolution of $\sim 2''$ and an RMS (Root Mean Square) value of ~ 6 mJy beam^{-1} at 200 MHz.

CHAPTER

THREE

OBSERVING ABELL 3376 WITH THE MWA

3.1 Background

Abell 3376 is a rich, merging galaxy cluster at a redshift of $z = 0.046$ (Struble and Rood, 1999). It has an X-ray luminosity of $L_{X[0.1-2.4\ \mathrm{keV}]} = 2.2 \times 10^{44}$erg s^{-1} (Reiprich and Böhringer, 2002) and a virial mass of $\sim 3.64 \times 10^{14}$ M$_\odot$ (Girardi et al., 1998). Optical observations (Escalera et al., 1994, Durret et al., 2013) indicate the merging status of the cluster by showing the two Brightest Cluster Galaxies (BCG) on the opposite ends of the cluster with the X-ray peak at BCG2 (MRC0600-399) (Fig. 3.1). The BCG1 is a cD galaxy and is considered to be the centre of the main cluster. The BCG2 is an elliptical and its radio counterpart is a bent-jet galaxy. Machado and Lima Neto (2013) simulated the merger of A3376 and compared their simulation results with the X-ray morphology of the cluster. Based on these comparisons they suggest that the merger in A3376 occurred ~ 0.5 Gyr ago between subclusters having a mass ratio of 6:1. VLA observations of this cluster at 1.4 GHz (Bagchi et al., 2006) showed the presence of two arc-like structures in the eastern and western peripheries of the cluster, ~ 1 Mpc away from the cluster centre. These relics are assumed to be due to synchrotron emission from the ICM as a consequence of shock waves travelling outward from the cluster centre soon after the merger. Further radio observations at lower frequencies (150 and 325 MHz) using the Giant Meterwave Radio Telescope (Kale et al., 2012) detected the relics but not a radio halo from the central regions of the cluster (Fig.3.1). The east relic is found to be polarized up to 30% with aligned magnetic field vectors, whereas the west relic is polarized between 5 and 20% and the field vectors are not aligned in any particular direction (Kale et al., 2012).

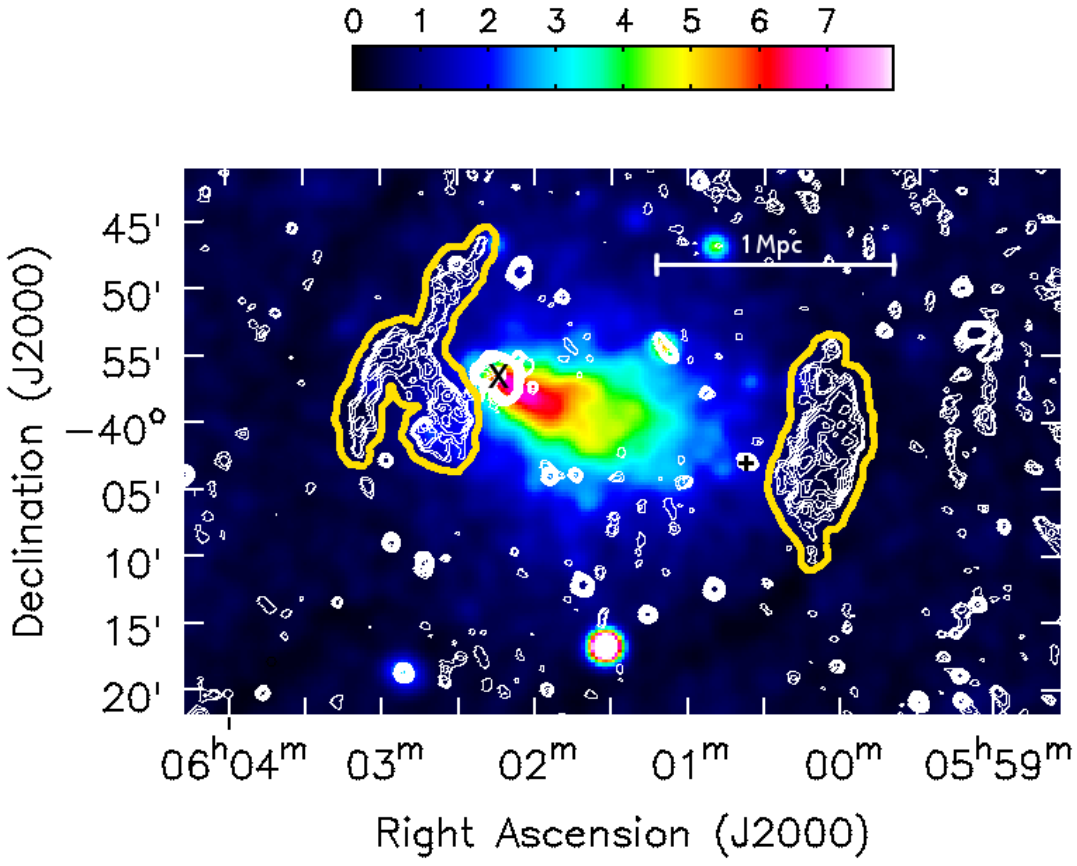

FIGURE 3.1: GMRT 325 MHz contours (Kale et al., 2012) on the ROSAT X-ray (0.1-2.4 keV) broadband image. The units of the X-ray image are in counts s^{-1} $arcmin^{-2}$. The contour levels start from 5.8 mJy $beam^{-1}$ (3σ) and increase by a factor of $\sqrt{2}$. The resolution of the radio image is $39'' \times 39''$. The $\times$ and the $+$ represent the BCG2 and BCG1 galaxies, respectively. The yellow solid line (drawn by the authors) marks the boundaries of the east and west relics.

3.2 Observations and Analysis

3.2.1 The GLEAM Survey

The observations of A3376 were carried out as part of GaLactic and Extragalactic All-Sky MWA (GLEAM) Survey (Wayth et al., 2015). There are five observing frequency ranges: 72.3–103.04 MHz, 103.04–133.76 MHz, 138.88–169.6 MHz, 169.6–200.32 MHz and 200.320–231.04 MHz, each having a bandwidth of 30.72 MHz. The data were recorded with an integration time of 0.5 second and a spectral resolution of 40 kHz. The frequency range 134–138 MHz was avoided due to the presence of satellite RFI (radio frequency interference) in that range.

The GLEAM survey was carried out in the drift-scan mode with the antennas pointing to one of the seven declination settings ($\delta = +18.6°, +1.6°, -13.0°, -26.7°, -40.0°, -55.0°, -72°$)

and letting the sky drift overhead. A single scan consists of observations for 112 seconds at each of the five frequencies available and then cycling through them. The data used for imaging A3376 in this paper were taken during November 6–7, 2013 while covering the RA range 0–8h at declination $\delta = -40°$. This declination pointing is within a few arcminutes of the centre of the cluster (Fig. 3.1).

3.2.2 Data reduction

In principle, one could use the specialised pipeline software that has been set up to analyse the observations from the GLEAM survey (Hurley-Walker, in prep.). However, with the scope to try to analyse the MWA observations using a standard radio astronomy software we imaged the cluster at two frequencies viz. 154 and 215 MHz using CASA [1] (Common Astronomy Software Applications). We chose these two frequencies because at 215 MHz the highest angular resolution in the GLEAM frequency range is achieved ($151'' \times 145''$) and at 154 MHz the MWA images obtained can be directly compared with the existing GMRT observations at 150 MHz. The images at 154 and 215 MHz, processed with CASA, are further compared with the pipeline processed images at the same frequencies. For the remaining frequencies (88, 118 and 188 MHz) we use the pipeline processed images.

The raw data from A3376 scans were converted to measurement sets readable by CASA using the COTTER software (Offringa et al., 2015). This software also performed some initial flagging and RFI removal using the AOFlagger library (Offringa et al., 2010, 2012). The source 3C161 was used to create the normalised bandpass tables (task *bandpass* in CASA) which were applied to all the A3376 scans. In all, a total of seven scans of A3376 were used – the transit scan and three scans on either side of the source's transit through the meridian – which covered a total time range of ±30 minutes around transit at each frequency. The scans beyond this time range were not considered due to the falling gain of the primary beam (i.e. the beam response was falling $< 50\%$). Note that the full widths at half maxima of the primary beams of the MWA tiles are $\sim 25°$ at 154 MHz (Hurley-Walker et al., 2014). The bandpass corrected measurement sets were then averaged in time and frequency to 8 s and 400 kHz, respectively. Each scan was then individually imaged and deconvolved in CASA using the task *clean*. Each image produced (2048×2048 pixels) covered an area of 34.13×34.13 deg^2 in each axis with a pixel size of $1'$. Deconvolution was performed using the Cotton-Schwab algorithm (Schwab, 1984) and widefield effects were taken into account using the w-projection algorithm (Cornwell et al., 2008) by setting the number of projection planes in *clean* to 256.

A variety of robust weighting schemes were tried to make images of A3376. In order to reach a balance between sensitivity and resolution we used "Briggs" weighting (Briggs, 1995) with robust value 0 for each scan at both polarizations. Note that Briggs weighting with values −5 and +5 correspond to purely uniform and purely natural weighting, respectively. The images were then sent through four rounds of phase self-calibration, at the end of which the phase errors had reduced to an rms of 0.2°. No further improvement was seen with subsequent phase and

[1] http://casa.nrao.edu

Object	Flux Density (mJy)				
	88 MHz	118 MHz	154 MHz	188 MHz	215 MHz
East Relic	5476 ± 675	3886 ± 577	2508 ± 465	1508 ± 169	1079 ± 184
West Relic	2805 ± 348	1926 ± 288	1351 ± 253	1172 ± 134	609 ± 108
Central Region	48.5 ± 47	59.5 ± 28.2	22 ± 18	20 ± 12	17 ± 11

TABLE 3.1: The integrated flux densities for the east and west relics along with their uncertainties are given in the first two rows. The third row gives the mean value of the flux density from the central region at different frequencies. These mean values represent upper limits to halo emission in the MWA synthesised beam (∼160 kpc at 154 MHz). The errors quoted on these mean values for the central region are the rms values at the corresponding frequencies.

amplitude self-calibration. The XX and YY polarizations were imaged separately for each scan. They were then corrected for primary beam effects (Sutinjo et al., 2015).

Following the above procedure a total of seven images were produced for A3376 for each polarization. These images were examined separately and their rms values were estimated. Furthermore, the positions of unresolved sources in the GMRT 150 MHz image within a degree from A3376 were compared with their respective positions in the seven MWA 154 MHz images. Across these seven images, the positional offsets for all these sources were constant to within 10% of the MWA synthesized beam size at 154 MHz. At each frequency, the individual primary beam corrected XX and YY images were weighted using the inverse variance of the rms in the respective images and then combined. The final XX and YY images were added together to produce the full total intensity (Stokes I) image.

For the remaining frequencies (88, 118 and 188 MHz), we utilised the pipeline-processed GLEAM images, described in detail in (Hurley-Walker et al., 2017). For each scan, the basic steps of this pipeline are as follows,

- Perform a first-pass calibration using a single bright source, applied to all observations (Hurley-Walker et al., 2014);
- Using WSCLEAN (Offringa et al., 2014), invert and clean multi-frequency-synthesis images in instrumental Stokes, across the full bandwidth, stopping at the first negative clean component;
- Use the MWA primary beam model (Sutinjo et al., 2015) to transform to astronomical Stokes;
- Set Q, U and V to zero (i.e. assume that the sky is unpolarized) and use the same beam model to transform back to instrumental Stokes;
- Use the sky model in a self-calibration loop to update the gain solutions;
- Form new multi-frequency synthesis images.

These individual images were then combined to produce the final total intensity images exactly as described earlier.

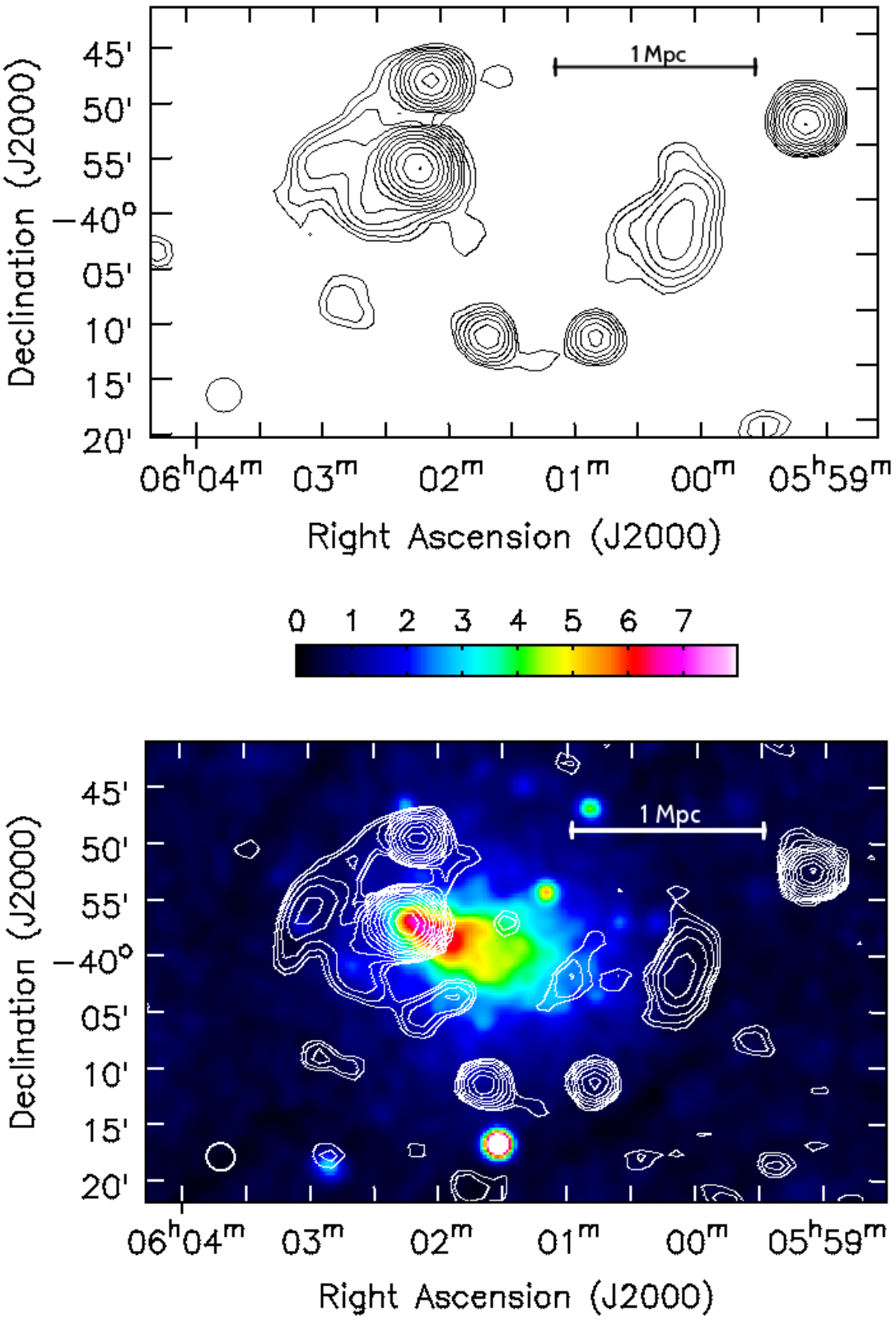

FIGURE 3.2: MWA 154 MHz (top) and 215 MHz (bottom) contour images. The 215 MHz contours are overlaid on ROSAT X-ray (0.1-2.4 keV) image. The units of the X-ray image are in counts s^{-1} $arcmin^{-2}$. Both images have a robust weighting of 0. The 154 MHz image has a resolution of $190'' \times 184''$ $-85.6°$ while the 215 MHz image has a resolution of $151'' \times 145''$, $68.2°$. The synthesised beam is indicated at the bottom left corner in both the images. Contours for the 154 MHz and 215 MHz images start at 54 mJy $beam^{-1}$ (3σ) and 33 mJy $beam^{-1}$ (3σ), respectively, and increase by a factor of $\sqrt{2}$.

3.2.3 Calibration

The absolute flux density calibration of the MWA images was tied to those of the GMRT images at 150 and 325 MHz (Kale et al., 2012). For GMRT calibration, 3C147 and 3C48 as primary calibrators. The Perley and Butler (2013) scale was used for absolute flux density calibration. The secondary calibrators used in the GMRT 150 and 325 MHz observations were 0521-207 and 0837-198, respectively. The flux densities of these two calibrators obtained from GMRT at the two frequencies agree to within 10% of their expected values based on the VLA calibrator list (Kale et al., 2012).

The MWA 154 MHz image was calibrated using the GMRT 150 MHz image. Unresolved sources in the GMRT 150 MHz image within a degree from A3376 were used to estimate an average scaling factor between the GMRT 150 MHz and the MWA 154 MHz images

To calibrate the MWA 215 MHz image, the spectral indices of the same unresolved sources were estimated between the GMRT 150 MHz and 325 MHz images. The extrapolated flux densities at 215 MHz were estimated for these sources. The MWA 215 MHz image was then scaled according to the average value of the scaling factor. The images at 88, 118, and 188 MHz were also calibrated in a manner similar to the one used for calibrating the MWA 215 MHz image.

The images at 154 and 215 MHz made from CASA and from pipeline-processing were compared. At 154 MHz, the rms of the CASA processed image was 18 mJy beam^{-1} (Table 3.1) while that of the pipeline processed image was 13 mJy beam^{-1} . At 215 MHz, the rms of the CASA image was 11 mJy beam^{-1} (Table 3.1) while the pipeline image had an rms of 10 mJy beam^{-1} . The rms of the pipeline images could be expected to reduce further by mosaicking in narrower frequency channels, resulting in fewer excluded images and thus a higher signal-to-noise ratio (Hurley-Walker et al., in prep).

3.3 Results

The MWA images of the Abell 3376 region at 154 and 215 MHz are shown in Fig. 3.2. The images at the other MWA frequencies are not presented here as they are essentially convolved versions of the above images. The Abell 3376 images at 154 and 215 MHz show two prominent relics just outside the region of X-ray emission: one toward the east and the other toward the west of the X-ray emission (compare Fig. 3.1 and 3.2). The two relics are separated by $\sim$ 2 Mpc ($\sim 30'$) from each other. Both the east and west relics were detected at all the MWA frequencies. No diffuse radio emission in the central regions of the cluster (halo) was detected down to the GLEAM sensitivity. Table 3.1 lists the integrated flux densities of the relics and the upper limits on the flux densities of a possible halo in the region between the relics.

There are two primary sources of errors in the estimation of the flux densities of the relics in the MWA images. First, there is an error due to the uncertainties in the flux densities of the unresolved sources used for calibration of the MWA images. This error is estimated to be $\sim$10%. Second, since the relics are extended sources in the MWA observations, the errors in their flux

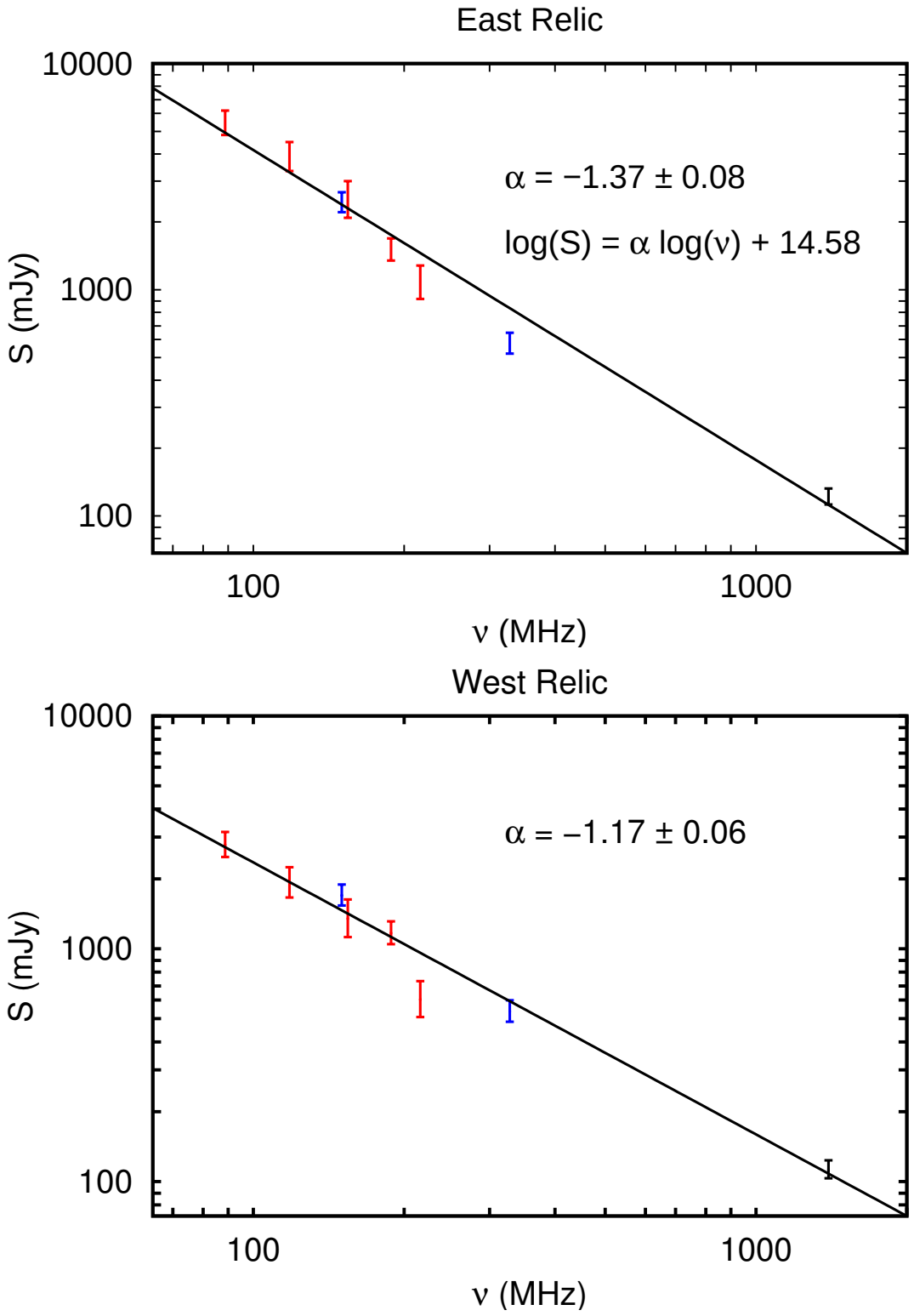

FIGURE 3.3: Spectra for the east and west relics. These spectra include measurements from the GMRT observations at 150 and 325 MHz (Kale et al., 2012) (blue), from the VLA observation at 1.4 GHz (Bagchi et al., 2006) (black) and from the current MWA observations at 88, 118, 154, 188, 215 MHz (red). Also displayed are the best fit lines for the respective data points as well as the spectral index estimates.

density estimations will be the rms in the image multiplied by the square root of the ratio of the solid angle of the relic to that of the synthesized beam. Since these two sources of errors are unrelated, they are added in quadrature to estimate the final error on the flux densities of the relics that are quoted in Table 3.1.

The left and the right panels in Fig. 3.3 show the spectra over the frequency range 80–1400 MHz, for the east and the west relics, respectively. The spectral index of the east relic is -1.37 ± 0.08 while that of the west relic is -1.17 ± 0.06. A least-squares fitting method was used to estimate the spectral index values from the flux density values given in Table 3.1. The reduced-χ^2 values for the fits on the east and west relics were 1.7 and 3.4, respectively.

3.4 Discussion

Abell 3376 shows two arc-like radio relics on either side of the X-ray emission from the cluster. The arcs are oriented roughly perpendicularly to the merger axis of the cluster. Such a scenario is in agreement with the models that predict two outgoing shocks in the aftermath of the merger which are responsible for the radio emission seen from the arcs.

According to the DSA theory (Blandford and Eichler, 1987) the slope of the power law spectrum of the number density of electrons, p, as a function of energy ($N(E) \propto E^p$), is related to the Mach number of the shock, $\mathcal{M}$, by

$$p = -2\frac{\mathcal{M}^2 + 1}{\mathcal{M}^2 - 1} - 1. \tag{3.1}$$

This includes the effects of particle ageing due to inverse Compton and synchrotron radiation losses under the assumption of continuous injection (Sarazin, 1999, Giacintucci et al., 2008). The slope is related to the spectral index (α) of the synchrotron radiation by

$$\alpha = \frac{p + 1}{2}. \tag{3.2}$$

The spectral index is related to the flux density, S, by the standard relation, $S \propto \nu^\alpha$, where ν is frequency. For the east relic, the spectral index is estimated to be -1.37 ± 0.08 which gives the Mach number 2.53 ± 0.23. For the west relic, the spectral index is estimated to be -1.17 ± 0.06, which gives the Mach number 3.57 ± 0.58.

Suzaku X-ray observations by Akamatsu et al. (2012) estimate the Mach number of the East and West relics to be 2.91 ± 0.91. This number agrees with the value obtained from simulations (Machado and Lima Neto, 2013) as well. The Mach numbers estimated here for both the relics are consistent with the X-ray estimates.

The spectra of the relics show no breaks in the frequency range 80 to 1400 MHz. The shock acceleration is expected to produce an initial injection index for the synchrotron radiation close to -0.8. Radiation losses induce a break such that the spectral index after the break steepens by

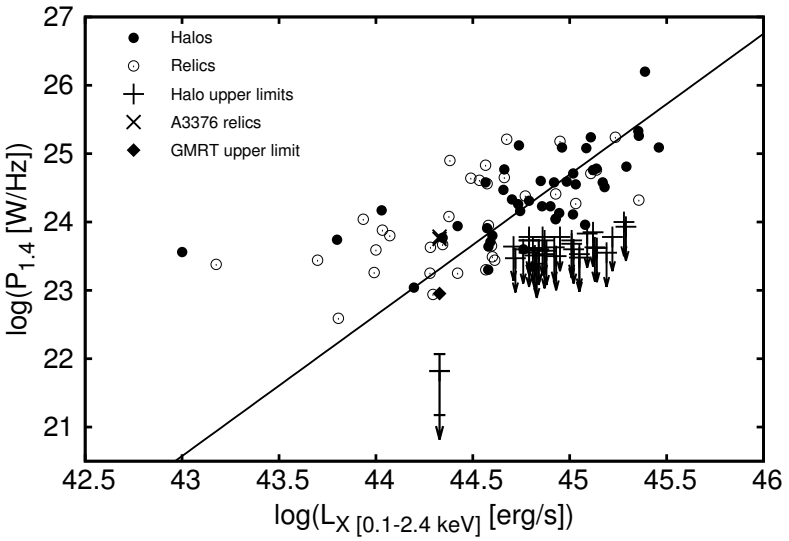

FIGURE 3.4: Plot showing the $L_X - P_{1.4}$ correlation for halos and relics. The filled circles represent all known radio halos. The empty circles represent radio relics (Feretti et al., 2012). The solid line represents the best fit for the $L_X - P_{1.4}$ relation for halos ($\log(P_{1.4}) - 24.5 = 0.195 + 2.06[\log(L_X) - 45]$, Brunetti et al. (2009)). The arrows represent upper limits on halo emission (Venturi et al., 2008, Kale et al., 2013). The cross represents the A3376 relics. The diamond symbol shows the upper limit to halo emission in A3376 as estimated by GMRT while the arrow below it represents the new upper limit as estimated by the MWA.

0.5 to -1.3 (See for example, the relic radio galaxies in Slee et al. (2001)). The average spectral index of the two relics is $\sim$ -1.3. This is consistent with the break frequency being close to or lower than the lower end of the spectrum ($\sim$ 80 MHz) shown in Fig. 3.3. The magnetic field in the cluster can be assumed to be $\sim 1\mu$G (Govoni et al., 2013). We can estimate the spectral ages of the relics as,

$$t = 1060 \frac{B^{0.5}}{B^2 + B_{\rm IC}^2} [(1+z)\nu]^{-0.5}, \tag{3.3}$$

where B is the magnetic field in the source, B_{IC} is the effective Inverse Compton magnetic field, z is the redshift of the source and ν is the break frequency (Slee et al., 2001). Based on these values, the spectral ages of the relics is $\sim$ 0.4 Gyr.

We have made the assumption here that the break frequency is 80 MHz. In reality, this break could be lower than this which would imply that the spectral age is greater than 0.4 Gyr. This estimated spectral age of the relics is, nevertheless, consistent with the age of the cluster ($\sim$ 0.5 Gyr) as obtained from simulations discussed later in this section.

The cluster merger responsible for the generation of the observed relics also generates turbulence in the ICM which is believed to be able to re-accelerate electrons in the region between the relics (Petrosian, 2001, Brunetti et al., 2001c). The region between the relics is then expected to host a radio halo. No such radio halo is detected at the MWA frequencies. However, we have been able to put an upper limit to the flux density from a possible halo in the central region of A3376. Table 3.1 lists the mean flux densities observed in the central regions of A3376 in the MWA

images. The mean value of the spectral index of halos is -1.34 ± 0.28 (Feretti et al. (2012)). An upper limit to the radio power of a halo at 1.4 GHz can be estimated using the upper limit at 154 MHz (Table 3.1) and extrapolating it to 1400 MHz using the mean value of the spectral index quoted here. This power corresponds to 6×10^{21} W Hz^{-1}.

The upper limit is plotted in Fig 3.4 where the radio powers at 1.4 GHz and the corresponding X-ray luminosities of known halos and relics are also plotted (Brunetti et al., 2009). The solid line represents the best fit to the known halos. The upper limit on the radio power of the A3376 halo is lower by a factor of ∼35 compared to that expected from the best fit line.

The upper limit on the radio power of the halo corresponds to a halo size of ~ 160 kpc ($\sim 3'$) at 154 MHz. This corresponds to the beam size at 154 MHz. If the halo is more extended than this, even with higher total radio power, it will be undetected because of limits on surface brightness sensitivity. For a canonical halo as extended as 500 kpc, the upper limit on the radio power would still be lower by a factor of ~ 4 as compared to that expected from the best-fit value.

In order to explain why no radio halo is detected in this cluster we first need to discuss some of the time scales involved in the merger process. The separation between the two relics of A3376 is ~ 2 Mpc. Simulations by Machado and Lima Neto (2013) estimate that the shock velocity, v_s, is ~ 2000 km s^{-1} with an estimated dynamical timescale, $t_{dyn} \sim 0.49$ Gyr. This agrees with their simulations of the gas morphology which puts the cluster at approximately 0.5 Gyr after central passage.

MHD turbulence generated in cluster mergers has a decay time associated with it which is given by Cassano and Brunetti (2005),

$$\tau_{kk}(\mathrm{Gyr}) \sim \left(\frac{v_i}{2000 \text{ km s}^{-1}}\right)^{-1} \left(\frac{L_{inj}}{1 \text{ Mpc}}\right) \left(\frac{\eta_t}{0.25}\right)^{-1}, \tag{3.4}$$

where v_i is the relative velocity of the merging clusters at the time of impact and η_t is defined as the fraction of energy in the form of turbulence that is converted into magnetosonic (MS) waves. This means that the value of η_t defines the efficiency with which the electron population is re-accelerated. The value of η_t can be approximated to 0.25 by using the constraint that the slope of the radio spectrum of the halos is in the range, $\alpha = 1.1 - 1.5$ (Kempner and Sarazin, 2001). The value of v_i is estimated from simulations (Machado and Lima Neto, 2013) to be ~ 1500 km s^{-1}. The typical injection length scale (L_{inj}) of turbulence in galaxy clusters is $200 - 300$ kpc (Brunetti and Lazarian, 2011). With these values in the above equation, the decay time of turbulence for a cluster like A3376 is estimated to be $0.25 - 0.4$ Gyr. Considering that it is now ~ 0.5 Gyr since core passage of the cluster, most of the turbulence that would have been generated at the time of merger would have dissipated. Furthermore, the half-life of these radio emitting electrons is short, ~ 0.3 Gyr (Slee et al., 2001). Any radio halo that was generated during the cluster merger is likely dissipated.

It has been postulated that in galaxy clusters there should be a long-lived component of cluster-wide diffuse radio emission that is generated by relativistic electrons which are continuously injected into the IGM by relativistic proton - thermal proton collisions (Brunetti and Lazarian,

2011). The radio power of diffuse emission expected from these secondary particles is expected to be at a level that is about an order of magnitude lower than that of the radio powers in halos that are detected. The upper limit on the radio power of a halo in Abell 3376 is nearing such levels. While the current limit is close to such a level, further lowering of these limits either in this cluster or in other clusters will have implications for the secondary models of halo production.

3.5 Summary

In this paper, we present low frequency radio observations of Abell 3376 using the Murchison Widefield Array at 88, 118, 154, 188 and 215 MHz. The observations were carried out as part of the GaLactic and Extragalactic All-sky MWA (GLEAM) survey. The observations were analysed using Common Astronomy Software Applications (CASA) tools as well as specialised software packages written to process the GLEAM data. Images were produced at all frequencies. Towards the east and west peripheries of the cluster bright arcs of radio emission (relics) were detected at all frequencies. These arcs, with a linear extent of ~ 1 Mpc each, are a result of outgoing shocks produced by the merger event and are separated by ~ 1 Mpc from the cluster centre. Spectra for both the relics were estimated using the flux densities estimated from the MWA images along with those from previous observations of GMRT at 150 and 325 MHz and of VLA at 1400 MHz. The spectral indices of the east and west relics over the frequency range 80-1400 MHz are -1.37 ± 0.08 and -1.17 ± 0.06 respectively. The Mach numbers of the shocks estimated from these indices are consistent with those estimated from *Suzaku* X-ray observations. Assuming that the break frequency due to radiation losses corresponds to the lower end of the spectrum, the age of the relics can be estimated to be ~ 0.37 Gyr. This age is consistent with the age of the cluster estimated from simulations to be ~ 0.5 Gyr.

No diffuse radio emission was detected in the region between the relics. The upper limit on the radio power of any possible halo of 160 kpc size is $\sim 6\times 10^{21}$ W Hz^{-1} at 1.4 GHz. This is a factor of 35 lower than that expected from the correlation between radio powers and X-ray luminosities of cluster halos. It is very likely that the radio emission from the halo has substantially decayed over its age (~ 0.37 Gyr) considering that this time scale is comparable to the life time of the radiating electrons at the MWA observing frequencies. The upper limit on the radio power of a halo in Abell 3376 is a factor of 10 lower than most upper limits available so far and is nearing levels at which radio emission from secondary electrons produced in relativistic proton - thermal proton collisions is expected. Given the uncertainties in the hadronic model (Brunetti and Lazarian, 2011) it is not possible to discuss the validity of the model based on the observations of the cluster alone. However, observations of a large number of clusters with MWA and LOFAR at the current limits of detection or using the SKA at improved sensitivities will have implications on the hadronic model.

CHAPTER

FOUR

RADIO HALOS AND RADIO RELICS WITH THE MWA

Based on *George et al., 2017, MNRAS*

4.1 Introduction

Radio haloes are known to exhibit an empirical correlation between the radio power of the halo at 1.4 GHz and the X-ray luminosity of the galaxy cluster that hosts the halo (Brunetti et al., 2009, Bacchi et al., 2003, Liang et al., 2000, Brunetti et al., 2007, Feretti, 2000, Govoni et al., 2001b). Recent GMRT (Giant Metrewave Radio Telescope) observations of galaxy clusters (Venturi et al., 2008, 2007) also found that galaxy clusters show a *bi-modal* nature in the $L_{\rm X} - P_{1.4}$ plot. In many clusters where no radio halo was detected, upper limits to the halo emission were placed that are a factor of 2–3 below the expected radio power. While it is possible that these clusters do not contain any radio haloes at all, it could also just be that at the sensitivity limits of the current generation of radio telescopes (e.g. GMRT, JVLA (Jansky Very Large Array)) any possible weak halo emission from clusters is not detectable. However, if the hadronic model is to be believed then there will always be a component of diffuse radio emission in galaxy clusters due to relativistic protons.

For this reason it is important to study non-detections of radio haloes just as much as detections. Using next generation telescopes like the MWA (Lonsdale et al., 2009, Tingay et al., 2013, Bowman et al., 2013), LOFAR (LOw Frequency ARray, van Haarlem et al. 2013) and the upcoming SKA (Square Kilometer Array, Dewdney et al. 2013), which have better low surface brightness sensitivity and uv-coverage at short baselines as compared to existing telescopes, it could be possible to detect previously undetected radio haloes. The radio power in these haloes will also tell us what fraction of the power in haloes is contributed due to the hadronic model as compared to the turbulence model.

With this in mind, we decided to observe merging galaxy clusters with the MWA. These clusters were chosen from literature on the basis of their position in the sky (Southern Hemisphere) as well as existing observations of the cluster and whether or not any haloes and/or relics were detected in them. Based on the above criteria we came up with a list of 9 galaxy clusters all of which are claimed to host a halo and/or a relic based on higher frequency (1.4 GHz) observations. These clusters are – **Abell 13, Abell 548b, Abell 2063, Abell 2163, Abell 2254, Abell 2345, Abell 2744, PLCK G287.0+32.9 and RXC J1314.4-2515.**

In section 2, we give the details of the observations of these clusters made with the MWA as well as with the GMRT. The primary results of the paper are given in Section 3, with a discussion of these results in Section 4. The main conclusions of the paper are summarized in Section 5. The cosmology used in this paper is as follows: $\Omega_0 = 0.3, \Omega_\Lambda = 0.7, H_0 = 68$ km/s/Mpc

4.2 Observations and Analysis

4.2.1 GLEAM Survey Images

The clusters studied in this paper were observed as part of the GaLactic and Extragalactic All-sky MWA (GLEAM) Survey (Wayth et al., 2015). The survey was carried out at 5 frequency bands between 72 and 230 MHz, centred on 88, 118, 154, 188 and 215 MHz with 30.72 MHz bandwidth each. Each full band was further divided into four sub-bands of 7.68 MHz bandwidth. The GLEAM Survey was carried out over two years. During the first year, the frequency resolution of the survey was 40 kHz while the time resolution was 0.5s. In the second year, the frequency and time resolutions were changed to 10 kHz and 2s, respectively. For our purposes we used the year one data.

The survey was carried out at seven declination settings
($\delta = +18.6°, +1.6°, -13.0°, -26.7°, -40.0°, -55.0°, -72°$), utilizing a drift-scan method. At the beginning of the observation the telescope was electronically set to one of the seven declinations and measurements were taken sequentially looping over the five frequencies every two minutes (112 sec) as the sky drifted overhead. A set of calibrators were observed throughout each of the observing nights.

This raw data was then analysed and sent through a pipeline to produce the final images used in this paper. The basic steps of the analysis are as follows.

For each scan:

- A single bright source was used for a first-pass calibration on all the observations (Hurley-Walker et al., 2014);
- Cleaning of the images was performed using WSClean (Offringa et al., 2014);
- The primary beam model for the MWA, as described by Sutinjo et al. (2015), was used to transform to astronomical Stokes;

- Assuming the sky to be unpolarized, Stokes Q, U and V were set to zero and, using the same beam model, converted back to instrumental Stokes;
- Self-calibration was now performed using this new sky model to produce the final multi-frequency synthesis images;

The GLEAM images were calibrated in 3 steps: first, at each frequency, the model of a bright source was used to transfer the complex antenna gains to the entire drift scan data of the night. Second, self-calibration was performed as described earlier. Finally, bright point sources ($> 8\sigma$) were chosen and cross-matched with the VLA Lowfrequency Sky Survey Redux (VLSSr) at 74 MHz, Molonglo Radio Catalog (MRC) at 408 MHz and NRAO VLA Sky Survey (NVSS) at 1400 MHz. A power law was fit to the spectra of the point sources and based on their expected to observed flux densities, a declination dependant average scaling factor was estimated at every MWA frequency and applied to the images. All the snapshots obtained during a night's observations were then combined in an inverse-noise-weighted fashion to produce mosaics at every frequency. Note that during this procedure, the absolute flux density scale of sources was set to the Baars scale (Baars et al., 1977). Details on all the above procedures can be found in Hurley-Walker et al. (2017). For most of the sources used in this paper, the uncertainties in their flux density measurements is $\sim 8\%$. The images used in this paper are all taken from the GLEAM survey.

In this chapter we make use of the 30.72 MHz bandwidth images centred at 88, 118 and 154 MHz in addition to the 60 MHz bandwidth wideband image centred at 200 MHz. These wideband images were made using observations in the frequency range $170 - 231$ MHz. These wideband images compromise between improved sensitivity and resolution and represent the best images to search for diffuse cluster emission. These wideband images have a resolution of $\sim 2''$ and an RMS (Root Mean Square) value of ~ 6 mJy beam^{-1} at 200 MHz.

Estimation of RMS values in the GLEAM images was carried out using the software package Background And Noise Estimation (BANE) written by Paul Hancock [1]. The standard method of estimating RMS from an image would be to estimate the mean and standard deviation in a fixed size box around every pixel in the image and then average it. However, this method is extremely time consuming and will also be biased due to the presence of sources in the image.

BANE uses a slightly modified version of this algorithm to quickly and accurately estimate the RMS of an image. The software works on the principle that there is a high degree of correlation between adjacent pixels in a radio image. As such, it is not necessary to estimate the mean and standard deviation in a box at every pixel. Instead, boxes are drawn around every N^{th} pixel and, first, contribution from the source pixels is removed by masking pixels greater than 3σ. This sigma clipping is performed three times and then, instead of the mean, the median is estimated for each grid and interpolated to produce the background image. The same process is repeated on the background subtracted image (data–background) and then the standard deviation of the image is estimated.

[1] https://github.com/PaulHancock/Aegean/wiki/BANE

4.2.2 TGSS Images

The TGSS[2] is a fully observed survey of the radio sky at 150 MHz as visible from the GMRT, covering the full declination range of -55 to +90 degrees. Data was recorded in half polarization (RR,LL) every 2 seconds in 256 frequency channels across 16 MHz of bandwidth (140–156 MHz). Each pointing was observed for about 15 minutes, split over 3 or more scans spaced out in time to improve UV-coverage. As a service to the community, this archival data has been processed with a fully automated pipeline based on the Source Peeling and Atmospheric Modelling (SPAM) package (Intema et al., 2009, Intema, 2014), which includes direction-dependent calibration, modelling and imaging to suppress mainly ionospheric phase errors.

In summary, the pipeline consists of two parts: a *pre-processing* part that converts the raw data from individual observing sessions into pre-calibrated visibility data sets for all observed pointings, and a *main pipeline* part that converts pre-calibrated visibility data per pointing into stokes I continuum images. The flux density scale is set by calibration on 3C48, 3C147 and 3C286 using the models from Scaife and Heald (2012). More details on the processing pipeline and characteristics of the data products can be found in the article on the first TGSS alternative data release (ADR1; Intema et al. 2016). For this study, ADR1 images were used to create mosaics at the cluster positions. These images have a resolution of ~ 25" and an RMS of ~ 5 mJy beam^{-1} at 150 MHz.

The primary purpose of using the TGSS images is that since they have better resolution than the GLEAM images it would be easier to detect any blending of unrelated sources that might occur with the haloes and relics. Such sources could then be identified and their flux densities subtracted in order to accurately estimate the flux densities of the haloes and relics.

4.3 Results

In Table 4.1 we give the RMS values of the GLEAM images used in this paper as well as those of the TGSS 150 MHz images at two separate resolutions, the original 25" images and images tapered to 60" to highlight the diffuse nature of the emission. This table also gives the resolutions of images at all the four GLEAM frequencies. Due to the poor resolution of the GLEAM images, occasionally unrelated sources get blended with the haloes and relics of interest. In order to estimate the flux densities of these haloes and relics at the GLEAM frequencies the flux densities of the unrelated sources were subtracted. Table 4.2 shows the positions of these unrelated sources as well as their flux densities at 200 MHz and their spectral indices. The integrated flux densities of the haloes and relics are given in Table 4.3. Note here that while the TGSS measurements use the calibration scale provided by Scaife and Heald (2012) and the MWA uses the calibration scheme of Baars et al. (1977) the difference between the two scales is $\sim 3\%$ (Hurley-Walker et al., 2017).

[2]TIFR (Tata Institute of Fundamental Research) GMRT Sky Survey; see http://tgss.ncra.tifr.res.in/

Cluster	MWA (″×″,° /mJy beam^{-1})				TGSS (mJy beam^{-1})	
	88 MHz	118 MHz	154 MHz	200 MHz	150 (25″)	150 (60″)
A13	287×263, -74 37.7	202×193, -76 19.3	153×147, -77 12.7	127×128, -83 7.8	5.0	11.4
A548b	282×265, 67 38.2	201×193, 72 16.6	153×148, 62 12.1	128×123, 39 6.0	4.5	9.4
A2063	324×383, 0 77.9	236×204, 4 45.3	183×158, 1 22.2	146×127, 2 19.6	7.1	17.0
A2163	286×272, 0 62.8	206×197, -14 36.6	158×150, -8 20.4	129×122, -10 14.3	3.8	8.9
A2254	347×278, 0 106.9	257×200, 0 65.9	203×157, 0 35.7	161×126, -2 37.6	4.4	10.9
A2345	293×282 46.4	203×198, -51 22.2	155×150, -45 16.7	130×125, -59 7.4	5.0	12.3
A2744	287×263, -56 33.5	204×191, -50 16.9	156×146, -55 12.2	129×122, -41 7.2	4.3	10.2
PLCK G287.0+32.9	278×264, 72 37.9	201×194, 73 19.7	152×147, 37 12.2	125×122, 14 5.6	5.0	10.2
RXC J1314.4-2515	277×264, 70 42.4	202×194, 64 24.0	152×149, 50 15.0	125×122, 61 8.5	5.4	10.2

TABLE 4.1: Image properties for the sample of clusters with known diffuse emission studied here. Note that the TGSS beam is circular at both resolutions.

We also estimated the angular sizes of the haloes and relics at 200 MHz using the task `imfit` in the Common Astronomy Software Analysis (CASA) package (Table 4.4). Also shown in Table 4.4 are the positions and linear extents of the haloes and relics as well as the redshifts of the clusters.

In Fig. 4.1, we show the contours of the GLEAM 200 MHz wideband images overlaid on the respective X-ray images of the clusters. All the X-ray images were obtained from the HEASARC webpage [3] or the XMM database [4]. We used *XMM-Newton* and *Chandra* images where available. Although we make use of the images at other MWA frequencies we are only showing the 200 MHz images as they have the best resolution and sensitivity. Fig. 4.2 shows the GLEAM 200 MHz image contours overlaid on the corresponding greyscale TGSS images at 60" resolution. The exception to this is A13 for which we have used the 25" resolution image. Fig.4.3 shows the spectra of all the halos and relics that were detected.

The results on the individual clusters are discussed below.

4.3.1 Abell 13

A low redshift cluster ($z = 0.0946$, Struble and Rood 1999) with a highly disturbed morphology, the X-ray distribution of Abell 13 (A13) shows two distinct clumps centred around the two brightest cluster galaxies (Juett et al., 2008). The X-ray luminosity of the cluster is $L_{\mathrm{X[0.1-2.4keV]}} = 1.24 \times 10^{44}$ ergs/s (Piffaretti et al., 2011). A13 was observed at radio frequencies by Slee et al. (2001) where they detected an irregularly shaped relic at 1.4 GHz.

The temperature map of the cluster (Juett et al., 2008) shows a drop in the temperature at the site of the radio relic. This seems to suggest that the origin of the relic in A13 is not shock

[3] http://heasarc.gsfc.nasa.gov/xamin/xamin.jsp
[4] http://nxsa.esac.esa.int/nxsa-web

Cluster	Position		S_{200}	α
	RA	DEC	(mJy)	
A13	00:13:33	-19:28:52	101.24	-2.0
A548b	05:45:21	-25:55:55	28.8	-0.74
	05:45:27	-25:55:10	4.5	0
	05:45:11	-25:54:55	22.2	-0.52
	05:45:22	-25:47:30	74.8	-0.13
A2163	16:16:03	-06:09:28	81.65	-1.59
	16:15:40	-06:13:48	373.48	-1.26
	16:15:27	-06:07:02	224.35	-1.41
	16:15:41	-06:09:08	28.46	-0.8
	16:16:23	-06:06:46	237.2	-0.65
A2345	21:27:34	-12:10:58	143.25	-0.8
	21:26:45	-12:07:29	199.22	-0.8
PLCK G287.0+32.9	11:50:43	-28:00:29	20.5	-0.6
	11:50:40	-28:01:00	14.8	-0.38
	11:50:33	-27:58:58	2.86	-0.28
	11:50:34	-28:00:05	6.85	-0.94
	11:50:50	-28:02:22	12.22	-0.6
	11:50:56	-28:01:54	20.59	-0.62
	11:51:00	-28:04:09	51.72	-0.92
	11:50:52	-28:05:24	37.01	-0.56
	11:50:46	-28:05:42	147.07	-0.9
	11:50:59	-28:00:40	34.8	-1.37
	11:50:50	-27:59:10	56.3	-0.6
	11:50:54	-27:59:10	72.2	-0.81
	11:50:59	-27:59:23	21.9	-1.44

TABLE 4.2: List of unrelated sources whose flux densities were subtracted from the corresponding haloes and/or relics. The flux density of the unrelated source at any given frequency is $S_\nu = S_{200} * (\nu_{\rm MHz}/200)^\alpha$. The spectral indices were estimated based on the TGSS and the higher frequency observations. Detailed references for the higher frequency observations are given in Table 4.3.

related as the temperature in regions around shock accelerated relics is usually greater than in the cluster centres.

Fig. 4.1a shows the GLEAM 200 MHz contours of A13 overlaid on the corresponding *XMM-Newton* image. The irregularly shaped object (A) towards the West of the X-ray emission is the radio relic in A13. The other two sources – one to the N and the other to the SE of the X-ray emission – are galaxies with optical counterparts and are unrelated to the relic emission. When compared with the 1.4 GHz image of Slee et al. (2001), the relic is more extended in the GLEAM images. This extension is over and above what can be expected due to convolution effects. The apparently smaller extent of the relic emission at 1.4 GHz is due to the extended emission being resolved out in the VLA-BnA configuration used by Slee et al. (2001).

In Fig. 4.2a we show the GLEAM 200 MHz contours overlaid on the corresponding 25" TGSS greyscale image where a faint source embedded within the MWA contours is seen to the NE of the relic emission. This source is unrelated to the relic and has an optical counterpart. This

source is not detected in the NVSS 1400 MHz image. We estimate the spectral index of this source to be ~ -2 based on the TGSS 150 MHz measurement and the NVSS 1400 MHz upper limit. This spectral index is consistent with the flux density estimate of this source at 74 MHz from the VLSSr images. The extrapolated flux density of this source was subtracted from the integrated flux density of source A to estimate the flux densities of the relic at all the GLEAM survey frequencies used in this study.

The spectrum of the A13 relic is shown in Fig. 4.3a. No diffuse radio emission (halo) associated with the cluster X-ray emission was detected. Slee et al. (2001) produced a spectrum for the relic over the frequency range $80 - 1400$ MHz which showed a curvature that is not seen by our measurements. However, it should be mentioned that the curved spectrum of the A13 relic as seen by Slee et al. (2001) is largely influenced by the Culgoora flux density measurements at 80 MHz. Given the uncertainty in the Culgoora measurements we do not believe that the A13 relic has a curved spectrum. With the currently available more accurate flux density measurements of the relic using MWA we believe the relic spectrum to fit a power law and not the curved spectrum as seen by Slee et al. (2001).

4.3.2 Abell 548b

Abell 548b (A548b) is a dynamically unrelaxed cluster at a redshift of $z = 0.0424$ (den Hartog and Katgert, 1996) but is not extremely X-ray luminous ($L_{\mathrm{X[0.1-2.4keV]}} = 0.1 \times 10^{44}$ ergs/s, Piffaretti et al. 2011).

The cluster is claimed to contain two radio relics: one to the north and the other to the north-west of the cluster centre. The NW relic was first detected by Giovannini et al. (1999) and later confirmed through more detailed observations by Feretti et al. (2006). These two claimed relics are ~ 500 kpc from the cluster centre and near the boundary of the X-ray emission (Solovyeva et al., 2008).

In addition to the above two relics, Feretti et al. (2006) also detected diffuse emission from an irregular source closer to the centre of the cluster. While not entirely certain of its nature, they posit that this source could be the result of an internal shock in the cluster whereas the other two relics are believed to trace the outgoing shocks generated at the time of cluster merger.

Fig. 4.1b shows the GLEAM 200 MHz contours overlaid on the XMM X-ray image of this cluster. There are 4 sources of interest which we have labelled A, B, C and D in the figure. While the source D is a known radio galaxy with an optical counterpart (PGC17721), the nature of the sources A and B, that are claimed to be cluster relics ((Feretti et al., 2012)) is still a mystery. We discuss this in detail in a later section of the paper. The central diffuse source (C), near the northern edge of the X-ray emission, is a complex source. High resolution images of this source (Feretti et al., 2006) reveal that source C is in fact a combination of 3 objects – the outer 2 of which are compact objects even in the ATCA (Australia Telescope Compact Array) 2.5 GHz images. The central object, however, is diffuse in nature and has no optical source associated with it. We estimate the spectral index of this diffuse source between 118 MHz and 1.4 GHz to be -0.7 ± 0.1. Based on its radio morphology ((Feretti et al., 2006)) and spectral index, this

source appears to be a radio galaxy. No diffuse radio emission (halo) associated with the X-ray distribution was detected in this cluster.

In Fig. 4.2b we have overlaid the GLEAM 200 MHz contours on the corresponding 60" TGSS image.

4.3.3 Abell 2063

Abell 2063 (A2063) is a low redshift ($z = 0.0343$, Hill and Oegerle 1993) galaxy cluster with an X-ray luminosity of $L_{\mathrm{X[0.1-2.4keV]}} = 1.14 \times 10^{44}$ ergs/s (Reiprich and Böhringer, 2002).

The GLEAM 200 MHz contours for A2063 are overlaid on the *Chandra* X-ray emission in Fig. 4.1c. In Fig. 4.2c the 200 MHz contours are overlaid on the corresponding TGSS image. The TGSS radio source, which is unresolved at 25" resolution, has an optical counterpart with a redshift corresponding to that of the galaxy cluster and is most likely a galaxy. The radio emission shown in Fig. 4.1c is due to a combination of this head-tail radio galaxy and another radio galaxy co-located with the X-ray emission. The latter source, [OL97]1520+087, has been discussed in Kanov et al. (2006). No diffuse emission in the form of relics or haloes were detected in this cluster. The claimed relic in this cluster (Feretti et al., 2012) is the source 3C318.1 which is 2.4 Mpc from the cluster centre and is a relic radio galaxy. This source is discussed in detail by Komissarov and Gubanov (1994) and is not relevant to the present discussion.

4.3.4 Abell 2163

Abell 2163 (A2163) ($z = 0.203$, Struble and Rood 1999) is one of the hottest and most X-ray luminous clusters known ($L_{\mathrm{X[0.1-2.4keV]}} = 20.16 \times 10^{44}$ ergs/s, Piffaretti et al. 2011). The X-ray distribution of the cluster shows two primary subclusters – one to the west and a secondary one to the north (Bourdin et al., 2011). The primary subcluster of A2163 (west) shows a bullet-like nature suggesting a recent merger in the E-W direction. The north subcluster appears to have not had any recent interaction with the west subcluster and is well separated from it.

This cluster contains a giant radio halo ($l \sim 3$ Mpc) in the middle and a small radio relic north-east of the cluster centre (Feretti et al., 2001).

Figs. 4.1d and 4.2d show the GLEAM 200 MHz contours of this cluster overlaid on the corresponding *XMM-Newton* X-ray image and the TGSS image, respectively. The central radio halo (A) and the relic (B) are detected in all the GLEAM images (see Table 4.3 for their flux densities). These flux densities were estimated after subtracting the flux densities of unrelated sources (Fig. 4.2d). The flux densities of these unrelated sources estimated at 150 MHz (TGSS images) and at 1400 MHz ((Feretti et al., 2001)) were used to estimate their spectra and their flux densities at all the GLEAM survey frequencies given in Table 4.3.

4.3.5 Abell 2254

The galaxy cluster Abell 2254 (A2254) is a rich, X-ray luminous cluster ($L_{\mathrm{X[0.1-2.4keV]}} = 4.79 \times 10^{44}$rg ergs/s, Böhringer et al. 2000) located at a redshift of $z = 0.178$ (Crawford et al., 1995).

Optical and X-ray analysis of the cluster (Girardi et al., 2011) suggest that A2254 is a highly disturbed cluster with a very complex morphology. There are two major clumps of galaxies separated by $\sim 0.5h_{70}^{-1}$ Mpc in the east-west direction. While the primary X-ray peak coincides with the BCG (Brightest Cluster Galaxy), the secondary X-ray peak in the east clump does not, suggesting that the cluster is still in the middle of an ongoing merger.

Radio observations of A2254 (Govoni et al., 2001a) show an irregularly shaped radio halo with clumpy features. Fig. 4.1e shows the GLEAM 200 MHz contours overlaid on the corresponding XMM X-ray image. The halo is seen at all the available GLEAM images.

We show the same 200 MHz contours overlaid on the corresponding 60" TGSS image in Fig. 4.2e. Note that the RMS value in the 200 MHz image of A2254 is ~ 37 mJy beam^{-1} which is ~ 5 times larger when compared with the RMS values in the other 200 MHz images. This is because of the position of this cluster. At a declination of $\sim +20$d, A2254 is at the northern-most declination setting for MWA which results in a larger synthesized beam and RMS.

4.3.6 Abell 2345

Abell 2345 (A2345) is a highly disturbed, X-ray luminous ($L_{\mathrm{X[0.1-2.4keV]}} = 3.9 \times 10^{44}$ ergs/s, Böhringer et al. 2004) galaxy cluster. The redshift of the cluster is found to be $z = 0.1789$ (Boschin et al., 2010).

Boschin et al. (2010) also highlighted the complex substructure in the cluster. A2345 contains three distinct subclumps as seen in optical and X-ray. These clumps lie in the east, south-east and north-west directions.

Extended diffuse emission from A2345 was first seen by Giovannini et al. (1999) as part of the NRAO VLA Sky Survey (NVSS) and later confirmed through detailed observations at 325 MHz and 1.4 GHz by Bonafede et al. (2009). The cluster contains two relics (A & B) on opposite sides of the cluster centre, both ~ 1 Mpc from the cluster centre. Each relic is about 1 Mpc in size.

In Fig. 4.1f, we show the GLEAM 200 MHz contours overlaid on the corresponding XMM X-ray image. The two relics are seen to the east (A) and to the west (B) of the central X-ray emission. The source above the east relic (C), which has a counterpart in the 60" TGSS image (Fig. 4.2f), is an unresolved source, has an infra-red counterpart in the 2 Micron All Sky Survey images and is unrelated to the relic emission. The source D is a cD galaxy while the source E is another radio galaxy in the cluster (Bonafede et al., 2009). The image obtained after subtracting sources D and E does not detect any radio halo that is associated with the cluster. Table 4.3 contains the flux densities for the relics at all the GLEAM frequencies except 88 MHz where they get blended with other sources.

Cluster	Object	Integrated Flux Densities (mJy)									$L_{X[0.1\text{-}2.4\ keV]}$	$\log(P_{1.4})$
		88 MHz	118 MHz	150 MHz	154 MHz	200 MHz	325 MHz	610 MHz	1400 MHz	3000 MHz	($\times 10^{44}$) erg s^{-1}	W Hz^{-1}
A13	H	–	–	–	–	–	–	–	–	–	1.24	$\lesssim$21.79
	R	4445.5 ± 355.6	2817.4 ± 225.4	1868.1 ± 186.8	1861.9 ± 149	1290 ± 103	–	–	35.5 ± 1.7[1]	–	–	24.08
A548b	H	–	–	–	–	–	–	–	–	–	0.1	$\lesssim$21.00
	B	196.05 ± 15.68	114.51 ± 9.16	142.12 ± 14.21	168.26 ± 13.46	116.21 ± 9.3	–	–	60 ± 5[2]	–	–	23.51
	A	307.2 ± 24.6	298.4 ± 23.9	203.9 ± 20.4	256 ± 20.5	230.1 ± 18.4	–	–	61 ± 5[2]	–	–	23.51
A2063	H	–	–	–	–	–	–	–	–	–	1.14	$\lesssim$21.23
A2163	H	2828.3 ± 226.3	1178 ± 94.2	563 ± 56.3	1235.4 ± 98.8	791.1 ± 63.3	861 ± 86.1[3]	–	155 ± 2[4]	–	20.16	25.61
	R	444.4 ± 35.6	172.9 ± 13.8	89.9 ± 9	252.4 ± 20.2	132.4 ± 10.6	82 ± 8.2[3]	–	18.7 ± 0.3[4]	–	–	24.68
A2254	H	1899.8 ± 247	904.9 ± 117.6	1086.9 ± 141.3	607.8 ± 79	289.4 ± 37.6	–	–	33.7 ± 3.37[5]	–	4.79	24.79
A2345	H	–	–	–	–	–	–	–	–	–	3.9	$\lesssim$22.38
	R(E)	–	623.9 ± 49.9	555.6 ± 55.6	592.3 ± 47.4	419.8 ± 33.6	188 ± 3[6]	–	29 ± 0.4[6]	–	–	24.73
	R(W)	–	1164.2 ± 93.1	1025.1 ± 102.5	932.3 ± 74.6	747.4 ± 59.8	291 ± 4[6]	–	30 ± 0.5[6]	–	–	24.74
A2744	H	–	759.3 ± 60.7	414.9 ± 41.5	512.2 ± 41	372.5 ± 30	218 ± 21.8	–	57.1 ± 0.57[5]	–	11.82	25.73
	R	–	285.3 ± 22.8	202.9 ± 20.3	203.6 ± 16.3	129.2 ± 10.3	98 ± 10	–	18.2 ± 0.18[5]	–	–	25.24
PLCK G287.0+32.9	H	–	–	314 ± 31.4	–	–	63 ± 6[7]	26 ± 2.6[7]	–	2.9 ± 0.3[7]	17.2	25.52
	R(SE)	621.4 ± 49.7	438.3 ± 35.1	382 ± 38.2	280.7 ± 22.5	268 ± 20.2	114 ± 11.4[7]	50 ± 5[7]	25 ± 5[7]	5.2 ± 0.52[7]	–	25.72
	R(NW)	855.3 ± 224.3	683.9 ± 168.1	620 ± 62	433.2 ± 93.4	356.8 ± 68.7	216 ± 21.6[7]	110 ± 11[7]	15.2 ± 1.52[7]	–	–	25.51
RXC J1314.5-2515	H	–	–	–	–	–	40 ± 3[8]	10.3 ± 0.3[9]	–	–	9.89	24.18
	R(E)	–	96.6 ± 7.7	104.8 ± 10.5	38.1 ± 7.7	86 ± 6.9	52 ± 4[8]	28 ± 1.4[9]	11.1 ± 0.3[10]	–	–	24.71
	R(W)	–	425.3 ± 34	519.8 ± 52	267.7 ± 21.4	263.1 ± 21.1	137 ± 11[8]	64.8 ± 3.2[9]	20.2 ± 0.5[10]	–		24.97

TABLE 4.3: Integrated flux densities of the haloes (H) and relics (R) from the current study. All the 150 MHz values are from the TGSS images. The references for the other flux densities are as follows: [1]Slee et al. (2001) [2]Feretti et al. (2006) [3]Feretti et al. (2004) [4]Feretti et al. (2001) [5]Govoni et al. (2001a) [6]Bonafede et al. (2009) [7]Bonafede et al. (2014) [8]Venturi et al. (2013) [9]Venturi et al. (2007) [10]Feretti et al. (2005). The X-ray luminosities were obtained from the MCXC meta-catalogue by Piffaretti et al. (2011). The only exception to this is PLCK G287.0+32.9 for which the X-ray luminosity was obtained from Planck Collaboration et al. (2011).

4.3.7 Abell 2744

The cluster Abell 2744 (A2744) is located at a redshift of $z = 0.308$ (Struble and Rood, 1999) and is extremely luminous in X-ray ($L_{\mathrm{X}[0.1-2.4\mathrm{keV}]} = 11.82 \times 10^{44}$ ergs/s, Ebeling et al. (2010)).

Optical and X-ray analysis of this cluster (Kempner and David, 2004, Boschin et al., 2006, Owers et al., 2011) shows that it is currently undergoing a merger in the north-south direction.

A giant radio halo ($\sim$ 2.4 Mpc) was first seen in the cluster by Govoni et al. (2001a,c). In addition to the halo, this cluster also contains an elongated radio relic north-east of the cluster centre.

The radio halo and the relic were detected in the GLEAM survey at all the observed frequencies (Table 4.3). The flux densities of the halo and relic at 88 MHz are not given as they get blended with each other at that frequency. Fig. 4.1g shows the GLEAM 200 MHz contours overlaid on the XMM X-ray image. The contours of the radio halo (A) are aligned with the X-ray emission. The radio relic (B) is the source NE of the X-ray and halo emission. The source SE of the X-ray distribution has an optical counterpart and is unrelated to the halo and relic emission. The GLEAM 200 MHz contours are overlaid on the corresponding 60" TGSS image in Fig. 4.2g.

4.3.8 PLCK G287.0+32.9

PLCK G287.0+32.9 is a high redshift ($z = 0.39$), highly X-ray luminous ($L_{\mathrm{X}[0.1-2.4\mathrm{keV}]} = 17.2 \times 10^{44}$ ergs/s, Planck Collaboration et al. 2011) galaxy cluster which contains radio relics (Bagchi et al., 2011) on opposite sides of the cluster centre to the north and south.

Subsequent observations of the cluster (Bonafede et al., 2014) revealed that the source identified by Bagchi et al. (2011) as the north relic was in fact the lobe emission from a galaxy. The true north relic was located south-west of this emission. The projected separation between the relics was estimated to be $\sim$ 3.2 Mpc which is one of the largest known separations between double relics. The cluster also contains a radio halo near the cluster centre (Bonafede et al., 2014).

In Fig. 4.1h we show the GLEAM 200 MHz contours overlaid on the corresponding *XMM-Newton* image. The south-east relic (SE), the north-west relic (NW) and the halo (H) are marked in the figure. Also shown are the galaxy (G) and the region further to the north-west (F) which get blended with the north-west relic and halo at frequencies below 200 MHz. GMRT observations of the cluster by Bonafede et al. (2014) at 150 (50"), 325 (13") and 610 MHz (7") show the presence of 10 unresolved sources near the halo and north-west relic region. In order to estimate the flux density of the north-west relic we first had to subtract the flux densities of all these unrelated sources. The flux densities of these unrelated sources at GMRT frequencies are available in Bonafede et al. (2014) and the extrapolated flux densities at MWA frequencies were subtracted from the total flux density in this region. Subtracting all the unrelated sources still leaves the halo and the north-west relic blended. We extrapolated the halo flux density to the MWA frequencies using the flux density values given in Bonafede et al. (2014) (Table 4.3) and subtracted it from the remaining flux density. This is quoted as the flux density of the north-west relic in Table 4.3.

Fig. 4.2h shows the GLEAM 200 MHz contours overlaid on the corresponding 60" TGSS 150 MHz image. Note that the TGSS image also detects the radio halo.

In Fig. 4.3k and 4.3l we plot the spectra for the north-west and the south-east relic, respectively.

4.3.9 RXC J1314.4-2515

A highly X-ray luminous cluster ($L_{\mathrm{X[0.1-2.4keV]}} = 9.89 \times 10^{44}$ ergs/s, Piffaretti et al. 2011), RXC J1314.4-2515 is at a redshift of $z = 0.247$ (Valtchanov et al., 2002). The X-ray emission is distorted in the NW-SE direction and is not centred on the two BCGs in the cluster (Valtchanov et al., 2002).

Radio observations of the cluster (Venturi et al., 2007, Feretti et al., 2005) reveal the presence of two radio relics – one to the east and another to the west of the cluster and a radio halo in the middle with a bridge to the west relic.

Fig. 4.1i shows the GLEAM 200 MHz contours of the cluster overlaid on the corresponding XMM X-ray image. The contours of the east relic (A) are seen towards the edge of the X-ray emission. The source seen to the west of the X-ray emission (B) is a convolution of the west relic and the radio halo in the cluster. Even at 200 MHz it is not possible to separate the halo emission from that of the west relic. Estimating the flux density of the east relic was straightforward. In order to estimate the flux density of the west relic we first extrapolated the flux density of the halo at 610 MHz (Venturi et al., 2007) to the MWA frequencies (up to 118 MHz) by assuming a spectral index of -1.34. This spectral index of -1.34 is the average spectral index of haloes from literature (Feretti et al., 2012). This extrapolated halo flux density was subtracted from the total flux density of the region B in order to get the flux density of the west relic. At 88 MHz, however, the east relic gets blended with the west relic and the halo and hence their flux densities are not estimated at 88MHz (Table 4.3).

In Fig. 4.2i we show the contours of the GLEAM 200 MHz image overlaid on the corresponding 60" TGSS image.

4.4 Discussion

Combining the GLEAM and TGSS flux density measurements along with all available measurements in literature (see Table 4.3) we estimated the spectral indices of the detected haloes and relics in the range 80 – 1400 MHz. In the case of PLCK G287.0+32.9, however, the spectrum is estimated over the range 80 – 3000 MHz. In Fig. 4.3 we have shown the spectra of the radio haloes and relics in the 9 clusters we observed. The spectra follow a power law over the frequency range $80 - 1400(/3000))$ MHz with no breaks. The mean values are $\alpha = -1.13 \pm 0.21$ for haloes and $\alpha = -1.2 \pm 0.19$ for relics. These mean values are in agreement, within errors, with the mean values of spectral indices in literature for haloes ($\alpha = -1.34 \pm 0.28$) and relics ($\alpha = -1.42 \pm 0.37$) (Feretti et al., 2012). Most of the spectral index estimates of haloes and relics in literature are

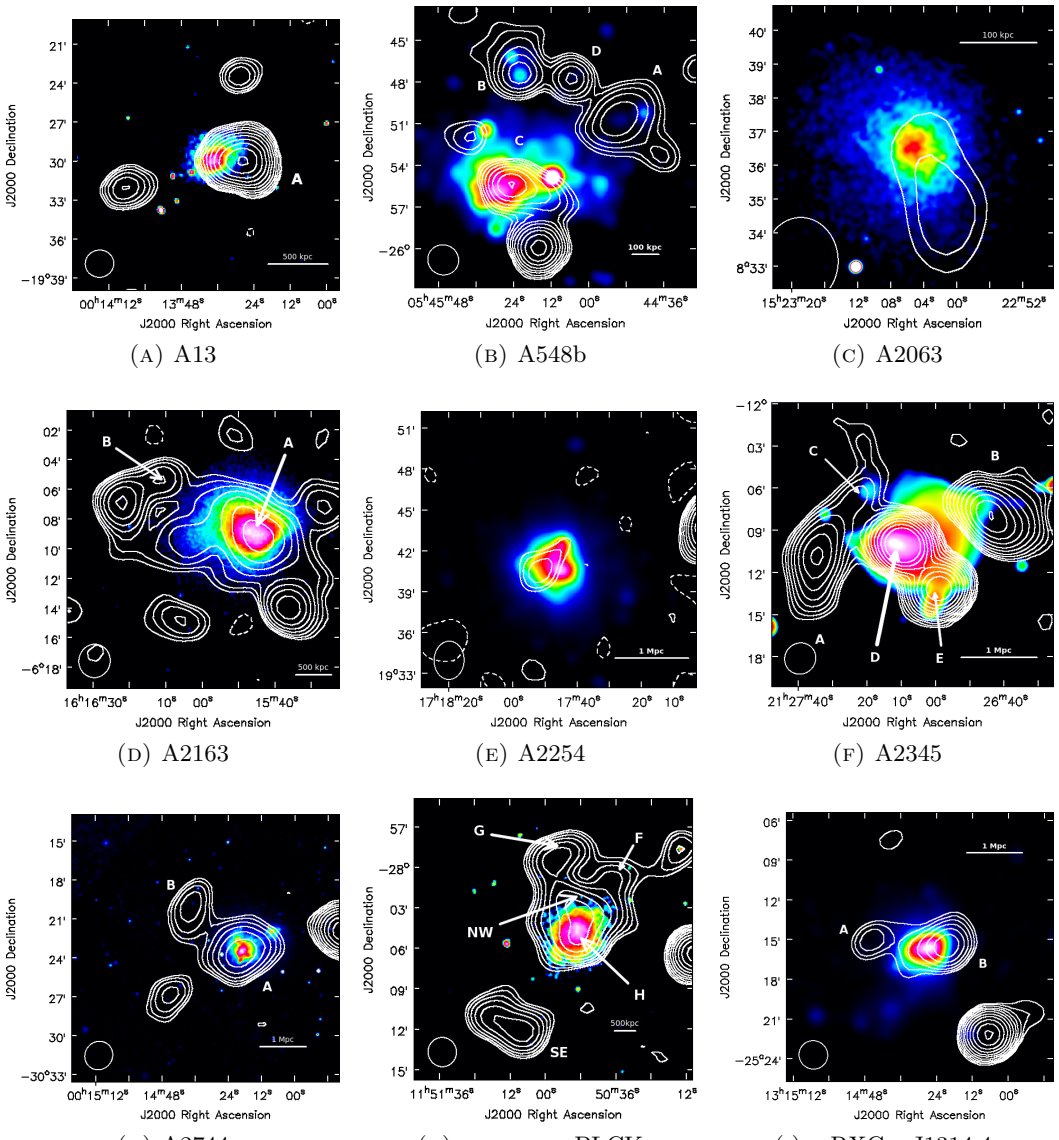

(A) A13 (B) A548b (C) A2063

(D) A2163 (E) A2254 (F) A2345

(G) A2744 (H) PLCK G287.0+32.9 (I) RXC J1314.4-2515

FIGURE 4.1: GLEAM 200 MHz contours (60 MHz bandwidth) overlaid on the respective X-ray images of the clusters. The contours start at 3σ (at 2σ for A2254) and increase by $\sqrt{2}$ thereafter. See Table 4.1 for σ values. The first negative contour at 3σ (at 2σ for A2254) is also plotted (dashed lines). The full-width half maximum of the synthesized beam of the MWA is indicated in the bottom left-hand corner.

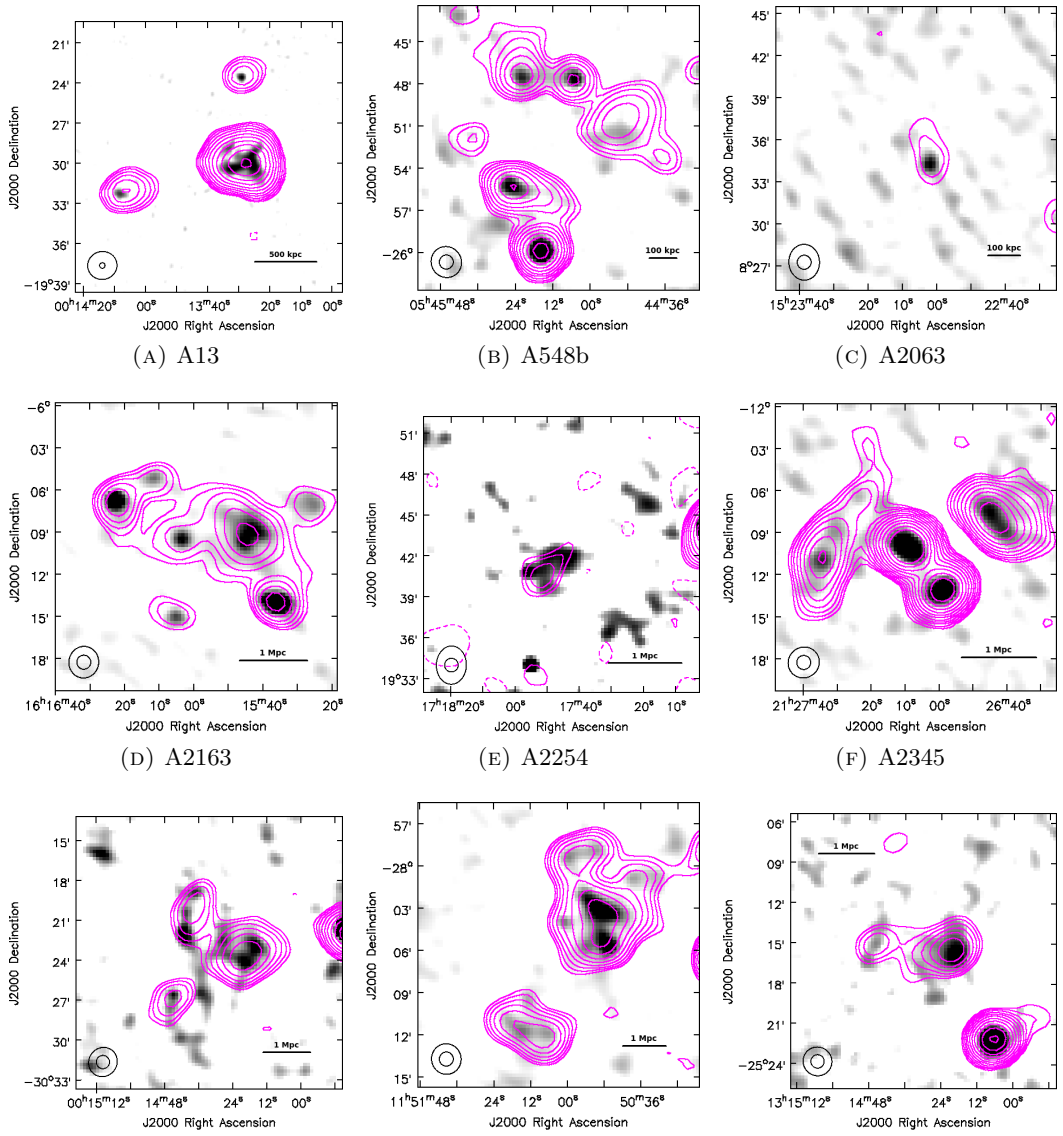

(A) A13 (B) A548b (C) A2063

(D) A2163 (E) A2254 (F) A2345

(G) A2744 (H) PLCK G287.0+32.9 (I) RXC J1314.4-2515

FIGURE 4.2: GLEAM 200 MHz (60 MHz bandwidth) contours overlaid on the corresponding greyscale TGSS 150 MHz images. All the TGSS images are at 60" resolution except for A13 which is at 25" resolution. Contours start at 3σ (at 2σ for A2254) and increase by $\sqrt{2}$ thereafter. The first negative contour at 3σ (at 2σ for A2254) is also plotted (dashed lines). The full-width half maxima of the synthesized beams of the GLEAM and TGSS images are indicated in the bottom left-hand corner.

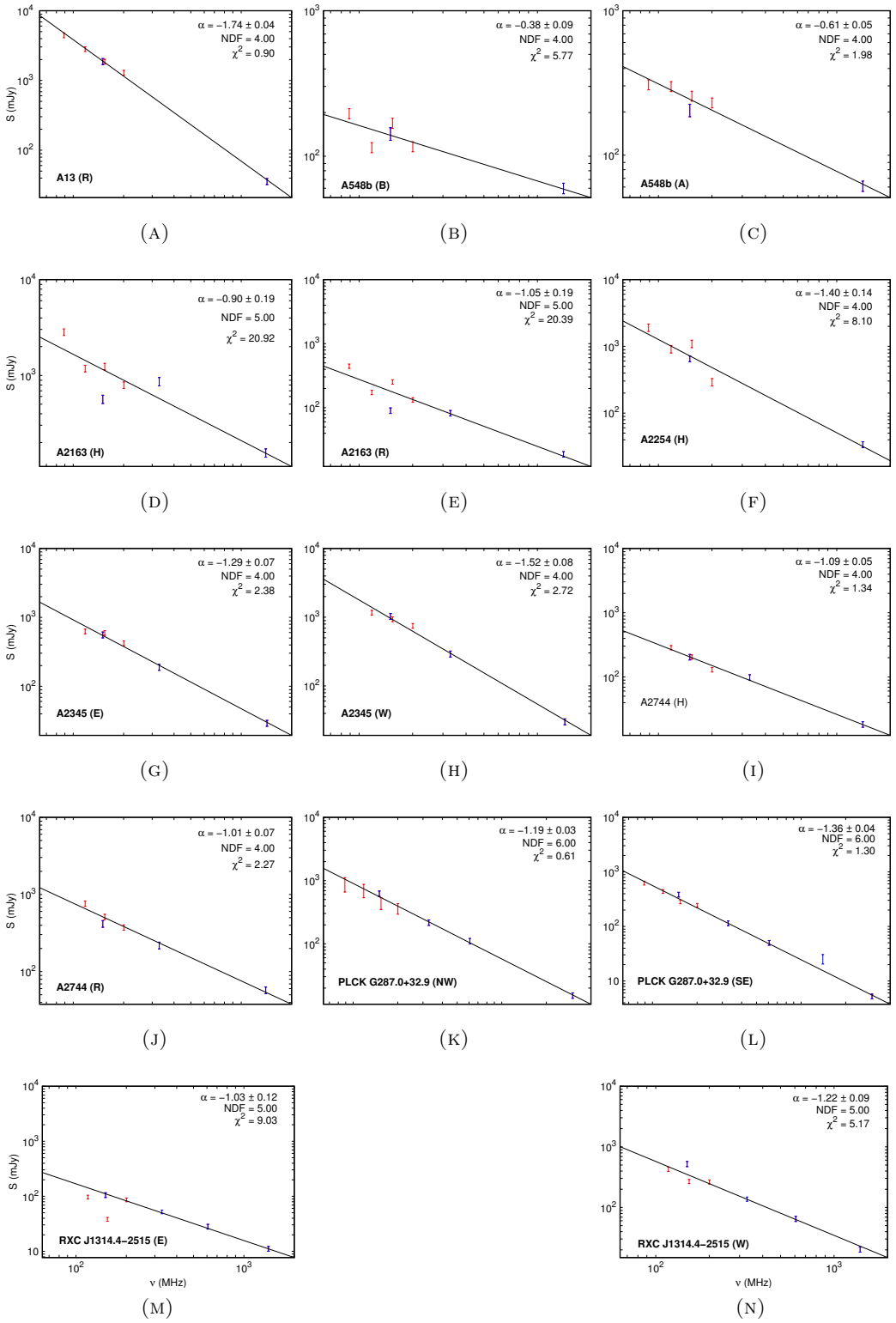

FIGURE 4.3: Spectra of haloes and relics. Data points in red colour are from the GLEAM survey measurements while those in blue colour are measurements from other telescopes. Note that the range of frequencies along the x-axis is identical in all the panels and is specified in the bottom-most panel. Every panel also shows the spectral index value (α), the number of degrees of freedom (NDF) and the reduced χ^2 value of the fit.

Cluster	Object	z	α	δ	Angular Size ($''\times''$,$^\circ$)			Linear Size	
					θ_{maj}	θ_{min}	pa	kpc	kpc
A13	R	0.094	00:13:28	–19:29:58	150	108	36	260	180
A548b	B	0.042	05:45:22	–25:47:07	84	72	45	110	89
	A		05:44:50	–25:50:37	168	102	96	180	130
A2063	R	0.035							
A2163	H	0.203	16:15:45	–06:09:07	234	132	51	970	390
	R		16:16:10	–06:05:02	193	102	92	660	350
A2254	H	0.178	17:17:52	+19:40:37	147	109	0	450	340
A2345	R(E)	0.179	21:27:34	–12:10:41	276	78	157	710	270
	R(W)		21:26:43	–12:07:56	174	60	41	590	180
A2744	H	0.308	00:14:20	–30:23:29	192	132	63	1010	690
	R		00:14:37	–30:20:22	204	102	132	1100	400
PLCK G287.0+32.9	H	0.39	11:50:49	–28:04:36	210	150	117	900	750
	R(SE)		11:51:12	–28:11:41	252	96	77	1530	670
	R(NW)		11:50:49	–28:03:35	192	132	38	860	410
RXC J1314.5-2515	H	0.244							
	R(E)		13:14:44	-25:15:03	192	120	143	660	600
	R(W)								

TABLE 4.4: Halos and relics detected by MWA. Columns 4 and 5 correspond to the peaks of emission at 200 MHz of the corresponding haloes and relics. No helo or relic was detected in A2063. The radio halo and the west relic in RXC J1314.5-2515 are blended even in the 200 MHz GLEAM image.

Cluster	RMS (mJy beam^{-1})	Resolution ($''$)	Linear Extent (kpc)
A13	9.2	133	240
A548b	7.8	132	120
A2063	19.2	121	88
A2345	9.2	136	420

TABLE 4.5: Upper limit clusters. The linear extents corresponding to the resolutions are given.

in the range $325-1400$ MHz, while in the current study the estimates are in the range $80-1400$ MHz or $80-3000$ MHz.

There are two exceptions to this result in our sample of clusters. The first is A548b whose relics have flat spectral indices (-0.61 (A) and -0.38 (B)) and the other is A13 where the relic has a steeper spectral index of -1.74.

The steep spectrum of the A13 relic can be attributed to the fact that it is not a typical shock accelerated relic. X-ray analysis using *Chandra* (Juett et al., 2008) shows that while the cluster is undergoing a merger event there are no shocks near the position of the radio relic. Moreover, the 1.4 GHz image of A13 shows this relic radio emission trailing from the brightest cluster galaxy located at the peak of the X-ray emission. The above authors suggest that this galaxy could have hosted an AGN in the past and the relic is a remnant of that emission. They propose two scenarios to explain this: either the radio plasma rose buoyantly to its current position, or the galaxy moved away during the merger event leaving behind the radio plasma that is now seen

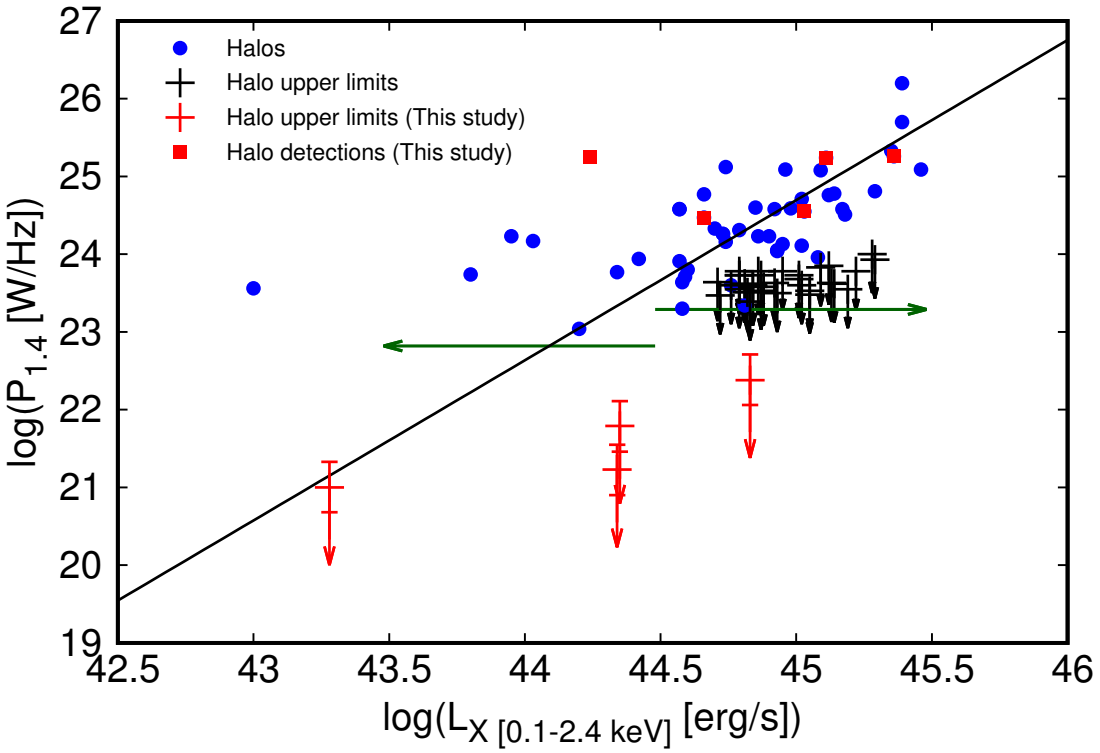

FIGURE 4.4: Plot showing the relation between the $L_{\mathrm{X}[0.1-2.4\mathrm{keV}]}$ of a cluster and the radio power at 1.4 GHz ($P_{1.4}$) of the halo in the cluster. The filled blue circles represent all the known radio haloes (Feretti et al., 2012). The solid black line is the best fit to the $L_{\mathrm{X}} - P_{1.4}$ relation for radio haloes (Brunetti et al., 2009). The black arrows represent the upper limits to halo emission (Venturi et al., 2008, Kale et al., 2013, Venturi et al., 2007). The MWA halo detections are shown as red squares while the upper limits are shown as red arrows. Note that the MWA upper limits were estimated using the RMS values estimated in the respective images at 200 MHz and then extrapolating to 1.4 GHz with a spectral index of −1.34. The four MWA upper limits, from left to right, are – A548b, A2063, A13 and A2345. The five MWA halo detections, from left to right, are – PLCK G287.0+32.9, A2254, RXC J1314.4-2515, A2744 and A2163. The green arrows show the upper limits to the radio powers in the *off-state* radio haloes based on their X-ray luminosities as given by Brown et al. (2011).

as a relic. In either scenario, there is no influx of new high energy electrons to this relic as the AGN is not active any more. As a result, the radio spectrum of this relic emission is steeper than the mean spectra of cluster relics which are produced by cluster merger shocks. This source is a relic radio galaxy rather than a cluster relic.

In the case of A548b, it is debatable if the sources A and B are truly radio relics driven by merger shocks of the cluster or merely the lobes of radio emission produced by one or more of the cluster galaxies detected in the vicinity of these sources, including the source D (Fig. 1).

It is possible to consider the sources A and B as relics in the cluster produced by merger shocks. There is some evidence supporting this scenario because the temperature distribution of the cluster shows a jump near the positions of the sources A and B (Solovyeva et al., 2008). However, as has been discussed in this paper, the relics are toward the outskirts of the cluster and are located in a region of poor signal to noise ratio in the X-ray images. So, the evidence for

the temperature jump near the relics is rather marginal. Furthermore, the radio morphologies of the relics observed in the higher frequency images (Feretti et al. (2006)) do not show any sharp boundaries usually observed in other cluster relics, but, are rather diffuse and irregular, resembling more like the radio emission or, the relict radio emission produced by radio galaxies and / or quasars.

It apears more likely that the sources A and B are lobes created by one or more of the cluster galaxies. In the case of source B, there is a small angular diameter ($4'' \times 2''$) cluster radio source (ESO 488-G006) with a flat spectral index embedded in this diffuse emission (Feretti et al. (2006)). In the case of source A, there are two cluster galaxies (source D and the extension seen toward south-west of source A in Fig. 1) within $\sim$ 100 kpc of this diffuse radio emission either of which could be responsible for this diffuse radio emission.

It appears that the sources A and B are more likely to be lobes of radio galaxies rather than cluster relics.

Fig. 4.4 shows the empirical relation ($L_{\rm X} - P_{1.4}$) between the radio power of the halo at 1.4 GHz ($P_{1.4}$) and the total X-ray luminosity of the cluster ($L_{\rm X}$) in the range 0.1–2.4 keV. Based on the GMRT Radio Halo Survey, Brunetti et al. (2009, 2007) estimated upper limits to the halo emission in clusters where none were detected. The upper limits plotted in Fig. 4.4 (black crosses) (Venturi et al., 2008, Kale et al., 2013, Venturi et al., 2007) correspond to clusters in the redshift range $z = 0.2 - 0.4$ and to an assumed halo size of 1 Mpc. These upper limits appear to correspond to *off-state* clusters compared to the detections which are in an *on-state*. It has been known that, for the most part, *on-state* clusters are the more disturbed clusters while the *off-state* clusters are relaxed. However, if the *hadronic* model is to be believed, there should be some amount of relativistic electrons in the ICM in either case.

Five of the nine clusters studied in this paper contain radio haloes which were detected by MWA. These clusters are shown in Fig. 4.4 with red squares. No radio haloes were detected in the remaining four clusters – A13, A548b, A2063 and A2345. Based on the RMS values in the respective images at 200 MHz, we have been able to put upper limits on the radio powers of any possible radio haloes that might be present in these clusters. These RMS values were estimated after removing the already known non halo sources in the GLEAM 200 MHz images using BANE (see Section 2.1) and then estimating the RMS values from the central regions of the clusters in the residual images. The RMS values thus estimated correspond to radio powers of haloes whose linear extents are comparable to those of the spatial resolutions in these images. The linear sizes corresponding to the spatial resolutions in these four images are given in column 4 of Table 4.5. The upper limits shown in Fig. 4.4 (red crosses) correspond to radio powers of such haloes. However, note that these upper limits at 1.4 GHz were obtained after extrapolating the respective values at 200 MHz with a spectral index of -1.34 which is the mean value of the spectral indices of haloes (Feretti et al., 2012). If the haloes in the current sample have spectra which are steeper than the mean value then the limits would be lower than those estimated here. The upper limit to the radio power of halo emission from A548b is consistent with that expected from the empirical $L_{\rm X} - P_{1.4}$ relation (best-fit line shown in Fig. 4.4). Note that this best-fit line (Brunetti et al., 2009) corresponds to Giant Radio Haloes with linear extent, $l \gtrsim 1$ Mpc. We discuss the upper limits on the remaining three clusters below.

The upper limits on the radio powers of haloes at 1.4 GHz in A13, A2063 and A2345 (shown in Fig. 4.4) are factors of $\sim$ 30, 120 and 90 below that expected from the $L_{\rm X} - P_{1.4}$ relation respectively. If the extents of the radio haloes in these clusters are $\sim$ Mpc (canonical halo size) the upper limit obtained for A2063 is consistent with the $L_{\rm X} - P_{1.4}$ relation. However the upper limits obtained for A13 and A2345 are lower than the expected values by a factor of $\sim$ 2 and 20 respectively.

Estimates of the upper limits on the radio powers of haloes in galaxy clusters have been carried out before. Brown et al. (2011) used the radio continuum images of galaxy clusters from the Sydney University Molonglo Sky Survey (SUMSS, Bock et al. 1999) in order to estimate such constraints. By stacking 105 clusters based on their X-ray luminosities, they found that for high X-ray luminosity ($L_{\rm X} > 3 \times 10^{44}$ ergs/s) clusters, the upper limit on the average radio power is $(1.95 \pm 0.75) \times 10^{23}$ W Hz^{-1}, whereas for the low luminosity ($L_{\rm X} < 3 \times 10^{44}$ ergs/s) clusters, the upper limit on the average radio power is $(0.66 \pm 0.89) \times 10^{23}$ W Hz^{-1}. The green arrows in Fig. 4.4 show the upper limits for both low and high X-ray luminosity clusters. The individual upper limits obtained in this study with the MWA observations are comparable to, or, better than the average limits obtained by Brown et al. (2011).

It is instructive to discuss the upper limits on the radio powers of haloes in many clusters in the context of the hadronic, or, secondary model. In order to estimate the contribution of the secondary model to radio emission from haloes, it is necessary to first estimate the contribution of high energy cosmic ray (CR) protons to the energy content of the cluster. Brunetti et al. (2008) show (Fig. 3 in their paper) how the ratio of the relativistic protons to the thermal protons ($\epsilon_{\rm p}/\epsilon_{\rm th}$) varies as a function of the magnetic field (B) in the cluster. This relation depends on the spectral index (δ) of the proton distribution ($N(p) \propto p^{-\delta}$, where p is the particle momentum) as well as the temperature (T) and the number density of thermal protons ($n_{\rm th}$) in the cluster. Assuming $n_{\rm th}$ in the system to be $\sim$ 1500 m^{-3} and the proton spectral index $\delta = 2.5$, Fig. 3 in Brunetti et al. (2008) shows how the energy density of cosmic-ray protons varies as a function of its magnetic field. Increasing the magnetic field from 0.5μG to 5μG (Bonafede et al., 2010) decreases the energy content of the cluster due to the CR proton component from 10% to 0.25%. Furthermore, Brunetti and Blasi (2005) show that for a given magnetic field, the efficiency of electron acceleration decreases with increasing values of both $n_{\rm th}$ as well as $\epsilon_{\rm p}/\epsilon_{\rm th}$, due to the increased damping of Alfvén waves on the protons.

Recent analysis of the Coma cluster (Brunetti and Lazarian, 2011) suggests that the strength of synchrotron emission due to the hadronic model is a factor of 10 smaller as compared to the primary model. The upper limits on the radio powers of haloes in A13 and A2345 are $\sim$ 10 times below the expected value. However, the upper limit on the radio power of a halo in A2063 is more than 50 times smaller than that expected. It should be noted, however, that the number of unknowns in these systems is still quite large. While the electron density ($n_{\rm e}$), and hence the proton density ($n_{\rm p}$) in the clusters are known, the magnetic field, B, and the CR proton energy content, $\epsilon_{\rm p}/\epsilon_{\rm th}$, are still unknown. The cluster A2063, being a relaxed cluster could well host a weak magnetic field (< 1 μG) resulting in a much weaker emission from the hadronic model. Independent measurements of magnetic fields in these clusters is crucial to the verification of the hadronic models.

4.5 Summary

In this chapter, we have presented low frequency observations of 9 merging galaxy clusters using the Murchison Widefield Array. Theses observations were carried out at 5 frequencies (88, 118, 154, 188 and 215 MHz) as part of the GaLactic and Extragalactic All-sky MWA (GLEAM) Survey. The images were products of a standard pipeline developed to analyse all of the GLEAM survey data. Furthermore, better resolution ($\sim 60''$) TGSS 150 MHz images were used to compare with the corresponding MWA images in order to identify and subtract unrelated sources that are blended with the halo and relic emission.

We have detected radio relics in 7 of the 9 clusters and also estimated their spectra over the frequency range $80 - 1400$ MHz (or, in the case of PLCK G287.0+32.9, $80 - 3000$ MHz). These spectra were found to be fit by a power law over this range. The cluster A548b was found to contain radio sources (which were claimed to be relics) with the flattest spectral indices in the current sample (-0.38 and -0.61). Based on the current study we believe these sources to be radio lobes rather than relics produced in merger shocks. The relic in A13 was found to have the steepest spectrum in the current sample ($\alpha = -1.74$). However, the origin of this relic is not due to merger driven shocks but rather it is the remnant emission from an old radio galaxy.

In 5 of the 9 clusters we detected the radio haloes that were first seen in high frequency (~ 1.4 GHz) observations. Their spectra fit a power law with no breaks in the range $80 - 1400$ MHz. In the remaining 4 clusters where no radio haloes were detected, we have placed upper limits to their radio powers. These upper limits are a factor of $2 - 20$ below that expected from an empirical relation between the X-ray luminosities of clusters and the radio powers of haloes in the corresponding clusters. Lack of independent measurements of magnetic fields in these clusters precludes one from putting serious constraints on the hadronic model at this stage.

CHAPTER

FIVE

ABELL 168: DISCOVERY OF RADIO RELIC USING MWA

5.1 Motivation

As mentioned earlier, low frequency observations of galaxy clusters are better suited for the observation of diffuse, extended radio emission in galaxy clusters seen in the form of radio halos and relics, especially at lower redshifts ($z < 0.1$). This is because at these redshifts the angular size of ∼Mpc sized objects will be $\gtrsim 10'$ which can get resolved out at higher frequency (~ 1 GHz) interferometric measurements. Furthermore, the X-ray luminosity function for galaxy clusters (Böhringer et al., 2002) suggests that there are a lot more low luminosity clusters than high luminosity ones. Therefore, if the $L_X - P_{1.4}$ relation for halos is to be believed the halos in these clusters will have correspondingly lower radio power which might have been missed by the current generation of telescopes. Additionally, these halos and relics could have steep spectra ($\alpha < -1.5$) as predicted by the turbulence model in which case they would also be likely to have missed detection at higher frequencies.

5.2 Sample Selection

With this motivation in mind we decided to search for clusters at low redshifts where extended emission could have been missed in earlier surveys like NVSS, WSRT, ATCA and GMRT. We first used the MCXC (Meta-Catalogue of X-ray detected Clusters of galaxies) catalog to compile a list of cluster with redshift $z < 0.1$. The MCXC is a very large X-ray cluster catalog based on publicly available ROSAT All Sky Survey-based (NORAS, REFLEX, BCS, SGP, NEP, MACS, and CIZA) and serendipitous (160SD, 400SD, SHARC, WARPS, and EMSS) cluster catalogues (Piffaretti et al., 2011). No additional cutoff was used for compiling a list of target clusters.

This criterion resulted in a final list of 440 clusters derived from the MCXC catalog. These clusters were then studied in the radio regime using the 200 MHz wideband GLEAM survey

Cluster Name	RA(J2000) (hh:mm:ss)	DEC(J2000) (dd:mm:ss)	z	$L_x(0.1-2.4keV)$ 10^{44} erg/s	M_{500} 10^{14} $M_\odot$	$Y_{x,M_{500}}$ 10^{14} $M_\odot$
A168	01:15:9.8	00:14:51	0.045	0.46	1.24	1.52

TABLE 5.1: Some details about the cluster A168.

images. Every cluster position was observed by eye to check for any possible diffuse emission either in the form of a central halo or relics in the periphery. After removing all clusters where halo and relic emission was previously known we were left with a final sample of 10 clusters where extended emission was detected. These were – **A168, A644, A761, A3223, A3266, MCXC J0137.2-0912, MCXC J2146.3-5717, MCXC J0341.2+1534, MCXC J0330.0-5235 and MCXC J2319.1-4206**. Of these 10 the latter 5 suffer from confusion from nearby galaxies and/or radio jets from these galaxies. The former 5 are the most promising in terms of detection of halo and/or relic emission. We present in this chapter preliminary results of the analysis one of these 5 clusters – A168. The remaining 4 clusters show signs of diffue emission in the form of halos and/or relics and are being analysed.

5.3 Abell 168

A168 is a nearby ($z = 0.045$) cluster with richness class of II-III (BM classification) (Yang et al., 2004a). Ulmer et al. (1992) noticed the positional discrepancy of $10'$ between optical and X-ray centre. This could indicate that this cluster was formed by the collision of two approximately same size sub-clusters. Tomita et al. (1996) first reported, based on *Einstein* IPC observation, that the X-ray emission of A168 has two peaks with surface brightness of 9×10^{-14} and 3×10^{-14} erg/s/cm^2, respectively. In a recent X-ray observation with the *Chandra* telescope, Yang et al. (2004b) also found two X-ray peaks correspond with the two subclusters; a northern subcluster (A168N) and a southern subcluster (A168S). Further X-ray observation reveals that the X-ray isophotes surrounding the two X-ray peaks are heavily disturbed and an elongated and continuous filament connects the two X-ray peaks. This indicates that strong interactions has occurred between the two subclusters. Yang et al. (2004a) have obtained superior quality observations of A168 with 13 intermediate filters of BATC (Beijing-Arizona-Taiwan-Connecticut) photometirc system. The SDSS database also contains photometry and the spectroscopic redshift measurement for A168 cluster region. After a cross matching between these two observations, Yang et al. (2004a) compiled a catalogue comprising of 1553 galaxies down to $r' < 20.0$ mag. In this catalog, there are 121 spectroscopically confirmed member galaxies and 255 newly selected members. All of these member galaxies (376) show an elongated distribution along the northwest-southeast direction with a position angle of $\sim 30°$ which is consistent with the spatial characteristic of X-ray distribution. There is also evidence of deviation of the cD galaxy (UGC 00797) and the two X-ray peaks from the local density peak, suggesting the existence of substructures in A168. Further investigation shows an obvious difference in the galaxy content of these two subclusters. A168S is dominated by bright galaxies, while A168N has larger number of faint galaxies. A168N is a subsystem associated with the cD galaxy and likely to be a more evolved system than A168S. All these indications are consistent and support the theory that A168 is likely to be a

head-on merging system at an early stage of the process and that the collision is occurring along the direction perpendicular to our line of sight. However, X-ray observations by Hallman and Markevitch (2004) suggest that core passage between the two subclusters has already occurred at least once. The northern subcluster has reached its apocentre and is about to turn around.

5.4 Radio observation

The radio relic in A168 is not visible in any of the previous radio observations such as NVSS or TGSS. The wideband image between 170-230 MHz (which has the best resolution) reveals the presence of the relic at the north-west edge of the cluster as seen in Figure 5.1. The regions marked A1, A2 and B towards the periphery of the cluster are the regions of extended emission. None of these sources have optical counterparts associated with them. While the relic (B) is visible at all MWA frequencies, it gets blended with other nearby point sources at lower frequencies. Poor angular resolution of MWA is the main limitation to study this relic at low frequencies, except wideband images. Also marked in the figure are two sources to the west of the relic emission marked C and D which have optical counterparts and get blended with the relic at lower frequencies. The bottom panel of Figure 5.1 shows the MWA 154 MHz contours overlaid on the 60″ resolution 150 MHz TGSS image.

5.4.1 GMRT Observations

The cluster was also observed using the GMRT at 325 and 610 MHz. The observation was carried out on November 27 and 28, 2016 for a total of 8 hours at each frequency. The total instantaneous bandwidth at each frequency was 32 MHz which was divided into 256 channels.

This GMRT 325 and 610 MHz data has been processed with a fully automated pipeline based on the SPAM package (Intema et al., 2009, Intema, 2014), which includes direction-dependent calibration, modeling and imaging to suppress ionospheric phase errors. The pipeline consists of two parts: a *pre-processing* part that converts the raw data from individual observing sessions into pre-calibrated visibility data sets for all observed pointings, and a *main pipeline* part that converts these pre-calibrated visibility data sets into stokes I continuum images. The flux scale is set with 3C48 and 3C147 as primary calibrators using the models from Scaife and Heald (2012). Phase calibration was done using 0059+001 as secondary calibrator. More details on the processing pipeline and characteristics of the data products has been given in a paper on the first TGSS alternative data release (Intema et al., 2016, ADR1).

Figure 5.2 shows the MWA 200 MHz contours overlaid on the 325 MHz (top) and 610 MHz (bottom) GMRT images, respectively. As mentioned in Chapter 4, the calibration scheme between Baars et al. (1977) and Scaife and Heald (2012) is in agreement to $\sim 3\%$. In order to re-confirm the calibration between the MWA and GMRT images the spectrum of 10 point sources in the field of view was estimated using the MWA and GMRT images. They were found to fit a power law with an average spectral index $\alpha = 0.75 \pm 0.13$. This agrees with the average spectral index

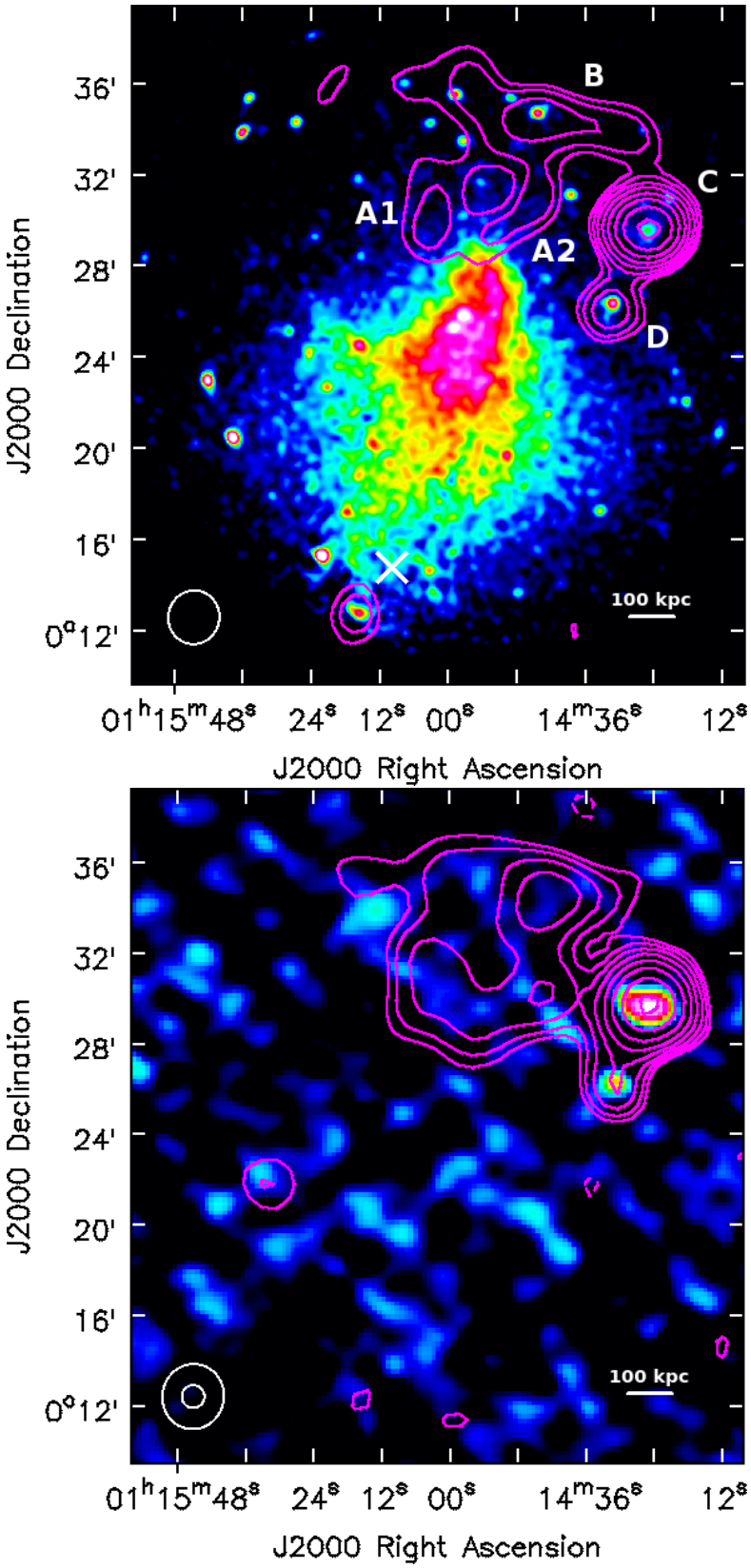

FIGURE 5.1: *Top:* MWA 200 MHz contours of A168 on the *XMM-Newton* X-ray image. *Bottom:* MWA 154 MHz contours on 60″ resolution TGSS image. Contours start at 3σ and increase in steps of $\sqrt{2}$. The resolution of the MWA 200 MHz image is $141'' \times 134'', -10°$ with an RMS of ~ 9 mJy beam^{-1} . The resolution of the MWA 154 MHz image is $173'' \times 163'', -10°$ with an RMS of ~ 16 mJy beam^{-1} .

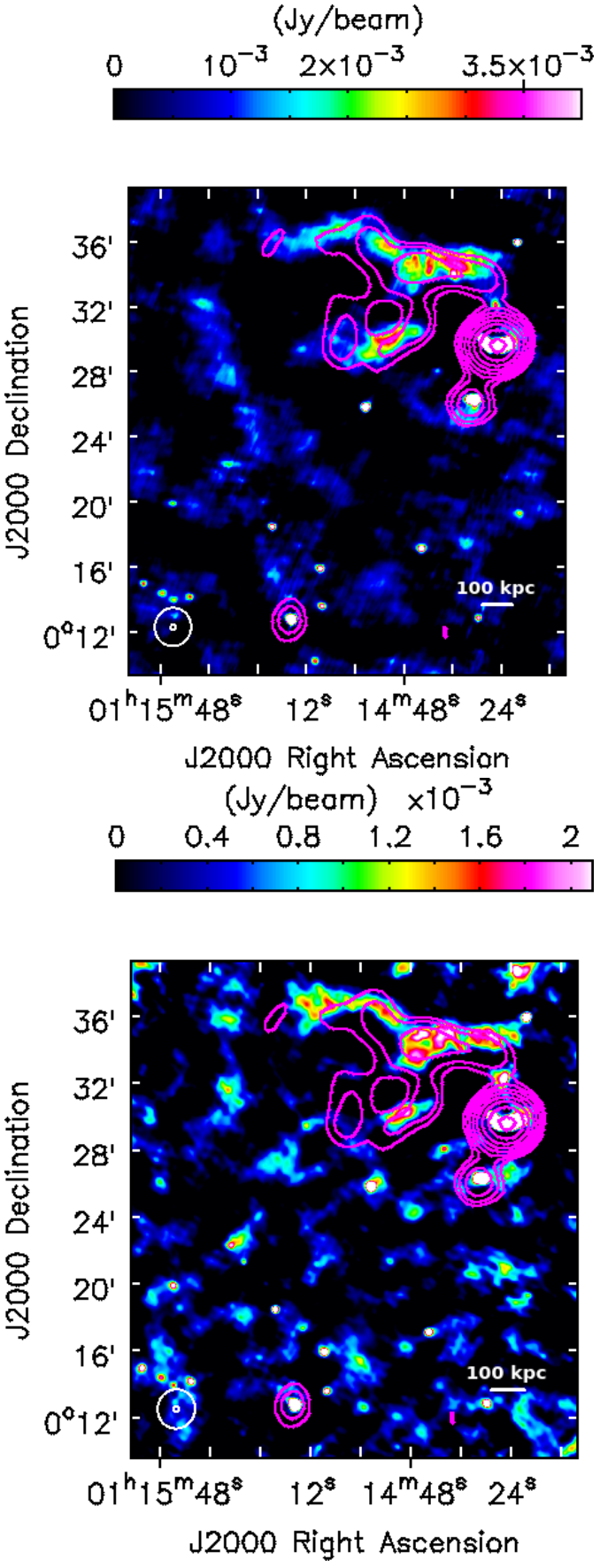

FIGURE 5.2: *Top:* MWA 200 MHz contours of A168 overlaid on GMRT 325 MHz image. *Bottom:* MWA 200 MHz contours of A168 overlaid on GMRT 610 MHz image. Colour bars for the GMRT images are shown over each image. Resolution of both GMRT images is $20'' \times 20''$. RMS of 325 MHz image is 0.9 mJy beam^{-1} while RMS of 610 MHz image is 0.8 mJy beam^{-1} .

Source	Flux Densities (mJy)					
	74 MHz	154 MHz	200 MHz	325 MHz	610 MHz	1400 MHz
A1	–	143.9 ± 11.5	92.5 ± 7.4	–	–	–
A2	320.44 ± 32.04	172.8 ± 13.8	85.9 ± 6.9	97.8 ± 9.8	29.6 ± 3	$\leq 1.8^*$
B	794.7 ± 79.5	320.3 ± 25.6	273.1 ± 21.8	206.4 ± 20.6	104.5 ± 10.5	18.7 ± 1.9
C	–	498 ± 40	397 ± 32	307.1 ± 30.7	208.1 ± 20.8	97.4 ± 10
D	–	85.6 ± 9	73.7 ± 6	54.1 ± 5.41	33.9 ± 3.39	18.5 ± 1.9

TABLE 5.2: Flux densities of the sources A1, A2, the relic B and the point sources C and D. *The RMS of the NVSS image (after convolving to MWA 200 MHz resolution) is taken as the upper limit to the flux density of source A2 at 1400 MHz.

value for extragalactic sources obtained from literature. As examples the spectra of the point sources C and D are given in Figure 5.3.

The spectra of the sources A2 and B are shown in Figure 5.4. VLSSr images were also used to estimate the flux densities of the extended sources. The source A1 is seen only in the MWA images and will not be discussed here. The spectrum of the source A2 includes the RMS of the 1400 MHz NVSS image as an upper limit. Table 5.2 shows the flux density values of the extended source A2, the relic B and the point sources C and D at two MWA frequencies, the two GMRT frequencies as well as at 1400 MHz.

Since no halo is seen in the X-ray region of the cluster we estimated the upper limit to a possible halo emission in the cluster. This was estimated in a manner similar to that used in Chapter 4. The RMS in the central region was 9.15 mJy beam^{-1} . This upper limit to the emission from a halo of size ~ 150 kpc was estimated to be 3.21×10^{21} W Hz^{-1}. This limit is a factor of ~ 12 lower than expected from the $L_X - P_{1.4}$ relation.

5.5 Discussion

The cluster contains two extended diffuse sources on the same side of the cluster centre. The sources A2 and B are 900 and 1150 kpc from the cluster centre, respectively. The sizes of the sources A2 and B are 750 kpc $\times$ 150 kpc and 230 kpc $\times$ 70 kpc, respectively. The curved spectrum of the source A2 seems to suggest that it is just old radio emission from a galaxy. However, source B has a spectral index ($\alpha = -1.23$) similar to those of traditional shock-driven relics.

Chandra observations of A168 by Hallman and Markevitch (2004) suggest that the cluster has recently undergone a merger and the two subclusters have passed one another at least once and are about to turn around. The temperature map of the cluster shows no signs of a hot region between the northern and souther subclusters which would be expected if the two clumps were moving towards each other. However, the temperature map does show a cold front towards the northern edge of the X-ray emission in *front* of the core cD galaxy of the subcluster. Although not as prominent, the southern edge of X-ray emission also shows a decrease in temperature. Hallman and Markevitch (2004) posit that the ICM gas around the northern subcluster has "slingshot" ahead and formed a cold front. This interpretation is also supported by simulations by Mathis et al. (2005) who predict the formation of the cold front as well.

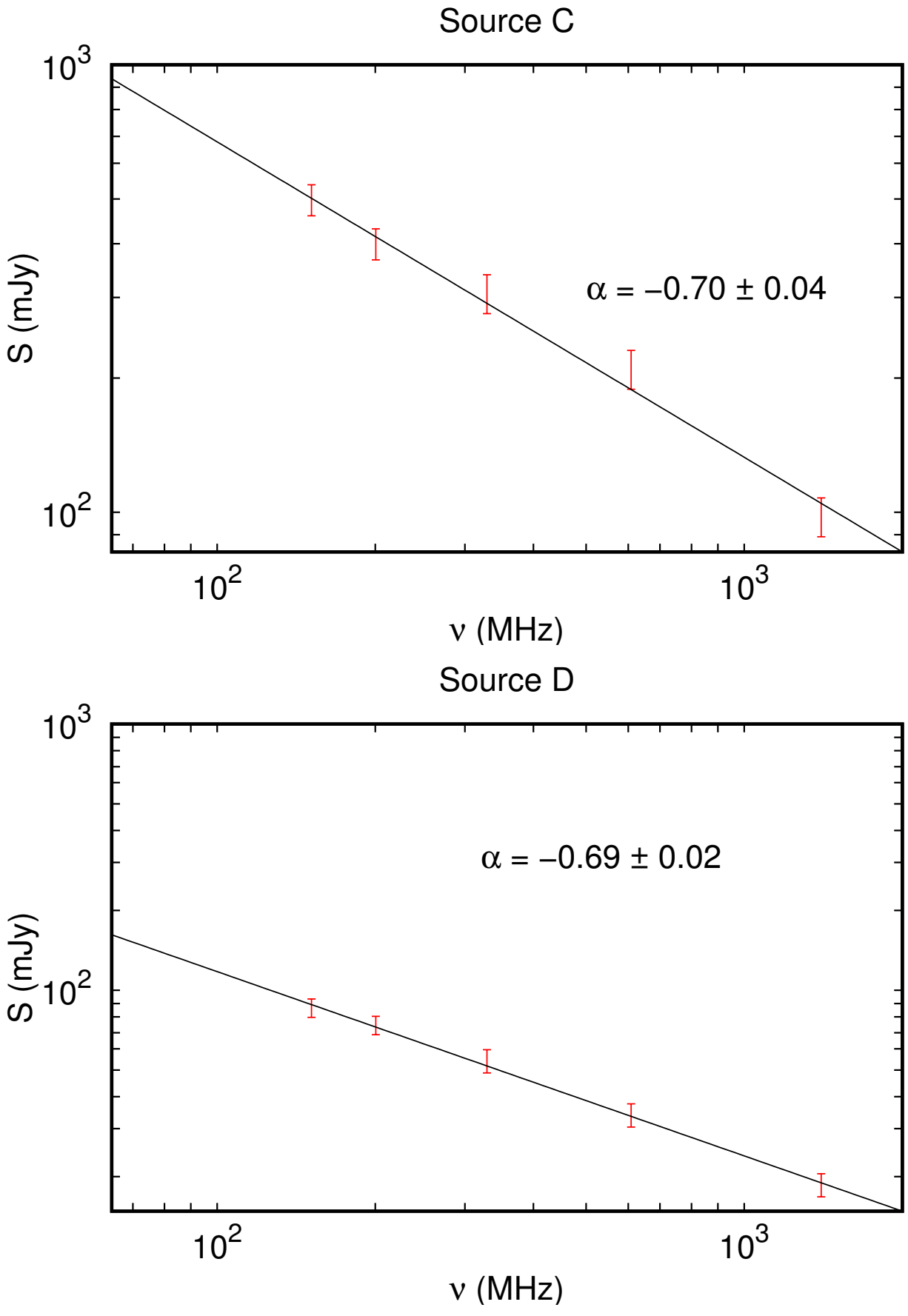

FIGURE 5.3: Spectra of the point sources C and D in the cluster A168.

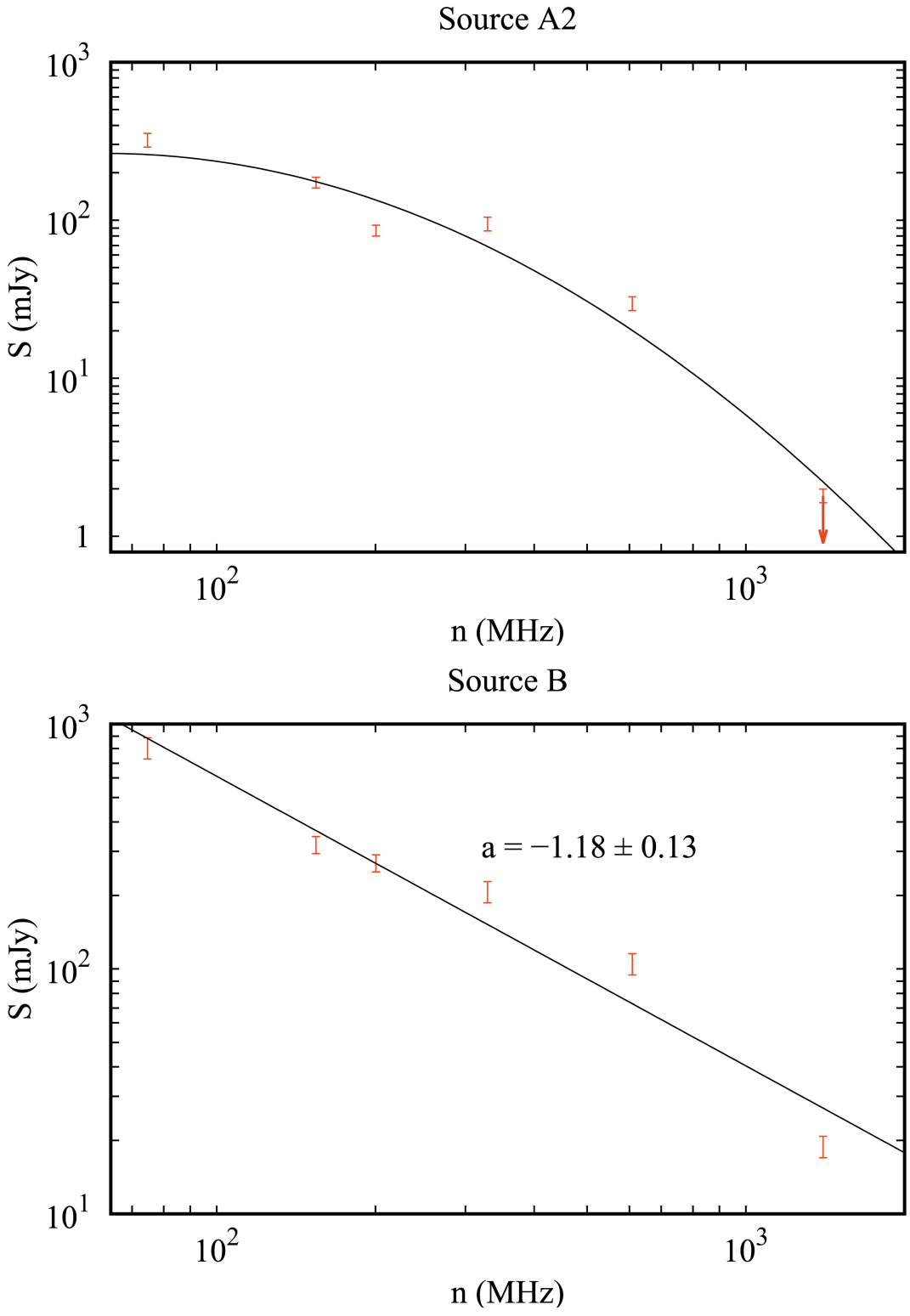

FIGURE 5.4: Spectrum of the extended sources (A2, *top*) and (B, *bottom*).

Based on their spectra as well as the orientation of the sources with respect to the axis of cluster merger the source B seems to be the true relic associated with A168 whereas the source A2 might just be the remnant emission from an old galaxy. The winged shape of source B is also reminiscent of the east relic in A3376 (Figure. 3.1 in Chapter 3) which shows a ridge in the middle of the emission. The curved spectrum of the source A2 is similar to those of relic radio sources as seen by Slee et al. (2001). This curved spectrum suggests that the electrons in the medium have aged significantly and represent emissions from old radio galaxies that are no longer active.

5.6 Summary

In this chapter we present the first possible candidate of a previously unknown relic emission in a cluster found using a blind search of galaxy clusters using the MCXC catalog and then following up with the GLEAM survey images. The galaxy cluster A168 contains two sources of extended radio emission ~ 1 Mpc away from the cluster centre. GMRT observations of the cluster at 325 MHz and 610 MHz were carried out and analysed. These images provided better resolution as compared to the MWA images and are useful to study the various features of the emission. Of the two sources, one is believed to be a genuine shock-accelerated relic whereas the other is believed to be emission from a radio galaxy. The relic in A168 was detected at all MWA frequencies as well as the 2 GMRT frequencies. The spectrum of the relic was found to fit a power law with a spectral index value, $\alpha = -1.18 \pm 0.13$. The other extended source in the cluster has a curved spectrum suggesting that it is the remnant emission of an old galaxy. Both sources are quite complex in nature and are currently being analysed in detail to better understand the nature of their emission.

CHAPTER

SIX

SUMMARY AND FUTURE WORK

6.1 Summary

In this thesis we have analysed merging galaxy clusters at low frequencies using the Murchison Widefield Array (MWA) telescope. This telescope is a precursor to the upcoming Square Kilometre Array (SKA) telescope and provides unprecedented sensitivity to extended emission especially at low frequencies. The aim of the thesis was to utilise this improved sensitivity (as compared to existing telescopes) and gain understanding about the origin of radio halos and relics that have been detected in some galaxy clusters.

Galaxy clusters have not been studied very well at low frequencies. This is especially true of low redshift clusters ($z < 0.1$) because $\sim$ Mpc scale emission in these clusters is likely to get resolved out at higher frequencies. Furthermore, telescopes like the GMRT suffer from RFI at these low frequencies. This is why a telescope like the MWA is extremely useful for studying halo and relic emission in galaxy clusters. We decided to focus on clusters with relics because these relics are indicative of a recent merger in the clusters history. According to the turbulence model merging clusters are also much more likely to host radio halos. The sample of clusters for our study were thus chosen partly to see if the MWA can possibly detect any radio halo that was missed out by previous observations.

6.1.1 Results

- The cluster Abell 3376 was studied at all the five MWA frequencies (*George et al., 2015, MNRAS*). These observations were carried out as part of the GLEAM survey. The data was analysed using the CASA software package and the results of this were compared with those from the pipeline set up to analyse GLEAM data. The two relics of A3376 were detected by the MWA at all of its frequencies. These arc-like relics, which trace the

outgoing shocks produced at the time of cluster merger, have a linear extent of ~ 1 Mpc each and are separated by ~ 1 Mpc from the cluster centre. The spectra of the relics was obtained between $80 - -1400$ MHz. The spectral index of the east and west relics was estimated to be -1.37 ± 0.08 and -1.17 ± 0.06, respectively. The Mach numbers for the shocks estimated from these spectral index values agrees with those estimated from X-ray observations as well as simulations. Assuming that the break frequency due to radiation losses corresponds to the lower end of the spectrum the age of the relics was estimated to be ~ 0.37 Gyr which agrees with the age of the cluster estimated through simulations (~ 0.5 Gyr). No halo emission from the central regions of the cluster was detected. An stringent upper limit to the radio power of a possible radio halo was placed. This upper limit is ~ 35 times lower than that expected from the $L_{\rm X} - P_{1.4}$ relation.

- We analysed 9 merging galaxy clusters with the MWA using the GLEAM images (*George et al. 2016, MNRAS*). The images were produced using a standard pipeline developed to analyse all the GLEAM survey images. We also used the TGSS 150 MHz images which had a better resolution ($25''$) to compared with the MWA images. This was done to identify and subtract unrelated sources that got blended with the halos and relics when estimating their spectra. Radio relics were detected in 7 of the 9 clusters and their spectra estimated over $80 - -1400$ MHz ($80 - 3000$ MHz in the case of PLCK G287.0+32.9) which were all found to be fit with a power law over this range. The cluster A548b contained two sources claimed to be relics. The spectra of these sources was found to be extremely flat (-0.38 and -0.61). Further analysis suggests that these two sources are not the traditional shock-driven radio relics but are instead lobes of one or more nearby radio galaxies. The relic in A13 was found to have an extremely steep spectrum (-1.74). This source too is not a merger related relic but rather it is the remnant emission from an old radio galaxy. Radio halos were detected in 5 of the 9 clusters. Their spectra over $80 - 1400$ MHz was estimated and found to fit a power law over this range. In clusters where no halo was detected we placed upper limits to the radio powers of a possible halo. These factors are $10 - 50$ times below those expected from the $L_{\rm X} - P_{1.4}$ relation.
- Using the MCXC cluster catalog and imposing a redshift cutoff of $z < 0.1$ we produced a sample of ~ 500 clusters which were then analysed using the 200 MHz wideband images produced through the GLEAM survey. These radio images were studied by eye in order to detect clusters which might contain previously undetected radio halos and relics. A total of 10 clusters were short-listed out of which 5 suffer from blending from nearby sources which cannot be easily removed. Of the remaining 5, we presented the preliminary analysis of the relic in the cluster A168. The spectral index of the relic in this cluster over the frequency range $150-1400$ MHz was estimated to be $\alpha = -1.18 \pm 0.13$. No halo is detected in the central regions of the cluster so an upper limit is placed.

6.2 Future Prospects

There are still plenty of unanswered questions when discussing the origin of radio halos and relics. Chief among these is the contribution of the hadronic model in the formation of radio

halos. While it is true that theoretically, synchrotron emission from secondary electrons is expected in all galaxy clusters, the model still has a lot of uncertainties. For instance, the nature of magnetic fields in galaxy clusters is still not very well understood. Independent measurements of magnetic fields in galaxy clusters using Faraday Rotation Measures of the galaxies in the clusters can help constrain the hadronic model. The origin of radio relics is also a matter of debate. While DSA still seems to be the most promising theory that explains their origin, the efficiency with which these low Mach number shocks accelerate electrons in the outskirts of a cluster environment is still under question.

One of the biggest drawbacks of the MWA was its poor resolution. At 200 MHz, MWA had a resolution of $\sim 2'$. Since most radio halos and relics will have an angular extent of $\sim$ few arcmin, MWA observations will lose a lot of the features seen in halos and relics. Blending with nearby galaxies is also a hindrance as discussed in Chapter 4. Since the MWA is very close to being confusion limited at its operating frequencies, improving the resolution will be very useful for studying the extended emission from galaxy clusters. The next phase of operations for the MWA is expected to double the maximum baseline of the telescope from 3 km to 6 km which will be a definite improvement for the detection of halos and relics.

The upcoming SKA will operate between 0.3-20 GHz and is expected to have a resolution of $20''$ at 150 MHz (SKA-LOW) and reach a noise level of $\sim 20\mu$Jy/beam. At 1400 MHz (SKA-MID) the telescope is expected to have a resolution of $\sim 5''$ and a sensitivity $\sim 5\mu$Jy/beam. When operational, the SKA will be the most sensitive radio telescope in the world and should be capable of detecting electron emission in galaxy clusters due to the hadronic model. Improved capabilities in magnetic field measurements in galaxy clusters through the SKA will also help shed light on origin of radio halos and radio relics in galaxy clusters.

BIBLIOGRAPHY

G. A. Ogrean, R. J. van Weeren, C. Jones, T. E. Clarke, J. Sayers, T. Mroczkowski, P. E. J. Nulsen, W. Forman, S. S. Murray, M. Pandey-Pommier, S. Randall, E. Churazov, A. Bonafede, R. Kraft, L. David, F. Andrade-Santos, J. Merten, A. Zitrin, K. Umetsu, A. Goulding, E. Roediger, J. Bagchi, E. Bulbul, M. Donahue, H. Ebeling, M. Johnston-Hollitt, B. Mason, P. Rosati, and A. Vikhlinin. Frontier Fields Clusters: Chandra and JVLA View of the Pre-merging Cluster MACS J0416.1-2403. ApJ, 812:153, October 2015. doi: 10.1088/0004-637X/812/2/153.

E. T. Million and S. W. Allen. Chandra measurements of non-thermal-like X-ray emission from massive, merging, radio halo clusters. MNRAS, 399:1307–1327, November 2009. doi: 10.1111/j.1365-2966.2009.15359.x.

M. Markevitch, A. H. Gonzalez, L. David, A. Vikhlinin, S. Murray, W. Forman, C. Jones, and W. Tucker. A Textbook Example of a Bow Shock in the Merging Galaxy Cluster 1E 0657-56. ApJ, 567:L27–L31, March 2002. doi: 10.1086/339619.

L. Feretti. Observational Properties of Diffuse Halos in Clusters. In A. Pramesh Rao, G. Swarup, and Gopal-Krishna, editors, *The Universe at Low Radio Frequencies*, volume 199 of *IAU Symposium*, page 133, 2002.

M. Thierbach, U. Klein, and R. Wielebinski. The diffuse radio emission from the Coma cluster at 2.675 GHz and 4.85 GHz. A&A, 397:53–61, January 2003. doi: 10.1051/0004-6361:20021474.

F. Govoni, M. Markevitch, A. Vikhlinin, L. van Speybroeck, L. Feretti, and G. Giovannini. Chandra Temperature Maps for Galaxy Clusters with Radio Halos. ApJ, 605:695–708, April 2004. doi: 10.1086/382674.

V. Vacca, L. Feretti, G. Giovannini, F. Govoni, M. Murgia, R. A. Perley, and T. E. Clarke. Spectral index image of the radio halo in the cluster Abell 520, which hosts the famous bow shock. A&A, 561:A52, January 2014. doi: 10.1051/0004-6361/201322504.

R. Kale, T. Venturi, S. Giacintucci, D. Dallacasa, R. Cassano, G. Brunetti, V. Cuciti, G. Macario, and R. Athreya. The Extended GMRT Radio Halo Survey. II. Further results and analysis of the full sample. A&A, 579:A92, July 2015. doi: 10.1051/0004-6361/201525695.

R. Cassano. The radio-X-ray luminosity correlation of radio halos at low radio frequency. Application of the turbulent re-acceleration model. A&A, 517:A10, July 2010. doi: 10.1051/0004-6361/200913622.

R. Kale, K. S. Dwarakanath, J. Bagchi, and S. Paul. Spectral and polarization study of the double relics in Abell 3376 using the Giant Metrewave Radio Telescope and the Very Large Array. MNRAS, 426:1204–1211, October 2012. doi: 10.1111/j.1365-2966.2012.21519.x.

J. Bagchi, F. Durret, G. B. L. Neto, and S. Paul. Giant Ringlike Radio Structures Around Galaxy Cluster Abell 3376. *Science*, 314:791–794, November 2006. doi: 10.1126/science.1131189.

L. Feretti, G. Giovannini, F. Govoni, and M. Murgia. Clusters of galaxies: observational properties of the diffuse radio emission. A&A Rev., 20:54, May 2012. doi: 10.1007/s00159-012-0054-z.

G. Brunetti, R. Cassano, K. Dolag, and G. Setti. On the evolution of giant radio halos and their connection with cluster mergers. A&A, 507:661–669, November 2009. doi: 10.1051/0004-6361/200912751.

T. Venturi, S. Giacintucci, D. Dallacasa, R. Cassano, G. Brunetti, S. Bardelli, and G. Setti. GMRT radio halo survey in galaxy clusters at z = 0.2-0.4. II. The eBCS clusters and analysis of the complete sample. A&A, 484:327–340, June 2008. doi: 10.1051/0004-6361:200809622.

R. Kale, T. Venturi, S. Giacintucci, D. Dallacasa, R. Cassano, G. Brunetti, G. Macario, and R. Athreya. The Extended GMRT Radio Halo Survey. I. New upper limits on radio halos and mini-halos. A&A, 557:A99, September 2013. doi: 10.1051/0004-6361/201321515.

T. Venturi, S. Giacintucci, G. Brunetti, R. Cassano, S. Bardelli, D. Dallacasa, and G. Setti. GMRT radio halo survey in galaxy clusters at z = 0.2-0.4. I. The REFLEX sub-sample. A&A, 463:937–947, March 2007. doi: 10.1051/0004-6361:20065961.

S. Brown, A. Emerick, L. Rudnick, and G. Brunetti. Probing the Off-state of Cluster Giant Radio Halos. ApJ, 740:L28, October 2011. doi: 10.1088/2041-8205/740/1/L28.

O. B. Slee, A. L. Roy, M. Murgia, H. Andernach, and M. Ehle. Four Extreme Relic Radio Sources in Clusters of Galaxies. AJ, 122:1172–1193, September 2001. doi: 10.1086/322105.

L. Feretti, M. Bacchi, O. B. Slee, G. Giovannini, F. Govoni, H. Andernach, and G. Tsarevsky. Diffuse radio sources in the cluster of galaxies Abell 548b. MNRAS, 368:544–552, May 2006. doi: 10.1111/j.1365-2966.2006.10086.x.

L. Feretti, E. Orrù, G. Brunetti, G. Giovannini, N. Kassim, and G. Setti. Spectral index maps of the radio halos in Abell 665 and Abell 2163. A&A, 423:111–119, August 2004. doi: 10.1051/0004-6361:20040316.

L. Feretti, R. Fusco-Femiano, G. Giovannini, and F. Govoni. The giant radio halo in Abell 2163. A&A, 373:106–112, July 2001. doi: 10.1051/0004-6361:20010581.

F. Govoni, L. Feretti, G. Giovannini, H. Böhringer, T. H. Reiprich, and M. Murgia. Radio and X-ray diffuse emission in six clusters of galaxies. A&A, 376:803–819, September 2001a. doi: 10.1051/0004-6361:20011016.

A. Bonafede, G. Giovannini, L. Feretti, F. Govoni, and M. Murgia. Double relics in Abell 2345 and Abell 1240. Spectral index and polarization analysis. A&A, 494:429–442, February 2009. doi: 10.1051/0004-6361:200810588.

A. Bonafede, H. T. Intema, M. Brüggen, M. Girardi, M. Nonino, N. Kantharia, R. J. van Weeren, and H. J. A. Röttgering. Evidence for Particle Re-acceleration in the Radio Relic in the Galaxy Cluster PLCKG287.0+32.9. ApJ, 785:1, April 2014. doi: 10.1088/0004-637X/785/1/1.

T. Venturi, S. Giacintucci, D. Dallacasa, R. Cassano, G. Brunetti, G. Macario, and R. Athreya. Low frequency follow up of radio haloes and relics in the GMRT Radio Halo Cluster Survey. A&A, 551:A24, March 2013. doi: 10.1051/0004-6361/201219872.

L. Feretti, P. Schuecker, H. Böhringer, F. Govoni, and G. Giovannini. Diffuse radio emission in a REFLEX cluster. A&A, 444:157–164, December 2005. doi: 10.1051/0004-6361:20052808.

R. Piffaretti, M. Arnaud, G. W. Pratt, E. Pointecouteau, and J.-B. Melin. The MCXC: a meta-catalogue of x-ray detected clusters of galaxies. A&A, 534:A109, October 2011. doi: 10.1051/0004-6361/201015377.

Planck Collaboration, P. A. R. Ade, N. Aghanim, M. Arnaud, M. Ashdown, J. Aumont, C. Baccigalupi, A. Balbi, A. J. Banday, R. B. Barreiro, and et al. Planck early results. VIII. The all-sky early Sunyaev-Zeldovich cluster sample. A&A, 536:A8, December 2011. doi: 10.1051/0004-6361/201116459.

V. Springel, S. D. M. White, A. Jenkins, C. S. Frenk, N. Yoshida, L. Gao, J. Navarro, R. Thacker, D. Croton, J. Helly, J. A. Peacock, S. Cole, P. Thomas, H. Couchman, A. Evrard, J. Colberg, and F. Pearce. Simulations of the formation, evolution and clustering of galaxies and quasars. Nature, 435:629–636, June 2005. doi: 10.1038/nature03597.

M. Hoeft, M. Brüggen, G. Yepes, S. Gottlöber, and A. Schwope. Diffuse radio emission from clusters in the MareNostrum Universe simulation. MNRAS, 391:1511–1526, December 2008. doi: 10.1111/j.1365-2966.2008.13955.x.

C. L. Sarazin. *X-ray emission from clusters of galaxies*. 1988.

R. Giacconi, S. Murray, H. Gursky, E. Kellogg, E. Schreier, and H. Tananbaum. The Uhuru catalog of X-ray sources. ApJ, 178:281–308, December 1972. doi: 10.1086/151790.

I. M. Gioia, T. Maccacaro, R. E. Schild, A. Wolter, J. T. Stocke, S. L. Morris, and J. P. Henry. The Einstein Observatory Extended Medium-Sensitivity Survey. I - X-ray data and analysis. ApJS, 72:567–619, March 1990. doi: 10.1086/191426.

W. Voges. In *Proceedings of Satellite Symposium 3, ESA, ICY-3*, page 9, 1992.

H. Ebeling, W. Voges, H. Bohringer, A. C. Edge, J. P. Huchra, and U. G. Briel. Properties of the X-ray-brightest Abell-type clusters of galaxies (XBACs) from ROSAT All-Sky Survey data - I. The sample. MNRAS, 281:799–829, August 1996. doi: 10.1093/mnras/281.3.799.

H. Böhringer, P. Schuecker, L. Guzzo, C. A. Collins, W. Voges, S. Schindler, D. M. Neumann, R. G. Cruddace, S. De Grandi, G. Chincarini, A. C. Edge, H. T. MacGillivray, and P. Shaver. The ROSAT-ESO flux limited X-ray (REFLEX) galaxy cluster survey. I. The construction of the cluster sample. A&A, 369:826–850, April 2001. doi: 10.1051/0004-6361:20010240.

H. Böhringer, P. Schuecker, L. Guzzo, C. A. Collins, W. Voges, R. G. Cruddace, A. Ortiz-Gil, G. Chincarini, S. De Grandi, A. C. Edge, H. T. MacGillivray, D. M. Neumann, S. Schindler, and P. Shaver. The ROSAT-ESO Flux Limited X-ray (REFLEX) Galaxy cluster survey. V. The cluster catalogue. A&A, 425:367–383, October 2004. doi: 10.1051/0004-6361:20034484.

H. Ebeling, A. C. Edge, and J. P. Henry. MACS: A Quest for the Most Massive Galaxy Clusters in the Universe. ApJ, 553:668–676, June 2001. doi: 10.1086/320958.

L. Feretti and G. Giovannini. Diffuse Cluster Radio Sources (Review). In R. D. Ekers, C. Fanti, and L. Padrielli, editors, *Extragalactic Radio Sources*, volume 175 of *IAU Symposium*, page 333, 1996.

M. S. Longair. *High energy astrophysics. Volume 2. Stars, the Galaxy and the interstellar medium.* 1994.

M. A. G. Willson. Radio observations of the cluster of galaxies in Coma Berenices - the 5C4 survey. MNRAS, 151:1–44, 1970. doi: 10.1093/mnras/151.1.1.

R. Schlickeiser, A. Sievers, and H. Thiemann. The diffuse radio emission from the Coma cluster. A&A, 182:21–35, August 1987.

G. Giovannini, L. Feretti, T. Venturi, K.-T. Kim, and P. P. Kronberg. The halo radio source Coma C and the origin of halo sources. ApJ, 406:399–406, April 1993. doi: 10.1086/172451.

A. Bonafede, L. Feretti, M. Murgia, F. Govoni, G. Giovannini, D. Dallacasa, K. Dolag, and G. B. Taylor. The Coma cluster magnetic field from Faraday rotation measures. A&A, 513:A30, April 2010. doi: 10.1051/0004-6361/200913696.

C. L. Carilli and G. B. Taylor. Cluster Magnetic Fields. ARA&A, 40:319–348, 2002. doi: 10.1146/annurev.astro.40.060401.093852.

L. Feretti and G. Giovannini. Diffuse radio emission in the Coma cluster. In A. Mazure, F. Casoli, F. Durret, and D. Gerbal, editors, *Untangling Coma Berenices: A New Vision of an Old Cluster*, 1998.

M. Bacchi, L. Feretti, G. Giovannini, and F. Govoni. Deep images of cluster radio halos. A&A, 400:465–476, March 2003. doi: 10.1051/0004-6361:20030044.

G. Giovannini, M. Tordi, and L. Feretti. Radio halo and relic candidates from the NRAO VLA Sky Survey. New A, 4:141–155, March 1999. doi: 10.1016/S1384-1076(99)00018-4.

H. Liang, R. W. Hunstead, M. Birkinshaw, and P. Andreani. A Powerful Radio Halo in the Hottest Known Cluster of Galaxies 1E 0657-56. ApJ, 544:686–701, December 2000. doi: 10.1086/317223.

R. Cassano, G. Brunetti, and G. Setti. Statistics of giant radio haloes from electron reacceleration models. MNRAS, 369:1577–1595, July 2006. doi: 10.1111/j.1365-2966.2006.10423.x.

G. Brunetti, T. Venturi, D. Dallacasa, R. Cassano, K. Dolag, S. Giacintucci, and G. Setti. Cosmic Rays and Radio Halos in Galaxy Clusters: New Constraints from Radio Observations. ApJ, 670:L5–L8, November 2007. doi: 10.1086/524037.

L. Rudnick and J. A. Lemmerman. An Objective Survey of Mpc-scale Radio Emission in 0.03 $<$ z $<$ 0.3 Bright X-ray Clusters. ApJ, 697:1341–1357, June 2009. doi: 10.1088/0004-637X/697/2/1341.

W. J. Jaffe. Origin and transport of electrons in the halo radio source in the Coma cluster. ApJ, 212:1–7, February 1977. doi: 10.1086/155011.

P. Blasi, S. Gabici, and G. Brunetti. Gamma Rays from Clusters of Galaxies. *International Journal of Modern Physics A*, 22:681–706, 2007. doi: 10.1142/S0217751X0703529X.

D. E. Harris, V. K. Kapahi, and R. D. Ekers. Westerbork synthesis observations of 8 clusters of galaxies which contain tailed radio galaxies. A&AS, 39:215–233, February 1980.

P. C. Tribble. Radio haloes, cluster mergers, and cooling flows. MNRAS, 263:31–36, July 1993. doi: 10.1093/mnras/263.1.31.

G. Brunetti, G. Setti, L. Feretti, and G. Giovannini. Particle reacceleration in the Coma cluster: radio properties and hard X-ray emission. MNRAS, 320:365–378, January 2001a. doi: 10.1046/j.1365-8711.2001.03978.x.

V. Petrosian. On the Nonthermal Emission and Acceleration of Electrons in Coma and Other Clusters of Galaxies. ApJ, 557:560–572, August 2001. doi: 10.1086/321557.

Y. Fujita, M. Takizawa, and C. L. Sarazin. Nonthermal Emissions from Particles Accelerated by Turbulence in Clusters of Galaxies. ApJ, 584:190–202, February 2003. doi: 10.1086/345599.

G. Brunetti, P. Blasi, R. Cassano, and S. Gabici. Alfvénic reacceleration of relativistic particles in galaxy clusters: MHD waves, leptons and hadrons. MNRAS, 350:1174–1194, June 2004. doi: 10.1111/j.1365-2966.2004.07727.x.

G. Brunetti and A. Lazarian. Compressible turbulence in galaxy clusters: physics and stochastic particle re-acceleration. MNRAS, 378:245–275, June 2007. doi: 10.1111/j.1365-2966.2007.11771.x.

D. A. Buote and J. C. Tsai. Quantifying the Morphologies and Dynamical Evolution of Galaxy Clusters. I. The Method. ApJ, 452:522, October 1995. doi: 10.1086/176326.

H. Böhringer, G. W. Pratt, M. Arnaud, S. Borgani, J. H. Croston, T. J. Ponman, S. Ameglio, R. F. Temple, and K. Dolag. Substructure of the galaxy clusters in the REXCESS sample: observed statistics and comparison to numerical simulations. A&A, 514:A32, May 2010. doi: 10.1051/0004-6361/200913911.

G. B. Poole, M. A. Fardal, A. Babul, I. G. McCarthy, T. Quinn, and J. Wadsley. The impact of mergers on relaxed X-ray clusters - I. Dynamical evolution and emergent transient structures. MNRAS, 373:881–905, December 2006. doi: 10.1111/j.1365-2966.2006.10916.x.

B. J. Maughan, C. Jones, W. Forman, and L. Van Speybroeck. Images, Structural Properties, and Metal Abundances of Galaxy Clusters Observed with Chandra ACIS-I at $0.1 < z < 1.3$. ApJS, 174:117-135, January 2008. doi: 10.1086/521225.

J. S. Santos, P. Rosati, P. Tozzi, H. Böhringer, S. Ettori, and A. Bignamini. Searching for cool core clusters at high redshift. A&A, 483:35–47, May 2008. doi: 10.1051/0004-6361:20078815.

D. A. Buote. On the Origin of Radio Halos in Galaxy Clusters. ApJ, 553:L15–L18, May 2001. doi: 10.1086/320500.

R. Cassano and G. Brunetti. Cluster mergers and non-thermal phenomena: a statistical magneto-turbulent model. MNRAS, 357:1313–1329, March 2005. doi: 10.1111/j.1365-2966.2005.08747.x.

G. Brunetti and A. Lazarian. Acceleration of primary and secondary particles in galaxy clusters by compressible MHD turbulence: from radio haloes to gamma-rays. MNRAS, 410:127–142, January 2011. doi: 10.1111/j.1365-2966.2010.17457.x.

G. Brunetti, G. Setti, L. Feretti, and G. Giovannini. Particle injection and reacceleration in clusters of galaxies and the EUV excess: the case of Coma. New A, 6:1–15, February 2001b. doi: 10.1016/S1384-1076(00)00048-8.

P. M. Ricker and C. L. Sarazin. Off-Axis Cluster Mergers: Effects of a Strongly Peaked Dark Matter Profile. ApJ, 561:621–644, November 2001. doi: 10.1086/323365.

G. Brunetti and A. Lazarian. Stochastic reacceleration of relativistic electrons by turbulent reconnection: a mechanism for cluster-scale radio emission? MNRAS, 458:2584–2595, May 2016. doi: 10.1093/mnras/stw496.

B. Dennison. Formation of radio halos in clusters of galaxies from cosmic-ray protons. ApJ, 239: L93–L96, August 1980. doi: 10.1086/183300.

P. Blasi and S. Colafrancesco. Cosmic rays, radio halos and nonthermal X-ray emission in clusters of galaxies. *Astroparticle Physics*, 12:169–183, November 1999. doi: 10.1016/S0927-6505(99)00079-1.

K. Dolag and T. A. Enßlin. Radio halos of galaxy clusters from hadronic secondary electron injection in realistic magnetic field configurations. A&A, 362:151–157, October 2000.

O. Reimer, M. Pohl, P. Sreekumar, and J. R. Mattox. EGRET Upper Limits on the High-Energy Gamma-Ray Emission of Galaxy Clusters. ApJ, 588:155–164, May 2003. doi: 10.1086/374046.

M. Ackermann, M. Ajello, A. Allafort, L. Baldini, et al. GeV Gamma-ray Flux Upper Limits from Clusters of Galaxies. ApJ, 717:L71–L78, July 2010. doi: 10.1088/2041-8205/717/1/L71.

T. E. Jeltema and S. Profumo. Implications of Fermi Observations For Hadronic Models of Radio Halos in Clusters of Galaxies. ApJ, 728:53, February 2011. doi: 10.1088/0004-637X/728/1/53.

R. Blandford and D. Eichler. Particle acceleration at astrophysical shocks: A theory of cosmic ray origin. Phys. Rep., 154:1–75, October 1987. doi: 10.1016/0370-1573(87)90134-7.

F. C. Jones and D. C. Ellison. The plasma physics of shock acceleration. Space Sci. Rev., 58: 259–346, December 1991. doi: 10.1007/BF01206003.

M. Markevitch and A. Vikhlinin. Shocks and cold fronts in galaxy clusters. Phys. Rep., 443: 1–53, May 2007. doi: 10.1016/j.physrep.2007.01.001.

H. Kang, T. W. Jones, and U. D. J. Gieseler. Numerical Studies of Cosmic-Ray Injection and Acceleration. ApJ, 579:337–358, November 2002. doi: 10.1086/342724.

H. Kang and D. Ryu. Re-acceleration of Non-thermal Particles at Weak Cosmological Shock Waves. ApJ, 734:18, June 2011. doi: 10.1088/0004-637X/734/1/18.

F. Vazza and M. Brüggen. Do radio relics challenge diffusive shock acceleration? MNRAS, 437: 2291–2296, January 2014. doi: 10.1093/mnras/stt2042.

F. Vazza, D. Eckert, M. Brüggen, and B. Huber. Electron and proton acceleration efficiency by merger shocks in galaxy clusters. MNRAS, 451:2198–2211, August 2015. doi: 10.1093/mnras/stv1072.

F. Vazza, M. Brüggen, D. Wittor, C. Gheller, D. Eckert, and M. Stubbe. Constraining the efficiency of cosmic ray acceleration by cluster shocks. MNRAS, 459:70–83, June 2016. doi: 10.1093/mnras/stw584.

D. Dallacasa, G. Brunetti, S. Giacintucci, R. Cassano, T. Venturi, G. Macario, N. E. Kassim, W. Lane, and G. Setti. Deep 1.4 GHz Follow-up of the Steep Spectrum Radio Halo in A521. ApJ, 699:1288–1292, July 2009. doi: 10.1088/0004-637X/699/2/1288.

H. Ebeling, A. C. Edge, H. Bohringer, S. W. Allen, C. S. Crawford, A. C. Fabian, W. Voges, and J. P. Huchra. The ROSAT Brightest Cluster Sample - I. The compilation of the sample and the cluster log N-log S distribution. MNRAS, 301:881–914, December 1998. doi: 10.1046/j.1365-8711.1998.01949.x.

H. Ebeling, A. C. Edge, S. W. Allen, C. S. Crawford, A. C. Fabian, and J. P. Huchra. The ROSAT Brightest Cluster Sample - IV. The extended sample. MNRAS, 318:333–340, October 2000. doi: 10.1046/j.1365-8711.2000.03549.x.

R. Cassano, G. Brunetti, and G. Setti. Occurence and Luminosity Functions of Giant Radio Halos from Magneto-Turbulent Model. *Journal of Korean Astronomical Society*, 37:589–592, December 2004. doi: 10.5303/JKAS.2004.37.5.589.

C. J. Lonsdale, R. J. Cappallo, M. F. Morales, F. H. Briggs, et al. The Murchison Widefield Array: Design Overview. *IEEE Proceedings*, 97:1497–1506, August 2009. doi: 10.1109/JPROC.2009.2017564.

S. J. Tingay, R. Goeke, J. D. Bowman, D. Emrich, et al. The Murchison Widefield Array: The Square Kilometre Array Precursor at Low Radio Frequencies. PASA, 30:e007, January 2013. doi: 10.1017/pasa.2012.007.

P. Dewdney, W. Turner, R. Millenaar, R. McCool, J. Lazio, and T. J. Cornwell. SKA1 System Baseline Design, Document number SKA-TEL-SKO-DD-001. 2013.

P. J. Hall. The Square Kilometre Array: An International Engineering Perspective. *Experimental Astronomy*, 17:5–16, June 2004. doi: 10.1007/s10686-005-4190-6.

R. J. Nijboer, M. Pandey-Pommier, and A. G. de Bruyn. LOFAR imaging capabilities and system sensitivity. *ArXiv e-prints*, August 2013.

R. B. Wayth et al. GLEAM: The GaLactic and Extragalactic All-sky MWA survey. *ArXiv e-prints*, May 2015.

N. Hurley-Walker et al. The Murchison Widefield Array Commissioning Survey: A Low-Frequency Catalogue of 14 110 Compact Radio Sources over 6 100 Square Degrees. PASA, 31:e045, November 2014. doi: 10.1017/pasa.2014.40.

A. R. Offringa, B. McKinley, N. Hurley-Walker, F. H. Briggs, et al. WSCLEAN: an implementation of a fast, generic wide-field imager for radio astronomy. MNRAS, 444:606–619, October 2014. doi: 10.1093/mnras/stu1368.

A. Sutinjo, J. O'Sullivan, E. Lenc, R. B. Wayth, S. Padhi, P. Hall, and S. J. Tingay. Understanding instrumental Stokes leakage in Murchison Widefield Array polarimetry. *Radio Science*, 50: 52–65, January 2015. doi: 10.1002/2014RS005517.

J. W. M. Baars, R. Genzel, I. I. K. Pauliny-Toth, and A. Witzel. The absolute spectrum of CAS A - an accurate flux density scale and a set of secondary calibrators. A&A, 61:99–106, October 1977.

N. Hurley-Walker, J. R. Callingham, P. J. Hancock, T. M. O. Franzen, L. Hindson, A. D. Kapińska, J. Morgan, A. R. Offringa, R. B. Wayth, C. Wu, Q. Zheng, T. Murphy, M. E. Bell, K. S. Dwarakanath, B. For, B. M. Gaensler, M. Johnston-Hollitt, E. Lenc, P. Procopio, L. Staveley-Smith, R. Ekers, J. D. Bowman, F. Briggs, R. J. Cappallo, A. A. Deshpande, L. Greenhill, B. J. Hazelton, D. L. Kaplan, C. J. Lonsdale, S. R. McWhirter, D. A. Mitchell, M. F. Morales, E. Morgan, D. Oberoi, S. M. Ord, T. Prabu, N. U. Shankar, K. S. Srivani, R. Subrahmanyan, S. J. Tingay, R. L. Webster, A. Williams, and C. L. Williams. GaLactic and Extragalactic All-sky Murchison Widefield Array (GLEAM) survey - I. A low-frequency extragalactic catalogue. MNRAS, 464:1146–1167, January 2017. doi: 10.1093/mnras/stw2337.

M. F. Struble and H. J. Rood. A Compilation of Redshifts and Velocity Dispersions for ACO Clusters. ApJS, 125:35–71, November 1999. doi: 10.1086/313274.

T. H. Reiprich and H. Böhringer. The Mass Function of an X-Ray Flux-limited Sample of Galaxy Clusters. ApJ, 567:716–740, March 2002. doi: 10.1086/338753.

M. Girardi, S. Borgani, G. Giuricin, F. Mardirossian, and M. Mezzetti. The Observational Mass Function of Nearby Galaxy Clusters. ApJ, 506:45–52, October 1998. doi: 10.1086/306252.

E. Escalera, A. Biviano, M. Girardi, G. Giuricin, F. Mardirossian, A. Mazure, and M. Mezzetti. Structures in Galaxy Clusters. ApJ, 423:539, March 1994. doi: 10.1086/173833.

F. Durret, C. Perrot, G. B. Lima Neto, C. Adami, E. Bertin, and J. Bagchi. The merging cluster of galaxies Abell 3376: an optical view. A&A, 560:A78, December 2013. doi: 10.1051/0004-6361/201322082.

R. E. G. Machado and G. B. Lima Neto. Simulations of the merging galaxy cluster Abell 3376. MNRAS, 430:3249–3260, April 2013. doi: 10.1093/mnras/stt127.

A. R. Offringa et al. The Low-Frequency Environment of the Murchison Widefield Array: Radio-Frequency Interference Analysis and Mitigation. PASA, 32:e008, March 2015. doi: 10.1017/pasa.2015.7.

A. R. Offringa, A. G. de Bruyn, M. Biehl, S. Zaroubi, G. Bernardi, and V. N. Pandey. Post-correlation radio frequency interference classification methods. MNRAS, 405:155–167, June 2010. doi: 10.1111/j.1365-2966.2010.16471.x.

A. R. Offringa, J. J. van de Gronde, and J. B. T. M. Roerdink. A morphological algorithm for improving radio-frequency interference detection. A&A, 539:A95, March 2012. doi: 10.1051/0004-6361/201118497.

F. R. Schwab. Relaxing the isoplanatism assumption in self-calibration; applications to low-frequency radio interferometry. AJ, 89:1076–1081, July 1984. doi: 10.1086/113605.

T. J. Cornwell, K. Golap, and S. Bhatnagar. The Noncoplanar Baselines Effect in Radio Interferometry: The W-Projection Algorithm. *IEEE Journal of Selected Topics in Signal Processing*, 2:647–657, November 2008. doi: 10.1109/JSTSP.2008.2005290.

D. S. Briggs. *High Fidelity Deconvolution of Moderately Resolved Sources*. PhD thesis, New Mexico Institue of Mining Technology, Socorro, New Mexico, USA, 1995.

R. A. Perley and B. J. Butler. An Accurate Flux Density Scale from 1 to 50 GHz. ApJS, 204:19, February 2013. doi: 10.1088/0067-0049/204/2/19.

C. L. Sarazin. The Energy Spectrum of Primary Cosmic-Ray Electrons in Clusters of Galaxies and Inverse Compton Emission. ApJ, 520:529–547, August 1999. doi: 10.1086/307501.

S. Giacintucci, T. Venturi, G. Macario, D. Dallacasa, G. Brunetti, M. Markevitch, R. Cassano, S. Bardelli, and R. Athreya. Shock acceleration as origin of the radio relic in A 521? A&A, 486:347–358, August 2008. doi: 10.1051/0004-6361:200809459.

H. Akamatsu, M. Takizawa, K. Nakazawa, Y. Fukazawa, Y. Ishisaki, and T. Ohashi. X-Ray View of the Shock Front in the Merging Cluster Abell 3376 with Suzaku. PASJ, 64:67, August 2012. doi: 10.1093/pasj/64.4.67.

F. Govoni, M. Murgia, H. Xu, H. Li, M. L. Norman, L. Feretti, G. Giovannini, and V. Vacca. Polarization of cluster radio halos with upcoming radio interferometers. A&A, 554:A102, June 2013. doi: 10.1051/0004-6361/201321403.

G. Brunetti, G. Setti, L. Feretti, and G. Giovannini. Particle reacceleration in the Coma cluster: radio properties and hard X-ray emission. MNRAS, 320:365–378, January 2001c. doi: 10.1046/j.1365-8711.2001.03978.x.

J. C. Kempner and C. L. Sarazin. Radio Halo and Relic Candidates from the Westerbork Northern Sky Survey. ApJ, 548:639–651, February 2001. doi: 10.1086/319024.

L. Feretti. Observational Properties of Diffuse Halos in Clusters. *ArXiv Astrophysics e-prints*, June 2000.

F. Govoni, L. Feretti, G. Giovannini, H. Böhringer, T. H. Reiprich, and M. Murgia. Radio and X-ray diffuse emission in six clusters of galaxies. A&A, 376:803–819, September 2001b. doi: 10.1051/0004-6361:20011016.

J. D. Bowman, I. Cairns, D. L. Kaplan, T. Murphy, et al. Science with the Murchison Widefield Array. PASA, 30:e031, April 2013. doi: 10.1017/pas.2013.009.

M. P. van Haarlem, M. W. Wise, A. W. Gunst, G. Heald, et al. LOFAR: The LOw-Frequency ARray. A&A, 556:A2, August 2013. doi: 10.1051/0004-6361/201220873.

H. T. Intema, S. van der Tol, W. D. Cotton, A. S. Cohen, I. M. van Bemmel, and H. J. A. Röttgering. Ionospheric calibration of low frequency radio interferometric observations using the peeling scheme. I. Method description and first results. A&A, 501:1185–1205, July 2009. doi: 10.1051/0004-6361/200811094.

H. T. Intema. SPAM: A data reduction recipe for high-resolution, low-frequency radio-interferometric observations. *ArXiv e-prints*, February 2014.

A. M. M. Scaife and G. H. Heald. A broad-band flux scale for low-frequency radio telescopes. MNRAS, 423:L30–L34, June 2012. doi: 10.1111/j.1745-3933.2012.01251.x.

H. T. Intema, P. Jagannathan, K. P. Mooley, and D. A. Frail. The GMRT 150 MHz All-sky Radio Survey: First Alternative Data Release TGSS ADR1. *ArXiv e-prints*, March 2016.

A. M. Juett, C. L. Sarazin, T. E. Clarke, H. Andernach, M. Ehle, Y. Fujita, J. C. Kempner, A. L. Roy, L. Rudnick, and O. B. Slee. A Chandra Observation of Abell 13: Investigating the Origin of the Radio Relic. ApJ, 672:138–145, January 2008. doi: 10.1086/523350.

R. den Hartog and P. Katgert. On the dynamics of the cores of galaxy clusters. MNRAS, 279: 349–388, March 1996. doi: 10.1093/mnras/279.2.349.

L. Solovyeva, S. Anokhin, L. Feretti, J. L. Sauvageot, R. Teyssier, G. Giovannini, F. Govoni, and D. Neumann. The dynamical state of A548 from XMM-Newton data: X-ray and radio connection. A&A, 484:621–630, June 2008. doi: 10.1051/0004-6361:200809445.

J. M. Hill and W. R. Oegerle. Dynamics of cD clusters of galaxies. I - Redshift data for seven clusters. AJ, 106:831–847, September 1993. doi: 10.1086/116688.

K. N. Kanov, C. L. Sarazin, and A. K. Hicks. Chandra Observation of the Interaction of the Radio Source and Cooling Core in Abell 2063. ApJ, 653:184–192, December 2006. doi: 10.1086/508862.

S. S. Komissarov and A. G. Gubanov. Relic radio galaxies: evolution of synchrotron spectrum. A&A, 285:27–43, May 1994.

H. Bourdin, M. Arnaud, P. Mazzotta, G. W. Pratt, J.-L. Sauvageot, R. Martino, S. Maurogordato, A. Cappi, C. Ferrari, and C. Benoist. A2163: Merger events in the hottest Abell galaxy cluster. II. Subcluster accretion with galaxy-gas separation. A&A, 527:A21, March 2011. doi: 10.1051/0004-6361/201014907.

H. Böhringer, W. Voges, J. P. Huchra, B. McLean, R. Giacconi, P. Rosati, R. Burg, J. Mader, P. Schuecker, D. Simiç, S. Komossa, T. H. Reiprich, J. Retzlaff, and J. Trümper. The Northern ROSAT All-Sky (NORAS) Galaxy Cluster Survey. I. X-Ray Properties of Clusters Detected as Extended X-Ray Sources. ApJS, 129:435–474, August 2000. doi: 10.1086/313427.

C. S. Crawford, A. C. Edge, A. C. Fabian, S. W. Allen, H. Bohringer, H. Ebeling, R. G. McMahon, and W. Voges. Optical spectroscopy of the ROSAT X-ray brightest clusters - II. MNRAS, 274:75–84, May 1995. doi: 10.1093/mnras/274.1.75.

M. Girardi, S. Bardelli, R. Barrena, W. Boschin, F. Gastaldello, and M. Nonino. Internal dynamics of Abell 2254: a merging galaxy cluster with a clumpy, diffuse radio emission. A&A, 536:A89, December 2011. doi: 10.1051/0004-6361/201117332.

W. Boschin, R. Barrena, and M. Girardi. The complex structure of Abell 2345: a galaxy cluster with non-symmetric radio relics. A&A, 521:A78, October 2010. doi: 10.1051/0004-6361/201014839.

H. Ebeling, A. C. Edge, A. Mantz, E. Barrett, J. P. Henry, C. J. Ma, and L. van Speybroeck. The X-ray brightest clusters of galaxies from the Massive Cluster Survey. MNRAS, 407:83–93, September 2010. doi: 10.1111/j.1365-2966.2010.16920.x.

J. C. Kempner and L. P. David. A Chandra view of the multiple merger in Abell 2744. MNRAS, 349:385–392, April 2004. doi: 10.1111/j.1365-2966.2004.07534.x.

W. Boschin, M. Girardi, M. Spolaor, and R. Barrena. Internal dynamics of the radio halo cluster Abell 2744. A&A, 449:461–474, April 2006. doi: 10.1051/0004-6361:20054408.

M. S. Owers, S. W. Randall, P. E. J. Nulsen, W. J. Couch, L. P. David, and J. C. Kempner. The Dissection of Abell 2744: A Rich Cluster Growing Through Major and Minor Mergers. ApJ, 728:27, February 2011. doi: 10.1088/0004-637X/728/1/27.

F. Govoni, T. A. Enßlin, L. Feretti, and G. Giovannini. A comparison of radio and X-ray morphologies of four clusters of galaxies containing radio halos. A&A, 369:441–449, April 2001c. doi: 10.1051/0004-6361:20010115.

J. Bagchi, S. K. Sirothia, N. Werner, M. B. Pandge, N. G. Kantharia, C. H. Ishwara-Chandra, Gopal-Krishna, S. Paul, and S. Joshi. Discovery of the First Giant Double Radio Relic in a Galaxy Cluster Found in the Planck Sunyaev-Zel'dovich Cluster Survey: PLCK G287.0+32.9. ApJ, 736:L8, July 2011. doi: 10.1088/2041-8205/736/1/L8.

I. Valtchanov, T. Murphy, M. Pierre, R. Hunstead, and L. Lémonon. Abell 1451 and 1RXS J131423.6-251521: A multi-wavelength study of two dynamically perturbed clusters of galaxies. A&A, 392:795–805, September 2002. doi: 10.1051/0004-6361:20020940.

D. C.-J. Bock, M. I. Large, and E. M. Sadler. SUMSS: A Wide-Field Radio Imaging Survey of the Southern Sky. I. Science Goals, Survey Design, and Instrumentation. AJ, 117:1578–1593, March 1999. doi: 10.1086/300786.

G. Brunetti, S. Giacintucci, R. Cassano, W. Lane, D. Dallacasa, T. Venturi, N. E. Kassim, G. Setti, W. D. Cotton, and M. Markevitch. A low-frequency radio halo associated with a cluster of galaxies. Nature, 455:944–947, October 2008. doi: 10.1038/nature07379.

G. Brunetti and P. Blasi. Alfvénic reacceleration of relativistic particles in galaxy clusters in the presence of secondary electrons and positrons. MNRAS, 363:1173–1187, November 2005. doi: 10.1111/j.1365-2966.2005.09511.x.

H. Böhringer, C. A. Collins, L. Guzzo, P. Schuecker, W. Voges, D. M. Neumann, S. Schindler, G. Chincarini, S. De Grandi, R. G. Cruddace, A. C. Edge, T. H. Reiprich, and P. Shaver. The ROSAT-ESO Flux-limited X-Ray (REFLEX) Galaxy Cluster Survey. IV. The X-Ray Luminosity Function. ApJ, 566:93–102, February 2002. doi: 10.1086/338072.

Y. Yang, X. Zhou, Q. Yuan, Z. Jiang, J. Ma, H. Wu, and J. Chen. Large-Field Multicolor Study of A168: Subclusters, Dynamics, and Luminosity Functions. ApJ, 600:141–148, January 2004a. doi: 10.1086/379703.

M. P. Ulmer, G. D. Wirth, and M. P. Kowalski. Clusters in collision? ApJ, 397:430–437, October 1992. doi: 10.1086/171798.

A. Tomita, F. E. Nakamura, T. Takata, K. Nakanishi, T. Takeuchi, K. Ohta, and T. Yamada. Distribution of Blue Galaxies in a Merging Cluster of Galaxies Abell 168. AJ, 111:42, January 1996. doi: 10.1086/117758.

Y. Yang, Z. Huo, X. Zhou, S. Xue, S. Mao, J. Ma, and J. Chen. Chandra X-Ray Observations of Galaxy Cluster A168. ApJ, 614:692–697, October 2004b. doi: 10.1086/423925.

E. J. Hallman and M. Markevitch. Chandra Observation of the Merging Cluster A168: A Late Stage in the Evolution of a Cold Front. ApJ, 610:L81–L84, August 2004. doi: 10.1086/423449.

H. Mathis, G. Lavaux, J. M. Diego, and J. Silk. On the formation of cold fronts in massive mergers. MNRAS, 357:801–818, March 2005. doi: 10.1111/j.1365-2966.2004.08589.x.